A Next-Generation Apparatus for Lithium Optical Lattice Experiments

by

Aviv Keshet

Submitted to the Department of Physics
in partial fulfillment of the requirements for the degree of

Doctor of Philosophy

at the

MASSACHUSETTS INSTITUTE OF TECHNOLOGY

September 2012

Author .....
Department of Physics
August 24, 2012

Certified by .....
Wolfgang Ketterle
John D. MacArthur Professor of Physics
Thesis Supervisor

Accepted by .....
Krishna Rajagopal
Professor of Physics, Associate Department Head for Education

A Next-Generation Apparatus for Lithium Optical Lattice Experiments

by

Aviv Keshet

Submitted to the Department of Physics
on August 24, 2012, in partial fulfillment of the
requirements for the degree of
Doctor of Philosophy

Abstract

Quantum simulation is emerging as an ambitious and active subfield of atomic physics. This thesis describes progress towards the goal of simulating condensed matter systems, in particular the physics of the Fermi-Hubbard model, using ultracold Lithium atoms in an optical lattice.

A major goal of the quantum simulation program is to observe phase transitions of the Hubbard model, into Néel antiferromagnetic phases and d-wave superfluid phases. Phase transitions are generally accompanied by a change in an underlying correlation in a physical system. Such correlations may be most amenable to probing by looking at fluctuations in the system. Experimental techniques for probing density and magnetization fluctuations in a variety of atomic Fermi systems are developed. The suppression of density fluctuations (or atom "shot noise") in an ideal degenerate Fermi gas is observed by absorption imaging of time-of-flight expanded clouds. In-trap measurements of density and magnetization fluctuations are not easy to probe with absorption imaging, due to their extremely high attenuation. A method to probe these fluctuations based on speckle patterns, caused by fluctuations in the index of refraction for a detuned illumination beam, is developed and applied first to weakly interacting and then to strongly interacting in-trap gases. Fluctuation probes such as these will be a crucial tool in future quantum simulation of condensed matter systems.

The quantum simulation experiments that we want to perform require a complex sequence of precisely timed computer controlled events. A distributed GUI-based control system designed with such experiments in mind, The Cicero Word Generator, is described. The system makes use of a client-server separation between a user interface for sequence design and a set of output hardware servers. Output hardware servers are designed to use standard National Instruments output cards, but the client-server nature allows this to be extended to other output hardware. Output sequences running on multiple servers and output cards can be synchronized using a shared clock. By using an FPGA-generated variable frequency clock, redundant buffers can be dramatically shortened, and a time resolution of 100ns achieved over effectively arbitrary sequence lengths.

Experimental set-ups for producing, manipulating, and probing ultracold atomic gases can be quite complicated. To move forward with a quantum simulation program, it is necessary to have an apparatus that operates with a reliability that is not easily achieved in the face of this complexity. The design of a new apparatus is discussed. This Sodium-Lithium ultracold gas production machine has been engineered to incorporate as much experimental experience as possible to enhance its reliability. Particular attention has been paid to maximizing optical access and the utilization of this optical access, controlling the ambient temperature of the experiment, achieving a high vacuum, and simplifying subsystems where possible. The apparatus is now on the verge of producing degenerate gases, and should serve as a stable platform on which to perform future lattice quantum simulation experiments.

Thesis Supervisor: Wolfgang Ketterle
Title: John D. MacArthur Professor of Physics

Acknowledgments

First and foremost, I would like to thank my parents, Leah and Joshua, and my brother Ilan. Without your love, support, and encouragement, none of this would have been meaningful.

I've been blessed with a circle of friends beyond compare. The antics of my hometown boys, Zev, Dave, and Eric, always left me looking forward to our next meetings. Nicolas has perfected the art of the out of context text message quote, and I thank him for providing the necessary means for a necessary means for a higher education. Leo was always a willing test subject for newly invented handshakes. Thanks to Antoine and Miranda's undamped oscillations between Cambridge and New York, I know I will always have a place to stay on the east coast. Brenda, I'm glad I was able to teach you how the moon works. And Kirill, my writing buddy, first you destroyed and then you enhanced my productivity.

MIT has been a challenging and exciting place. It may be a cliché to say that I've met the most intelligent people I've ever known here, but only because it is statement that everyone here truthfully experiences.

The BEC2 lab has had a consistent stream of frighteningly smart, unique, and intense characters. Jit Kee's commitment to doing things right if you're going to bother doing them at all set the lab up for success. And Jit Kee, you're welcome for the elephant [15]. When I first joined the lab, it was clear that Dan was the hallway's social glue. He has grown into a close friend outside of the lab, thanks to his mastery of humor as a motivational tool, and I thank him for awarding me the first (soft) academic medal of my career. Widagdo's technological zeal set many good precedents in the lab, even if most of his LEDs have been decommissioned. Christian is a fascinating individual, and not just because of his two-finger typing technique. Without his infinite patience, and his extra-sensory communication ability with any physics experiment, nothing would ever have been accomplished. But beyond that, Christian has a boundless curiosity, be it about physics, film, casinos, literary theory, or the finer points of American culture. Ed has one of the fastest minds I've encountered,

and it's been a challenge trying to keep up. Our contrasting styles have meshed well, and every once in a while after I've slowly caught up I've managed to convince him that I'm right. The range of his interests, reading, and knowledge, are something I aspire to. But please, Ed, can you learn to use the aesthetically correct staircase to the 2nd floor? Ralf was an critical member of the group, tackling all the dirty work that we threw his way. His love of python *finally* gave me somebody to talk programming with, but his musical tastes have forever ruined that one Portishead album for me. Yong's deep experience and knowledge were great to have on the team for an all-too-short time. Jonathan was a great partner in machine building endeavors, and his dedication to quantifying, measuring, and understanding the things we built was a crucial foil to my occasional sloppiness. I'll always fondly remember our vacuum chamber road trip up the eastern seaboard. But I fail to be convinced that there is anything even remotely interesting about fantasy football. Wujie's enthusiasm for physics experiments has been evident from his arrival, and in an amazingly short time has ramped him from novice to expert experimentalist. This is accompanied by an excellent sense of humor and positive attitude that I'm sure will propel the lab forward once it is under his command. Junru is the latest addition to the mix; I haven't had a chance to get to know him well, but I can tell he will add to the pool of unique talents that has characterized BEC2.

Outside of 26-259 and 26-256, the CUA hallway has been a wonderfully tight knit group. In fact, perhaps too tight knit – to our friends on the Fermi1 and Fermi2 experiments (Peyman, Cheng, Thomas, Waseem, Sara, Ibon, Peter, et. al.) yes, we *know* that you call our lab Wal-Mart behind our backs, and we also know that you *didn't return* most of those things you "borrowed". But we got the better end of the deal, getting to capitalize on your building wisdom and experience, and gathering motivational fuel from your collective enthusiasm. Andre, I'll never forget your handwritten note "I HATE the New Word Generator!". Your biceps failed to intimidate me during our many impromptu joke inappropriateness contests, but did you have to use so dern many cuss words? Ariel always seemed to understand my bizarre jokes, even when I didn't understand them myself, and was always ready with the per-

fect rejoinder. And, Ariel, I appreciate your commitment to classical-period-inspired naming conventions. Hiro, as I write this I realize that I still owe you a baseball glove. Marko, I'm glad our office could serve as the destination for you midnight wanderings. The *other* tall bespectacled Christian from Heidelberg, conventionally known as Schunk, you had an endless supply of good cheer, presumably replenished by those sweet boozy Feuerzangenbowles that you annually prepared for us. Dave Weld, I've already made two Lebowski references in this section, and I fear any more would be indecorous, but take it as stated that your literacy is not unnoticed. Tout, thanks for letting me borrow your fellow Ontarian Timur from time to time; inter-provincial cooperation like this helps reduce BC's western alienation. To the many other hallway participants, all of whom I could not possibly list, thank you for making the rich environment richer.

I want to thank Joanna for solving all the administrative problems that I created for myself over the years. Al, on the RLE facilities team, thanks for going to bat for us when we needed to face the wider MIT facilities inertia. Mark at the Edgerton machine shop has been a crucial and under-appreciated resource for many students faced with a perplexing machining operation.

Vladan, my academic advisor, has always been a source of calming guidance. Ike, thanks for the many useful discussions on matters ranging from the minutely technical to the quantum philosophical. David Pritchard, thanks for providing such a wonderful welcome to the community, I'll always remember the beautiful sailing excursions.

I think I may be the only remaining graduate student who overlapped with Martin's time as a grad student (for only a few days). Now I'm proud to count him as a member of my thesis committee. Martin's enthusiasm and gregarious energy are legendary, and made him like an unofficial second advisor to me.

Last and most certainly not least, I'd like to thank Wolfgang for making all of this possible. Wolfgang takes fresh faced grad students with little experience, and gives them a staggering amount of trust, freedom, and an array of resources that is dizzying. This has given me the freedom to fully explore my interests, and find the

places where I could maximally contribute, in a manner I doubt I will ever find again. Thank you for the opportunity.

Contents

List of Figures

List of Tables

Chapter 1

Introduction

1.1 Background

1.1.1 Quantum complexity

In 1982, Richard Feynman gave a talk that is often credited with sparking into existence the study of quantum computing [21]. As he pointed out, physical systems can be hard to simulate with a computer. This is especially true of quantum mechanical systems, in which the memory required to represent a state and the time required to do computations with it increase exponentially with the number of degrees of freedom simulated. A classical state of N two-level objects can be represented by the N individual object states, whereas the full quantum mechanical state requires specifying the amplitude of all 2^N possibilities. And yet the universe, obeying physical laws, is able to simulate itself perfectly in real time. This suggests that machines taking advantage of quantum mechanics may be capable of computations that are not (efficiently) tractable with classical machines alone.

The apparent computational power of quantum computers, built out of quantum bits instead of normal bits, and unitary operations instead of logic gates, lies in their vastly larger state space compared with a classical computer of the same size, and is a field of enormous activity and interest [58]. A parallel branch of investigation, quantum simulation, uses Feynman's insight differently. Instead of building a gen-

eral purpose quantum computer to run quantum algorithms, can we build quantum systems which are analogues of those we wish to simulate?

1.1.2 Cold atoms as quantum simulators

Since the achievement of Bose-Einstein condensation [2, 16] and later Fermi degeneracy [17, 33] of neutral atomic gases, cold atoms have shown themselves to be an ideal resource for quantum simulations. Cold atoms are very quantum mechanically pure – the weakness of their coupling to the outside environment gives them long coherence times. Many textbook quantum phenomena, such as interference between matter waves, are readily realized with them.

The toolbox for manipulating and probing cold atoms is rapidly growing. Atoms can be imaged in absorption, phase contrast imaging, single atom detection via fluorescence [5] or even via electron microscopes [26]. Energies can be precisely mapped with RF spectroscopy [74, 9]. Two-body interactions can be tuned using Feshbach resonances [38, 18]. Defect-free periodic potentials for atoms (optical lattices) can be created by interfering laser beams. Atoms in individual sites can be manipulated [79], and sites can be ramped or even split using superlattice techniques [78]. Synthetic gauge fields which imitate a Lorentz force can be created optically [50]. Of course in practice, not all these things can be done at once.

1.1.3 Simulating condensed matter systems

The biggest splash made by cold atom quantum simulation has been in condensed matter physics. In particular, the BEC-BCS crossover (in which the Cooper pairs of Bardeen-Cooper-Schrieffer theory of type I superconductors connect smoothly to a condensate of diatomic molecules) has been an amazingly fruitful system to study. In the 9 years since the BEC-BCS regime was first accessed with cold atoms [29, 82], a close coupling between experimentalists and condensed matter theorists has shed light on pair size [73], clarified the role of spin population imbalance in suppressing superfluidity [74, 76], and by now it is theory that has to play catch-up to experi-

ments which have measured universal coefficients of the transition to superfluidity at unitarity [48].

Another natural system to attack is fermions in a periodic potential. This is the bread and butter of condensed matter physics. Here theory has a bigger head start on quantum simulation experiments, but the prospective payoff, new insight into high-T_c superconductors, is even more exciting. Real condensed matter systems can be messy, with lattice defects, long range interactions, phonons, intricate band structures, and complicated potentials all affecting the physics and making systems difficult to model exactly. And yet, a wide range of interesting physical phenomena can be captured by a much simplified model, the Fermi-Hubbard hamiltonian:

$$H = -J \sum_{\langle ij \rangle, \sigma} \left(\hat{c}^\dagger_{j\sigma} \hat{c}_{i\sigma} + \hat{c}^\dagger_{i\sigma} \hat{c}_{j\sigma} \right) + U \sum_i \hat{n}_{i\uparrow} \hat{n}_{i\downarrow} + \sum_i \epsilon_i \hat{n}_i \tag{1.1}$$

Here $\hat{c}^\dagger$ and $\hat{c}$ are the usual fermionic creation and annihilation operators, and $\hat{n} = \hat{c}^\dagger \hat{c}$ the usual number operator. The Fermi-Hubbard model describes two species of fermions in the first band of a lattice, hopping around strength with J, and with an on-site inter-species repulsion U. This is a hamiltonian that is eminently realizable with fermionic gases in optical lattices, and with tunability in U, J, chemical potential, spin imbalance, and other parameters.

Depending on choice of parameters and the system dimensionality, the Fermi-Hubbard hamiltonian leads to states as diverse as metallic conductors, band insulators, Mott insulators, antiferromagnets (Néel states), and (it is expected) d-wave superfluids. And understanding the simple Fermi-Hubbard model can advance our understanding of the more complicated real condensed matter systems which build on it. In particular, the remarkably high critical temperature cuprate superconductors, whose discovery in 1986 set off a revolution in condensed matter physics [6], is believed to be understandable in the framework of the 2D Fermi-Hubbard, but the complexities of real condensed matter systems and the difficulty in simulating many-body fermionic systems has made this connection the subject of vigorous investigation.

Reaching the more exotic ordered states of the Hubbard model, the Néel states

and d-wave superfluids, is one of the major goals in the community of quantum simulation, and the goal of our lab. Doing so will require exquisite control of experimental variables, advances in in-lattice cooling of atoms, and new ways to probe cold atom systems. The work in this thesis is aimed in this direction. New probes based on fluctuations have been applied to trapped atomic gases. And a versatile new apparatus has been constructed, which will be able to flexibly adjust between different lattice configurations and imaging configurations, able to work at high imaging resolution without sacrificing atom number, able to work with 2D or 3D systems, and be a reliable base for sophisticated experiments.

1.2 Outline of this thesis

This thesis will present progress towards experimental realization of exotic ordered states of fermions in optical lattices. It is organized as follows.

- **Chapter 2** will discuss the relevance of fluctuations in characterizing cold atom systems, and present experiments in which probes of fluctuations were developed and tested, and then applied to determine thermodynamic properties of bulk fermion systems. These experiments were performed in an apparatus that was subsequently decommissioned.

- **Chapter 3** will discuss a new control software system, developed to control our (and other groups') increasingly sophisticated experiments.

- **Chapter 4** will detail the design of a new atom cooling machine, intended as a next-generation general purpose fermion optical lattice machine, incorporating as much accumulated experimental wisdom as possible.

- **Chapter 5** will discuss future directions of the new experiment, and act as a conclusion.

Chapter 2

Fluctuations as a Probe of Many-Body Quantum Systems

God does not play dice.

Albert Einstein

Einstein, stop telling God what to do.

Neils Bohr

This chapter will discuss a series of experiments conducted in the old apparatus in our lab, studying noise and fluctuations in degenerate ^{6}Li Fermi gases [68, 69, 67]. For a more detailed treatment the reader is referred to the thesis of Christian Sanner [66] who was the main driver of these experiments.

When confronting a new physical system, it is often most intuitive to think about its average behaviors, and tempting to gloss over underlying fluctuations as a distraction. The majority of atomic physics experiments are based on repeatedly producing cold atomic samples, prodding them, averaging over many resulting images, and extracting physical insight from these averaged images. The reason is natural – non-systematic technical noise sources can be averaged away compared to properties

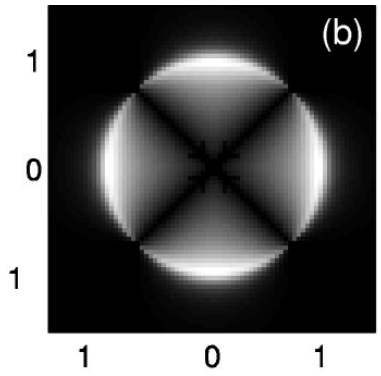

Figure 2-1: Predicted $d_{x^2-y^2}$ momentum correlations of a d-wave superfluid, mapped into position correlations after time-of-flight. From [1] .

of the ensemble average the system. But in performing this average, one is also averaging over fluctuating properties of the system under study, fluctuations which if measured can tell you about correlations that are not revealed in the average, correlations whose origin can range from simple quantum statistics to complex many-body interactions. Being able to see these fluctuations requires a sensitive experiment, in which technical noise sources are small and well-understood enough to separate them from the system fluctuations being measured.

Consider two of the benchmark phases of the Fermi-Hubbard model: antiferromagnetic ordering and d-wave pairing. Both phases are characterized by the onset of a new two-particle correlation, the antiferromagnet by a checkered magnetic order $\lim_{|x_i-x_j|\to\infty} (-1)^{i-j} \langle \sigma_i \sigma_j \rangle = N_0^2$ where spins σ_i and σ_j are correlated over long distance $|x_i - x_j|$, the d-wave superfluid by momentum space correlations with a $d_{x^2-y^2}$ character (see Figure 2-1).

Real-space correlations, like those in the antiferromagnet, should have a signature in real-space fluctuations. Momentum-space correlations have also been amenable to probing via fluctuations. In experiments with s-wave molecular BECs, time of flight has been used to convert momentum correlations into correlations in the real-space density fluctuations [30]. Theoretical proposals for seeing such correlations in a d-wave superfluid [1] make a strong case that examining fluctuations will be a powerful probe.

The versatility of probing fluctuations provides the motivation behind the tech-

niques developed in this chapter. Section 2.1 will give an overview of fluctuations, their source, and what they can tell us about the physics of a particular system. Section 2.2 will discuss a proof-of-principle fluctuation probing experiment, in which Pauli suppression of density fluctuations was observed in time-of-flight expanded clouds. In Section 2.3 we will introduce a method for probing fluctuations in-trap, when atom density is too high for normal absorption imaging, and apply this method towards interacting and noninteracting Fermi gases. This technique is then applied to strongly interacting Fermi gases, hunting for ferromagnetic domain formation, in Section 2.4.

2.1 What can we learn from fluctuations?

2.1.1 Shot noise and the $g^{(2)}$ function

When an ensemble of N particles are independently projected into a particular state, with probability per particle $p \ll 1$, the Binomial distribution tells us to expect a mean of $\mu = Np$ with a variance of $\sigma^2 = Np(1-p) \approx Np = \mu$. This is the ubiquitous "shot noise" of the Poisson distribution, which manifests itself in phenomena from clicks of a Geiger counter, to raindrops hitting a given patch of dirt, to the number of soldiers killed by horse kicks per year in the Prussian army [64].

Shot noise is a generic consequence of a system with many identical but uncorrelated events. Correlations between events can either enhance noise above the shot noise level ("super-poissonian") for positive correlations, or suppress it ("sub-poissonian") for negative correlations. In the context of atoms and photons, it is customary to discuss the two-particle correlation function $g^{(2)}(\Delta x, \Delta t)$ which tells you the probability of finding two particles at locations and times separated by Δx and Δt, relative to the probabilities of each individual measurement,

$$g^{(2)}(\Delta x, \Delta t) = \frac{\langle n(0,0) n(\Delta x, \Delta t)\rangle}{\langle n(0,0)\rangle \langle n(\Delta x, \Delta t)\rangle} \tag{2.1}$$

where $\langle \cdots \rangle$ indicates an ensemble average, and where n is particle density or probability density for occupation of a labeled state. For uncorrelated particles $g^{(2)} =$

1 everywhere. Any deviation from 1 indicates correlations. Systems with no long-range correlations may still exhibit interesting local correlations in $g^{(2)}$ near $(0,0)$. Enhanced values indicate particles that like to bunch together, and in which density fluctuations are enhanced relative to Poisson statistics, while suppressed $g^{(2)}$ values indicate anti-bunched particles and a suppression of shot noise.

2.1.2 The Hanbury Brown Twiss Effect

The fact that quantum mechanics permits indistinguishable particles can have surprising influence on the $g^{(2)}$ function and fluctuations, even in situations in which single-particle states look quite classical. Accounts of the history of studying the quantum mechanical sources of fluctuations typically begin with the astronomers Robert Hanbury Brown and Richard Q. Twiss, who had early insights into the bunching of photons, and who used a pair of photomultipliers to measure correlation between arrivals of photons of distant stars in order to measure their angular size [8]. At the time, without a well understood framework for thinking about lasers and coherent states of the photon field, these correlated photons were the source of much confusion. Hanbury Brown and Twiss in fact refer to measuring properties of "coherent" light sources, though in modern terminology we would refer to their observations as applying to chaotic light (from a thermal source) and emphatically not true for coherent light (lasers) which exhibit true Poisson statistics.

Consider two point sources of particles S_1 and S_2 and two detectors D_1 and D_2. The quantum mechanical amplitude for a detection at D_a due to a particle from S_b is $\langle S_b|D_a\rangle$. There are two trajectories by which a particle can be simultaneously detected at both detectors: $(S_1 \to D_1, S_2 \to D_2)$ and $(S_1 \to D_2, S_2 \to D_1)$. If the particles are indistinguishable then the amplitude for each of these trajectories must be combined, so the probability for a joint detection is $|\langle S_1|D_1\rangle \langle S_2|D_2\rangle \pm \langle S_2|D_1\rangle \langle S_1|D_2\rangle|^2$, with a $+$ sign for bosons and a $-$ sign for fermions. As the detectors are brought closer together, $\langle S_1|D_1\rangle$ and $\langle S_1|D_2\rangle$ must become equal (and likewise for S_2), so the joint detection probability for bosons approaches $4|\langle S_1|D_1\rangle \langle S_2|D_1\rangle|^2$ while for fermions it approaches zero. Compare this to the join detection probability if the particles were

distinguishable, $2|\langle S_1|D_1\rangle\,\langle S_2|D_1\rangle|^2$ (in which we add the probabilities of the two trajectories, rather then adding their amplitudes). This enhancement / suppression is the famous "boson bunching" and "fermion anti-bunching", in which the g_2 function goes to 2 for bosons and 0 for fermions at small length scales.

Coherent bosonic states of light (lasers) or matter (Bose-Einstein condensates) are purely poissonian and do not exhibit bosonic bunching. The above argument applies only in the case of multiple phase-independent sources, and not when particles are coming from the same macroscopically occupied mode.

Hanbury Brown and Twiss measured and used the eponymous Hanbury Brown Twiss effect (HBT) with photons. The range of the effect on the g_2 function is on the order of the coherence length of the light source. Even before the advent of lasers there were sources of reasonably narrow-band light and narrow interference filters which would be used on thermal sources. With atoms, the effect is harder to see, since the distance over which the g_2 function is enhanced or suppressed is on the order of the thermal de Broglie wavelength, and until the recent advances in laser cooling and evaporative cooling this was too severe a limit to make the effect practical to measure. Using cold atoms, the effect has by now been observed with both bosonic and fermion atoms. In an experiment with single-atom detection via a micro-channel plate the presence of the HBT bump with a thermal source of ^{4}He atoms was observed, with the bump absent as expected when the He atoms underwent the transition to a BEC [70]. Later ^{3}He, a fermion, was used and the HBT dip was also observed [39]. In a 1D system with normal absorption imaging, and in which the low dimensionality suppressed the transition to BEC even at low temperatures, the boson HBT bump was also observed [20].

The HBT effect gets more interesting with atoms in a periodic lattice. When a superfluid is released from a lattice, it will produce interference peaks after time of flight. Each site can be treated as a phase coherent source, and after time of flight atoms are only observed at locations where all the sources interfere constructively. When the phase coherence between lattice sites is lost (as in the bosonic superfluid to Mott insulator transition), the interference peaks disappear [31]. However, the

HBT effect does not require a phase coherent set sources (in fact it requires the opposite). Because of the periodic arrangement of incoherent sources, one can select pairs of detection position displaced from each other by Δx_a for which the two paths $(S_1 \to D_1, S_2 \to D_2)$ and $(S_1 \to D_2, S_2 \to D_1)$ have the same relative phase for any pair of sources S_α. Detectors at this relative displacement are, from an HBT standpoint, equivalent to having D_1 and D_2 on top of each other as in the earlier HBT discussion, and thus the $g^{(2)}(\Delta x)$ originally confined near $\Delta x = 0$ is now reproduced at $\Delta x = n\Delta x_a$ (for integer n). The HBT effect is a powerful tool to probe for periodicity in a system, even without the phase coherence requisite for seeing interference effects directly in average density. A series of experiments demonstrated HBT with ultracold atoms in a lattice, first with bosons [25] and later with fermions [59]. When anti-ferromagnetic states of atoms in optical lattices are eventually realized, finding a signature of the altered periodicity of the system with a technique such as this may be a key probe.

2.1.3 The fluctuation-dissipation theorem

Non-equilibrium fluctuations in a system are related to equilibrium thermodynamics of the system through the fluctuation-dissipation theorem. A system's equilibrium response function (such as compressibility) relates the change in some variable (such as density) in response to a drive term (such as pressure). The same response function determines the variable's thermal fluctuations. The textbook example is the grand canonical ensemble [22], in which particle number $N(\mu, T, V)$ is controlled by chemical potential μ. Fluctuations in N follow

$$\left\langle (\Delta N)^2 \right\rangle = k_B T \left(\frac{\partial \langle N \rangle}{\partial \mu} \right)_{TV} \tag{2.2}$$

where $\left(\frac{\partial \langle N \rangle}{\partial \mu}\right)_{TV}$ is the response function, a formulation of compressibility. The fluctuation dissipation theorem is a powerful way to think about the source of fluctuations. From this perspective, all fluctuations are thermally activated. The ideal gas, in which one expects Poisson density fluctuations even at zero temperature, is

pathological from this point of view – it behaves this way only because its compressibility diverges as $\propto 1/T$, preserving T independent fluctuations. This also indicates the usefulness of studying fluctuations – they can be used to determine response functions in situations where the drive terms cannot be manipulated directly, by observing a system's response to its thermally generated fluctuations (for instance, as in experiments with trapped atomic Mott insulators [24, 75]). Or, if response functions are known, fluctuations can be used as a thermometer.

2.1.4 Phase transitions, correlations, and domains

Phase transitions, be they quantum or classical, are accompanied by the emergence of new correlations in a system. A liquid freezing into a solid loses translational symmetry but gains a long range unit-cell correlation. Atoms undergoing transition to a BEC gain a long range phase coherence. Or, taking an illustrative lattice model, consider the quantum Ising model [65]

$$H_I = -Jg\sum_i \hat{\sigma}^x - J\sum_{\langle ij\rangle} \hat{\sigma}_i^z \hat{\sigma}_j^z \tag{2.3}$$

in which spins on a lattice have a ferromagnetic interaction in the z direction, in the presence of a magnetic field in the perpendicular x direction with strength set by g (the notation $\langle ij\rangle$ indicates summation over nearest neighbors). For sufficiently strong field $g > g_c$, the ground state $|0\rangle$ of this system is a paramagnet, with spins preferentially aligning along the x direction. In this state, z-component spin correlations decay exponentially, $\langle 0|\, \hat{\sigma}_i^z \hat{\sigma}_j^z \,|0\rangle \sim e^{-|x_i - x_j|/\xi}$. For low fields $g < g_c$, the ground state is a ferromagnet, with some spontaneous magnetization N_0 (either + or -, spontaneously breaking the symmetry of the Hamiltonian) and long range correlations $\lim_{|x_i - x_j|\to\infty} \langle 0|\, \hat{\sigma}_i^z \hat{\sigma}_j^z \,|0\rangle = N_0^2$. The critical field g_c sits at the phase transition, the boundary between these two correlation behaviors.

A signature of the phase transition is thus a change in the z magnetization fluctuations. Consider a probe of total z-magnetization $\hat{M}_z$ in some probe region V

containing N spins, $\hat{M}_z = \sum_{i \in V} \hat{\sigma}_i^z$ where $m_z = \pm 1/2$. In the strongly paramagnetic phase, with $g \gg g_c$ and $\xi \to 0$, each spin's m_z is independently projected, resulting in $\left\langle \hat{M}^z \right\rangle = 0$ and binomial fluctuations $\mathrm{Var}\,(\hat{M}^z) \equiv \left\langle \left(\hat{M}^z - \left\langle \hat{M}^z \right\rangle \right)^2 \right\rangle = N/4$. In a fully polarized ferromagnet, within a given ferromagnetic domain (i.e. for a certain choice of spontaneous magnetization $N_0 = \pm 1/2$), fluctuations in magnetization are suppressed, $\mathrm{Var}\,(\hat{M}^z) = 0$.

On the other hand, if the system is ferromagnetic but has broken into many independent ferromagnetic domains, fluctuations can be enhanced. If there are n spins per domain, then the probe volume will contain on average N/n independent domains, each with total magnetization $\pm n/2$. Each domain is independently projected, leading to $\mathrm{Var}\,(\hat{M}^z) = (N/n)(n^2/4) = n \times (N/4)$, an enhancement by a factor of n compared to the binomial fluctuations of the paramagnetic phase. This is a powerful property, because it means that even for a large probe volume V where individual domains cannot be resolved, there is a strong signature of domain size in the magnetization fluctuations.

2.2 Proof of principle experiment – density fluctuations in an ideal Fermi gas

This section expands upon *Suppression of Density Fluctuations in a Quantum Degenerate Fermi Gas*[68], which is attached as Appendix E.

2.2.1 Experiment overview

A manifestation of fermion anti-bunching is that at low temperatures a gas of fermions will have no atom shot noise. Consider a Fermi gas in which we can count the number of atoms in some probe volume – or equivalently, count the number of atoms in some set of elementary phase space cells ($\Delta x \Delta p = \hbar$). The Fermi-Dirac distribution tells us the probability $p(\epsilon)$ of a state with energy ϵ is $p(\epsilon) = \left(e^{(\epsilon-\mu)/(kT)} + 1\right)^{-1}$, where μ is the chemical potential. As the temperature approaches zero, this approaches a step

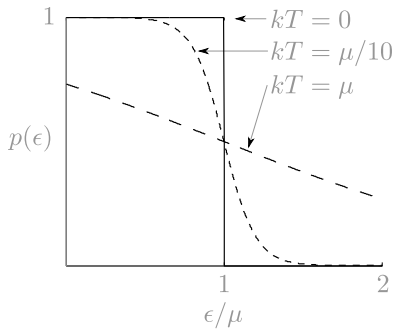

Figure 2-2: Fermi-Dirac distribution, for 3 temperatures.

cutoff (see Figure 2-2); phase space cells with energy below the Fermi energy will be occupied by a single particle, with probability 1, while cells above that energy will be empty. There is no room for fluctuations; all cells are either certainly occupied or certainly unoccupied. Repeatedly preparing this state and counting the atoms within the probe volume will always yield the same count. Equivalently, density fluctuations as $T \to 0$ are suppressed via the fluctuation dissipation theorem, due to the finite compressibility of a degenerate Fermi gas.

Our actual experiment was a close realization of the thought experiment. Clouds of ^{6}Li were repeatedly prepared and cooled to temperatures near or below degeneracy. Absorption imaging was used to determine the column-integrated density of atoms throughout each cloud. For each sub-bin of the cloud image, the variance in atom number in that bin was determined over the ensemble of prepared clouds.

In principle this experiment can be performed with trapped Fermi gases. However, for typical experimental parameters with ultracold atoms absorption imaging under these conditions has limitations. The very dense in-trap cloud is almost completely opaque to resonant imaging light, so useful absorption imaging requires either the use of detuned light, or small samples with high imaging resolution, both of which introduce their own complications[1].

The same experiment can be cleaner when taking advantage of a convenient property of non-interacting Fermi gases trapped in harmonic potentials – when you release

[1]Nevertheless, a similar experiment to ours was simultaneously performed in the Zurich group, using high resolution imaging to look at in-trap density fluctuations of a Fermi gas in a small sample [57].

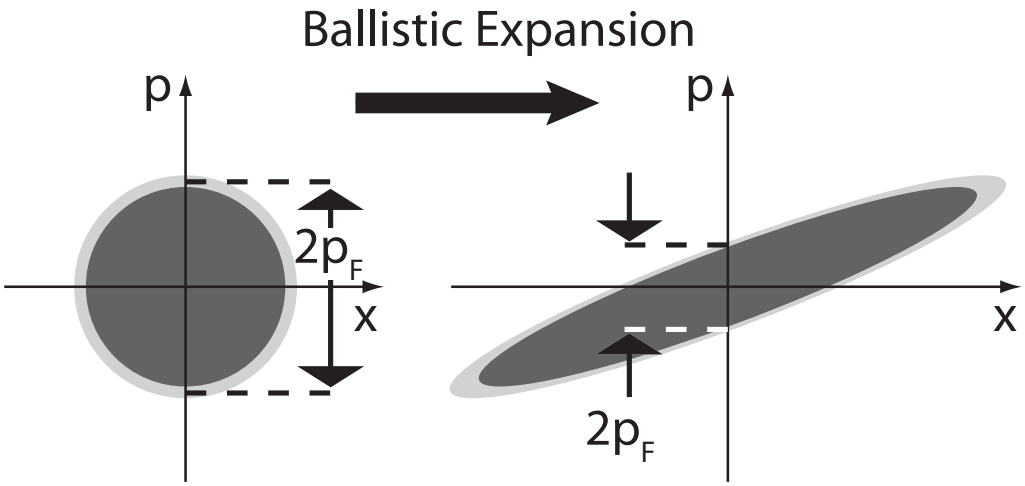

Figure 2-3: Ballistic expansion of a harmonically trapped Fermi gas. Fermi statistics are locally preserved in time of flight.

a trapped cloud by switching off the trap, the time of flight can be treated as a simple rescaling of coordinates. This is represented pictorially in Figure 2-3 , or mathematically in [32]. Initially, because of the position-momentum symmetry of the harmonic trap (in appropriately scaled units, the Hamiltonian is simply $H = \hat{p}^2 + \hat{x}^2$), the gas occupies a sphere in phase space. The cloud as a whole is a degenerate Fermi gas, but if the system contains many phase space cells ($\Delta x \Delta p = \hbar$) then the local density approximation allows us to think of the system as a collection of local Fermi gases, each with their own chemical potential, but with the same temperature. When the trap is turned off and the cloud begins to expand ballistically, the sphere in phase space begins to shear. Everywhere the gas now looks, locally, like a moving Fermi gas, with its own Fermi energy. The temperature is the same everywhere, but decreases as the cloud expands ballistically. And at every location the local T/E_F is the same as it was for the corresponding unscaled in-trap position under the scaling $x \to \left(\sqrt{1+\omega^2 t^2}\right) x$ (though if the trap is anistropic, the temperature in the expanded cloud can be anisotropic). Thus, time of flight ballistic expansion simply magnifies the cloud profile and the relative fluctuations.

2.2.2 Observed Noise Suppressions

Figure 2-4 shows the results of this experiment, for two cloud preparations (hot and cold). For each image bin, the atom number and atom number variance are depicted. In a cloud with Poisson fluctuations, one would expect these images to be the same. As the cloud temperature is lowered well below the Fermi temperature, the variance is suppressed. For the same set of clouds, the number measured atom number variance is plotted as a function of atom number in Figure 2-5. Suppression of fluctuations is highest near the center of the cloud, where the density is highest, and where even the hot cloud shows some suppression of fluctuations (the trap depth limited the maximum temperature of clouds that we could use). In the wings of the cloud, where the atom number is low, the hot cloud follows expected Poisson noise, while the cold cloud shows noise suppression. Profiles of observed atom number variance, for 3 different cloud temperatures, are shown in Figure 2-6, from which the cloud temperatures was inferred, demonstrating the capabilities of noise as a thermometer.

2.2.3 Fluctuation dissipation theorem

The appropriate formulation of the fluctuation-dissipation theorem for our experiment is $(\Delta N)^2 / \langle N \rangle = n k_B T \kappa_T$, where n is the density of the gas, and $\kappa_T = -\frac{1}{V}\left(\frac{\partial V}{\partial P}\right)_T$ the isothermal compressibility. An ideal Fermi gas with Fermi energy E_F has a finite compressibility of $\kappa_T = 3/(2nE_F)$ as $T \to 0$. This finite compressibility leads to the suppressed density fluctuations at low temperatures, by a factor of $3k_BT/2E_F$.

2.2.4 Experimental challenges

Accurately determining atom shot noise fluctuations by repeated preparation of clouds prepared a number of unique experimental challenges, described in detail in Appendix E and [66].

Atom shot noise is being measured by absorption imaging, in the presence of photon shot noise, which is always poissonian and for low light intensities this can dwarf the atom shot noise signal. This would seem to argue for using high intensities, or

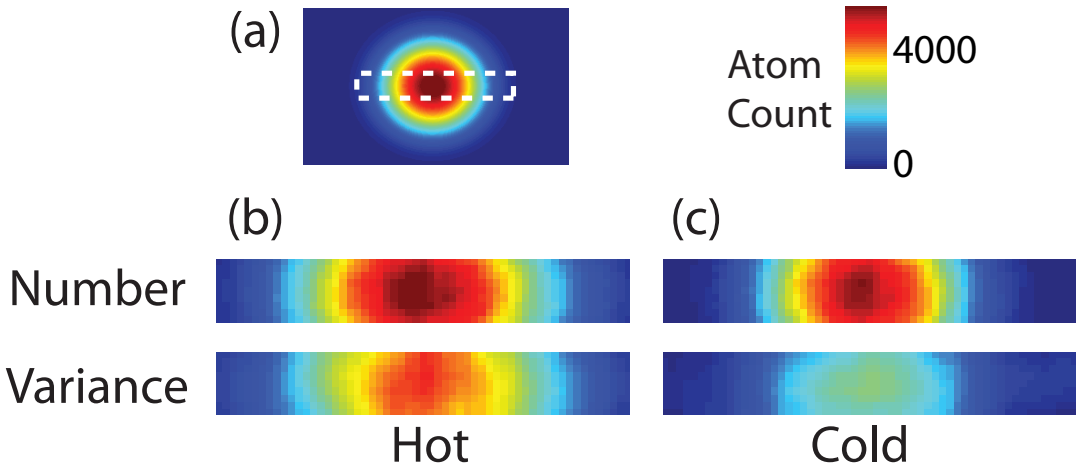

Figure 2-4: Spatial distribution of atom shot noise in Fermi clouds. For poissonian fluctuations, the two images at a given temperature should be identical. The variance images were obtained by determining the local density fluctuations from a set of 85 images taken under identical conditions. (a) Two dimensional image of the optical density of an ideal Fermi gas after 7 ms of ballistic expansion. The noise data were taken by limiting the field of view to the dashed region of interest, allowing for faster image acquisition. (b) For the heated sample, variance and density pictures are almost identical, implying only modest deviation from poissonian statistics. (c) Fermi suppression of density fluctuations deep in the quantum degenerate regime manifests itself through the difference between density and variance picture. Especially in the center of the cloud, there is a large suppression of density fluctuations. The variance images were smoothed over 6×6 bins. The width of images (b) and (c) is 2 mm.

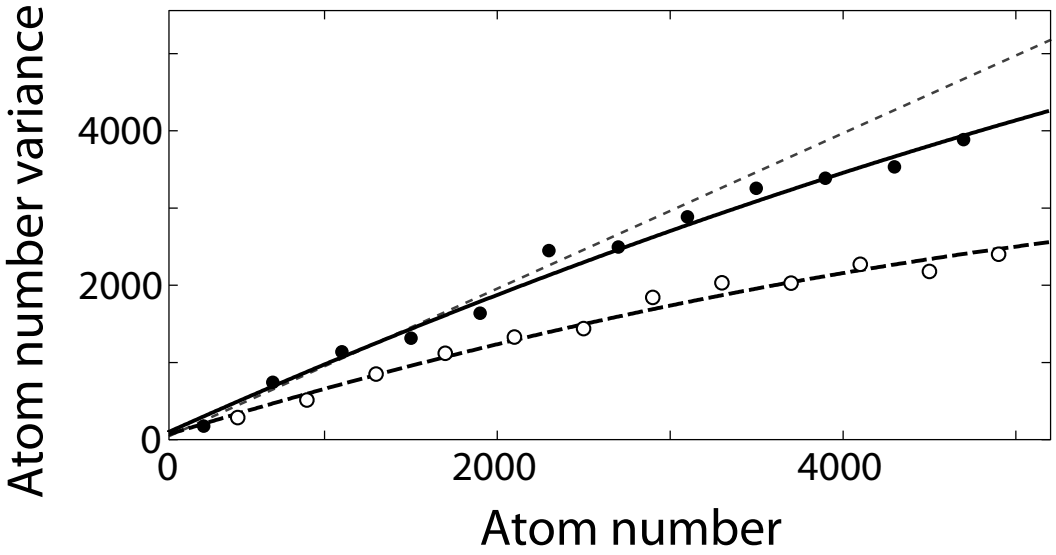

Figure 2-5: Atom number variance vs average atom number. For each spatial position, the average atom number per bin and its variance were determined using 85 images. The filled and open circles in the figure are averages of different spatial bin positions with similar average atom number. For a hot cloud at $T/T_F = 0.6$ (filled circles), the atom number variance is equal to the average atom number (dotted line, full poissonian noise) in the spatial wings where the atom number is low. The deviation from the linear slope for a cold cloud at $T/T_F = 0.21$ (open circles) is due to Pauli suppression of density fluctuations. There is also some suppression at the center of the hot cloud, where the atom number is high. The solid and dashed lines are quadratic fits for the hot and cold clouds to guide the eye.

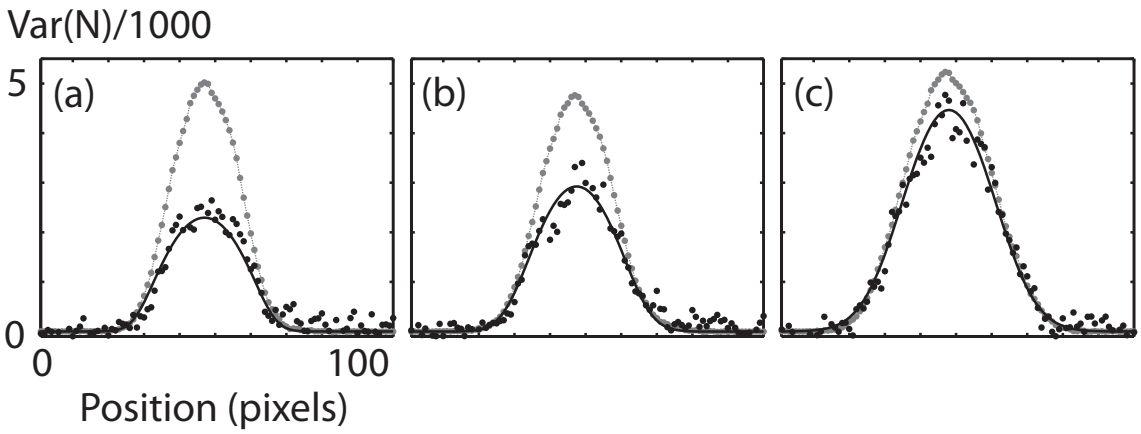

Figure 2-6: Comparison of observed variances (black dots) with a theoretical model (black line) and the observed atom number (gray), at three different temperatures (a, b, and c), showing 50, 40, and 15% suppression. Noise thermometry is implemented by fitting the observed fluctuations, resulting in temperatures T/T_F of $0.23 \pm .01$, $0.33 \pm .02$, and $0.60 \pm .02$. This is in good agreement with temperatures $0.21 \pm .01$, $0.31 \pm .01$, and $0.6 \pm .1$ obtained by fitting the shape of the expanded cloud[45]. The quoted uncertainties correspond to 1 standard deviation and are purely statistical.

scattering many photons per atom. However, saturation effects must be avoided. If atoms are driven outside of the linear response regime, then the usual image normalization technique of dividing a transmission image by an illumination image will pick up artifacts due to fringes in the imaging beam, again dwarfing the atom noise. Due to Lithium's very low mass, the dominant saturation mechanism is doppler shifting – after scattering $\sim$10 photons an atom picks up enough recoil momentum to to be doppler shifted on order of the transition linewidth. These two limits set a stringent illumination intensity range. To be sensitive enough, a camera with high quantum efficiency $> 90\%$ percent and no cover glass or other fringe-creating elements was carefully selected after trial and error.

Fringes in the imaging system were a major source of problems, especially due to the ease with which the glass cell vacuum chamber could be made to shake, causing the fringe pattern to be rearranged between probe and normalization exposures. The required a camera with a kinetics mode feature, to have minimal delay between exposures, and an atom depumping technique that could be applied between these shots to rapidly move them out of resonance for the normalization exposure.

After taking these steps to reduce technical noise, the measured atom number variance for bins that correspond to a particular atom number in the cloud themselves still had a lot of scatter, as can be seen in Figure 2-7. At first this effect that was attributed to residual technical noise. Counterintuitively, almost all of the remaining scatter is purely statistical in nature, caused by the underlying variance in sample variance. This is given by

$$\mathrm{Var}(\mathrm{Var}(N)) = \frac{(m-1)^2}{m^3}\mu_4 - \frac{(m-1)(m-3)}{m^3}\mu_2^2 \tag{2.4}$$

where m is the number of observations in each sample. The moments μ_2 and μ_4 are the central moments of the population distribution. For a Poisson distribution, $\mu_2 = \langle N \rangle$ and $\mu_4 = \langle N \rangle (1 + 3 \langle N \rangle)$

$$\mathrm{Var}(\mathrm{Var}(N)) = \frac{(m-1)^2}{m^3}\langle N \rangle (1 + 3\langle N \rangle) - \frac{(m-1)(m-3)}{m^3}(\langle N \rangle)^2 \tag{2.5}$$

where $\langle N \rangle$ is the population mean. For $m, \langle N \rangle \gg 1$, this is simply $2\langle N \rangle^2/m$. Note that this derivation was not presented correctly in the supplement in Appendix E.

2.2.5 The relationship between density fluctuations and light scattering

Density fluctuations and light scattering are intimately related. The scattered field at a given sample point is the sum of scattered field due to each individual atom. A sufficiently large collection of localized individual scatterers, if their spatial distribution is perfectly homogenous, will not scatter light. In all directions except the forward direction, the scatterers interfere destructively. Conversely, if the scatterers are disordered, with each scatterer location independently random (as in an ideal gas) then in non-forward directions the scatterer phases are independently random. The field of N scatterers is then a random walk of N individual scatterers, with an expected total amplitude $\propto \sqrt{N}$ and hence intensity $\propto N$. Equivalently, light scattering of a source beam off an object can be thought of in the Fourier domain, as a convolution

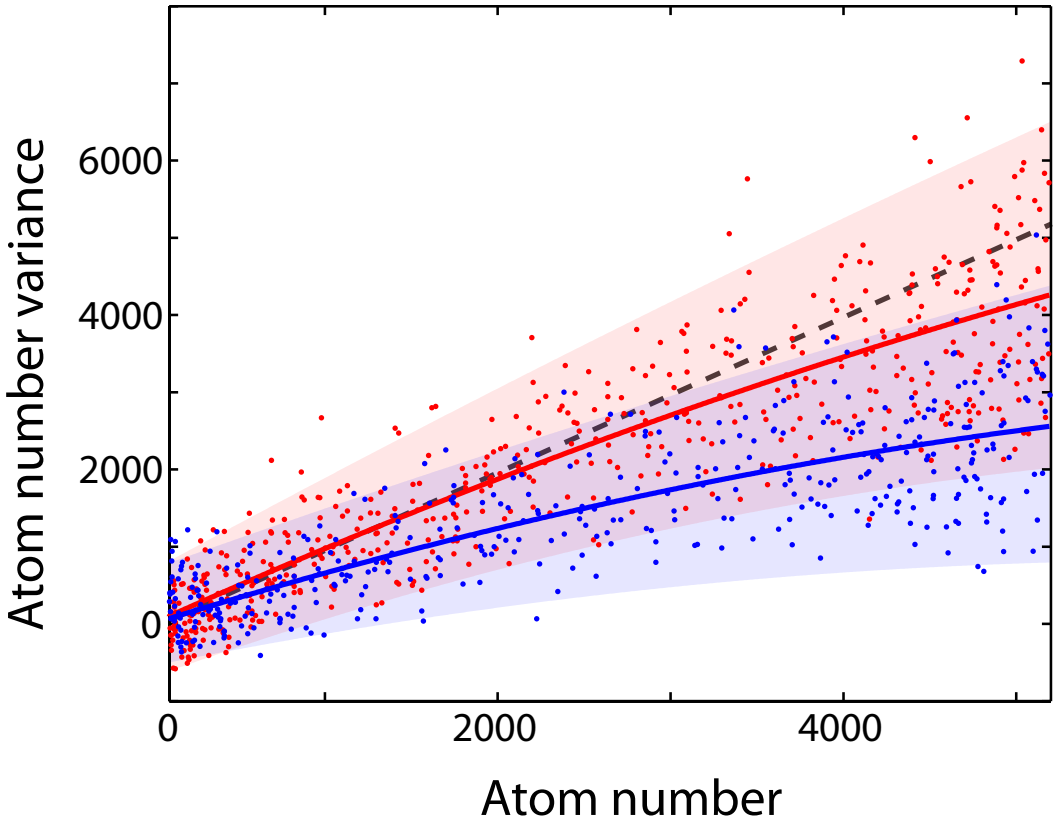

Figure 2-7: Atom number variance vs. atom number. Data for all of the resolution elements is plotted. This is the same data as used in Figure 2-5. Red points are from the hot cloud at $T/T_F = 0.6$, blue points from the cold cloud at $T/T_F = 0.21$. There is significant scatter in the variance data, and there are many "cold" pixels which actually have higher variance than their corresponding "hot" pixel. The red and blue shaded regions indicate the expected 2σ scatter in sample variance that is expected due to atom and photon counting statistics. The measured scatter agrees very well with the expected scatter, indicating that the scatter of the data is fully accounted for by counting statistics. Dashed line gives poissonian noise, and solid lines are fits to measured scatter, as in Figure 2-5. Negative values of the observed atom number variance result from the subtraction of photon shot noise.

between the spatial frequency spectrum of the source and of the scatterers. If the source is a plane wave (pure DC in the Fourier domain) then scattered light (non DC components after convolution) can only result from density fluctuations in the object (non DC components in the object's Fourier domain). This is captured by the structure factor:

$$S(q) = \frac{1}{N} \sum_{jk} e^{-i\vec{q}\cdot(\vec{r}_i - \vec{r}_j)} \tag{2.6}$$

where $\vec{r}_i$ is the position of atom i. Light is scattered at wavevector q with intensity $I(\vec{q}) = N|f(\vec{q})|^2 S(\vec{q})$ where f is the so-called "form factor", a property of the individual scatterers.

Quantum mechanically, light scattering means transfer of an input photon in some incoming state $|k_i\rangle$ into a scattered state $|k_i + \Delta k\rangle$, while simultaneously transferring the scatterer state from some initial state $|i\rangle$ to final state $|f\rangle$. For initial state with known momentum $|i\rangle = |k_{\mathrm{atom},i}\rangle$ conservation of momentum tells us that the matrix element for this scattering process will be nonzero only for $|f\rangle = |k_{\mathrm{atom},i} - \Delta k\rangle$. For a degenerate Fermi gas with a sufficiently high Fermi wavevector $k_F \gg \Delta k$, this matrix element is suppressed, since other than for $|i\rangle$ states very near the Fermi surface there are no unoccupied states $|f\rangle$ with the corresponding recoil momentum for the atom to scatter into. Equivalently, the structure factor $S_q < 1$ [62]. This is responsible for the widely predicted Pauli blocking of total light scattering in a deeply degenerate Fermi gas [28]. This is exactly equivalent to saying that a degenerate Fermi gas with a de Broglie wavelength substantially smaller than the probe light wavelength will have suppressed density fluctuations on that length scale, and therefore suppressed light scattering.

However, this is not the regime that our experiment has probed. Indeed, if light scattering had been suppressed by this mechanism, then absorption imaging (by which we determined column counts of atoms) would have been impossible, since absorption (i.e. light scattering) would have been suppressed entirely, and the atom clouds would have been transparent. In our prepared samples, $k_F \ll k_R$ where k_R is the

recoil momentum for a resonant 671nm photon. Light scattering at large angles is not suppressed, and therefore absorption imaging works as expected (with a slightly reduced cross section by about 0.3%). However, density fluctuations are suppressed for fluctuations with smaller $k < k_F \ll k_R$, corresponding to small light scattering angles that are collected by our imaging system, and hence to density fluctuations at length scales that are resolvable by the imaging system.

2.3 Measuring in-trap fluctuations with speckle

This section expands on *Speckle Imaging of Spin Fluctuations in a Strongly Interacting Fermi Gas* [69], reproduced in Appendix F.

The density fluctuations study made use of the convenient time-of-flight rescaling property of harmonically trapped Fermi gases, to allow us to study a noise property of the in-trap gas. Only a few special cases admit this trick (the noninteracting Fermi gas, or Fermi gases with interactions so strong as to cause hydrodynamic expansion). In particular, the property does not hold for atoms confined to a lattice or to general interacting Fermi gases. This led us to develop ideas for studying in-trap fluctuations in-trap, where resonant absorption imaging is impractical due to high densities. Somewhat accidentally, after trying to track down an anomalous source of noise in in-trap detuned absorption images, we stumbled upon a technique making use of speckle patterns formed by objects that randomize the phase of light.

2.3.1 What is speckle?

Laser speckle is one of the easiest laser phenomena to observe – anyone who has played with a laser pointer has noticed the grainy appearance that a laser spot has when viewed on a rough wall or sheet of paper. The speckle pattern is caused by the many out-of-phase scatterers of a rough surface, one that is bumpy on the scale of the laser wavelength or greater (any scattering surface fulfills this condition – if it wasn't bumpy on the optical scale, it would act like a mirror instead). These scatterers independently scatter with a random phase between 0 and 2π. Each resolution

element of your iris receives a random walk of scattered amplitudes, in certain places interfering destructively, and in others constructively. The correlation length of the speckle pattern in your iris is set by the numerical aperture of the imaging system.

Speckle has many counter-intuitive properties. For instance, the contrast of an observed speckle pattern does not depend on the scattering plane being in focus. This is one reason why laser pointer spots can be difficult for the human imaging system to focus on. For a thorough treatment of its many ins and outs the reader is referred to the definitive book on the topic [27].

Equivalently to looking at laser speckle off a rough surface, speckle can be observed in laser transmission through a phase randomizing object such as a ground glass diffuser plate. A diffuser will scramble the phases of different parts of a beam, imparting random random phases over 0 to 2π. Once the diffuser is rough enough to do this, increasing its roughness does not increase the speckle contrast (the ratio σ/μ where μ is the average intensity of the image and σ^2 is the intensity variance) – this is the "fully developed" speckle limit. If imparted phases are small compared to 2π, then the intensity contrast of the speckle pattern will be proportional to the range of random phases, and can thus be a probe of phase randomness.

To turn random phase into intensity contrast, some propagation distance is required. The phase randomizing elements have some characteristic grain size, and the light field must propagate by a distance on the order of the corresponding Rayleigh length in order for contributions from many grain elements to combine into a random walk speckle pattern. If the phase object is observed with an imaging system, then even with the imaging system focused on a thin phase randomizing object, intensity speckle will result if the numerical aperture of the imaging system cannot resolve the individual grains. In essence, this is because the finite resolution causes neighboring grains to blur into each other, restoring the random walk argument. The correlation length of the speckle pattern produced by an imaging system in this case comes from the numerical aperture of the imaging system, and not from the grain size of the diffuser.

Speckle imaging can considered a form a phase contrast imaging without a phase

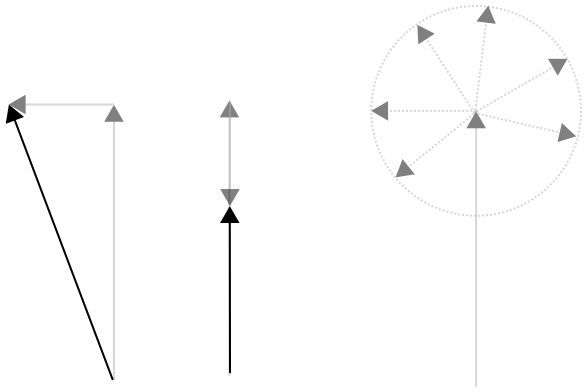

Figure 2-8: Left: an object which imparts a small phase shift to imaging light can be represented as a source with phase $\pi/2$ relative to the illumination beam, yielding (to first order in source amplitude) only a change in the phase of resultant field. Center: an absorption object, which affects the intensity of the transmitted field, can be represented as a source with phase π relative to illumination field. This picture works in the spatial domain, or in the spatial frequency domain where the object phasors represent field at different spatial frequency components. Right – in the frequency domain, free propagation or imaging through a defocused imaging system imparts a different phase to different spatial frequency components. If the system is sufficiently defocused, the relative phases for different frequency components allow those source terms to scramble phase contrast into a mixture of phase and amplitude contrast.

plate. Phase contrast imaging is a common technique with ultracold atoms, applied almost immediately after condensates were first produced [3]. It is usually accomplished by inserting a phase spot into the Fourier plane of an imaging system, imparting a $\pi/2$ phase shift to the DC spatial frequency component of the light field. This allows the illumination beam into to interfere with light from the object plane that is in the phase quadrature, and converts phase differences into amplitude contrast.

When the phase object is random, if all that is desired is an intensity signal with contrast that is proportional to the amount of phase noise, a phase plate is not required. Simply defocusing the imaging system, so that a the different spatial frequencies components acquire relative phase allows half of the power (in the Fourier components sense) that was initially in the phase quadrature to convert to the amplitude quadrature (see Figure 2-8). The intensity image produced by this technique is not a reconstruction of the exact phase pattern present in the object, but nevertheless has a contrast that is proportional to the amount of phase noise in the object.

A side-by-side comparison of the generation of weak speckle and strong speckle

is depicted in Figure 2-9. A simple numerical simulation, corresponding to typical parameters from our experiment, is presented in Figure 2-10, with the source code reproduced in Appendix H. The simulation starts with a Gaussian illumination beam and a Poisson phase object which imparts random phase to the resolution elements of the simulation. The resultant field is Fourier transformed, and propagated by the defocus distance. The finite aperture of the imaging system is simulated by applying a low-pass filter in the Fourier domain. Then the field is inverse Fourier transformed to produce the observed intensity pattern. Alternatively, a phase spot is simulated in the Fourier domain before the inverse transform, to produce a simulated phase-contrast image. When the cloud is perfectly in focus, no speckle contrast is seen in the amplitude quadrature (normal absorption imaging), while full contrast is seen in phase contrast imaging. As the cloud is defocused, speckle contrast in the two quadratures is rapidly equalized at half the initial contrast, over a distance corresponding to the Rayleigh length of the imaging system. In separate simulations not plotted below, it was also shown that this speckle contrast is additive for many independent planes, meaning that the speckle contrast in an absorption image can be interpreted as coming from the column-integrated fluctuations.

2.3.2 Proof of principle experiment

In our experiment described in [69], speckle is produced by an in-trap two species Fermi gas. The gas is prepared with a mixture of the two lowest hyperfine states of ^{6}Li, conventionally labelled $|1\rangle$ and $|2\rangle$. The light used as a probe is tuned halfway between these two species' resonant frequencies, such that the detuning is ~ 40MHz for each, but of opposite sign for the two. At this detuning, the imaginary part of the atom polarizability (which contributes to absorption signal) is substantially reduced, avoiding the opaque-cloud problems of in-trap resonant imaging. The real part of the polarizability (which contributes phase shift to the light, or acts as an index of refraction) is dominant, and is opposite sign for species $|1\rangle$ and $|2\rangle$, meaning that for this probe light the local index of refraction is proportional to the density difference (or magnetization) $(n_1 - n_2)$. In a second data set for the experiment, the probe light

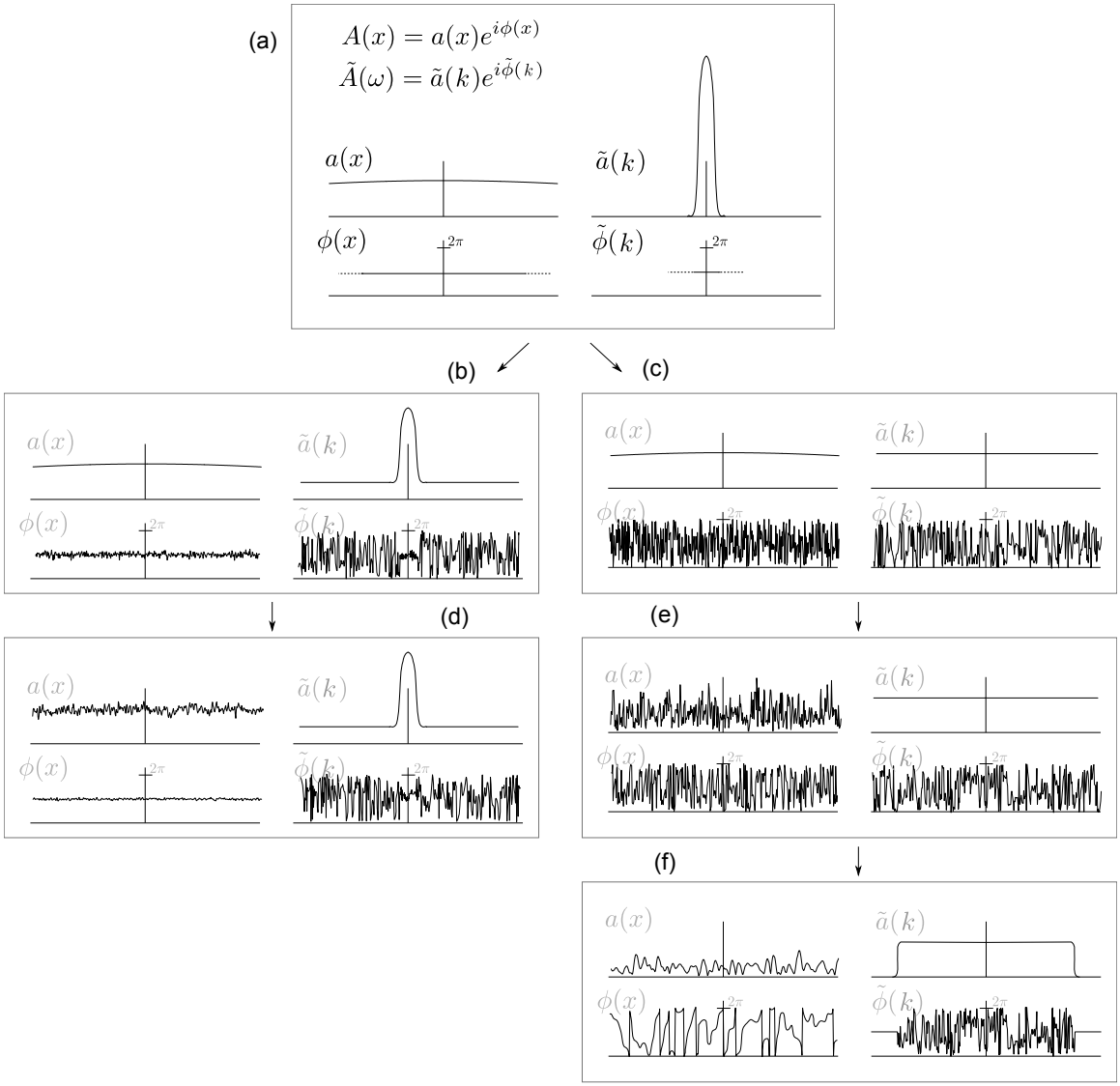

Figure 2-9: Evolution of phase noise into visible speckle. **(a)** An input gaussian beam with spatial field amplitude $A(x)$, with spatial Fourier transform $\tilde{A}(k)$. Light is incident on **(b)** a weak random phase object, with imparted random phase $\ll 2\pi$ or **(c)** a strong random phase object. In the weak phase case, the field still retains a strong component of the initial gaussian beam, whereas in the strong phase case all of initial gaussian component has been spread to higher frequencies. After the phase objects, the beam is propagated forward in space, adding relative phase shifts between frequency components and leading to **(d)** weak speckle or **(e)** strong speckle. For weak speckle, propagation converts half of the phase noise into amplitude noise. Amplitude fluctuations have a small contrast, proportional to the phase fluctuations in the object. For strong speckle case, amplitude fluctuations have full contrast, independent of the size of phase fluctuations in the phase object. **(f)** Imaging the strong phase object with finite resolution (applying a low-pass cutoff in the frequency domain) retains a full contrast speckle pattern, with a larger speckle size.

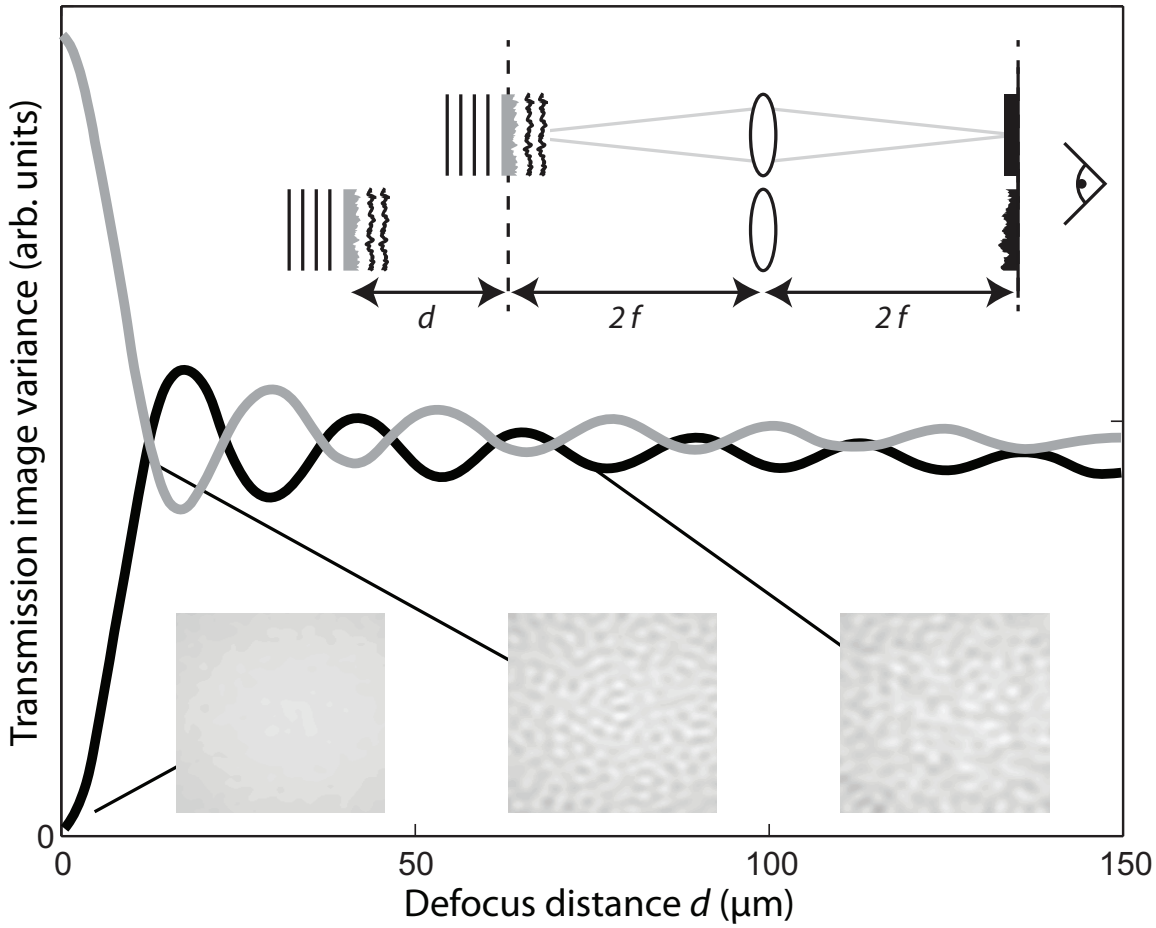

Figure 2-10: Simulation of propagation effects after light has passed through a poissonian phase noise object. Shown are the variance measured in the amplitude or in-phase quadrature (black line) and the out-of-phase quadrature (gray line) as a function of defocus distance, for an imaging system with a numerical aperture of 0.14. Within a distance less than 5% of our cloud size, noise becomes equally distributed between the two quadratures and the variances in transmission and phase-contrast images become the same. The oscillations in phase and amplitude contrast with distance are a numerical artifact caused by the discrete grid. (Top inset) For small phase fluctuations, an in-focus phase noise object gives no amplitude contrast, but when it is out of focus it does. (Bottom inset) Sample intensity patterns for a defocused phase object. The source code for the simulation which produced these plots is reproduced in Appendix H

is detuned ~ 40MHz to the other side of state $|2\rangle$ so that the detuning of both states is of the same sign, giving a local index of refraction $(n_1/3 + n_2)$. This second linear combination of densities allows us to determine fluctuations in both density difference and total density. The determination is cleaner for $(n_1 - n_2)$ – at this detuning the cloud has no overall average index of refraction (since the two densities are equal on average), and hence does not result in overall lensing, which produces some extra noise due to normalization artifacts.

Speckle imaging was applied to determine fluctuations in both total density and density difference, in both non-interacting and resonantly interacting gases. Pairing introduces a local correlation in density of $|1\rangle$ and $|2\rangle$ atoms, leading to reduced noise in the density difference $(n_1 - n_2)$ relative to $(n_1 + n_2)$ noise (see Figure 2-11). Or, in terms of the fluctuation dissipation theorem, noise in the total density $(n_1 + n_2)$ is proportional to compressibility κ as in the previous experiment, while noise in $(n_1 - n_2)$ is proportional to the magnetic susceptibility χ. The response functions determined in this experiment match well with theoretical calculations (see Figure 2-12).

2.4 Searching for domains of the Stoner ferromagnet

This section summarizes and slightly elaborates on *Correlations and Pair Formation in a Repulsively Interacting Fermi Gas* [67], reproduced in Appendix G.

One of the conceptually simplest phase transitions that can be realized with interacting Fermi gases is Stoner ferromagnetism. The Stoner model treats two species of repulsively interacting fermions, with a short range repulsive interaction characterized by a scattering length a. Consider a system of N fermions, distributed between two spin states $N_1 + N_2 = N$, in a box of volume V. The total energy of the system (at zero temperature) comes from the Fermi gas energy of each species, plus the repulsive interaction energy, giving $E = \alpha \times \left(N_1^{5/3} + N_2^{5/3}\right) + \beta \times aN_1N_2$ (system volume and mass dependent terms have been folded into terms α and β for clarity). For small

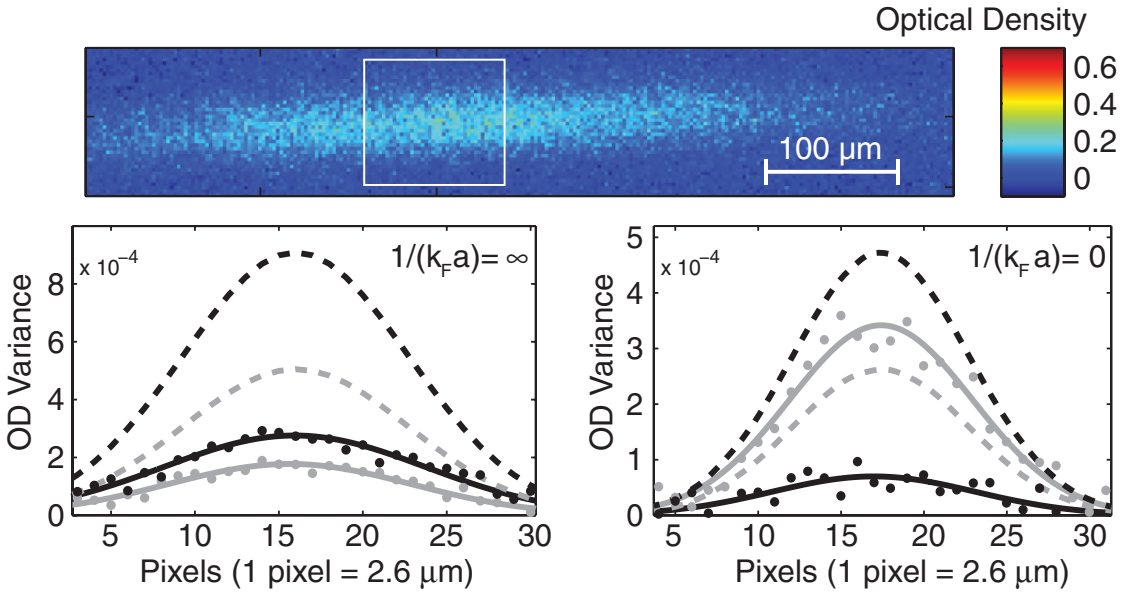

Figure 2-11: Example speckle noise image, with white box indicating analysis region. (Bottom panels) Noise data for noninteracting (left panel) and resonantly interacting (right panel) cold clouds, showing the variance in optical density for $n_1 - n_2$ images (black dots) and for $n_1 + n_2$ (gray dots). Solid lines are gaussian fits to the data, and dotted lines illustrate the expected full poissonian noise for the corresponding quantities based on density determined from off-resonant absorption.

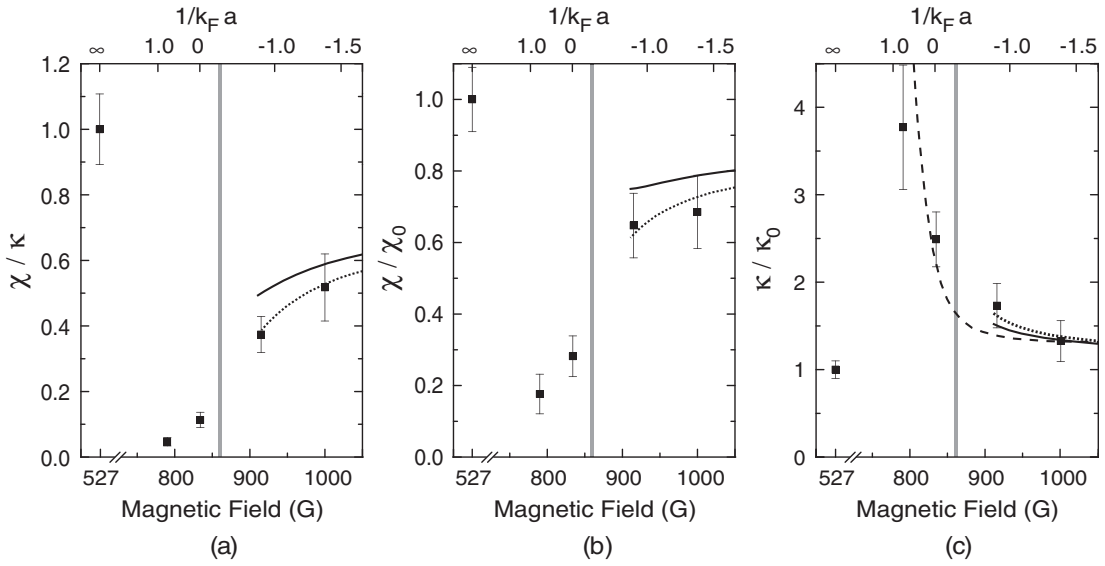

Figure 2-12: (a) The ratio χ/κ , (b) the normalized susceptibility χ/χ_0, and (c) the normalized compressibility κ/κ_0 in the BEC- BCS crossover. The variances derived from sequences of images are converted into thermodynamic variables using the measured temperatures and a calibration factor determined from the non-interacting gas. The vertical line indicates the onset region of superfluidity, as determined via condensate fraction measurements. The curves show theoretical zero temperature estimates based on 1st (dotted) and 2nd order (solid) perturbative formulas obtained from Landau Fermi-liquid theory integrated along the line of sight, and results from a Monte Carlo calculation (dashed) for the compressibility in a homogeneous system[4].

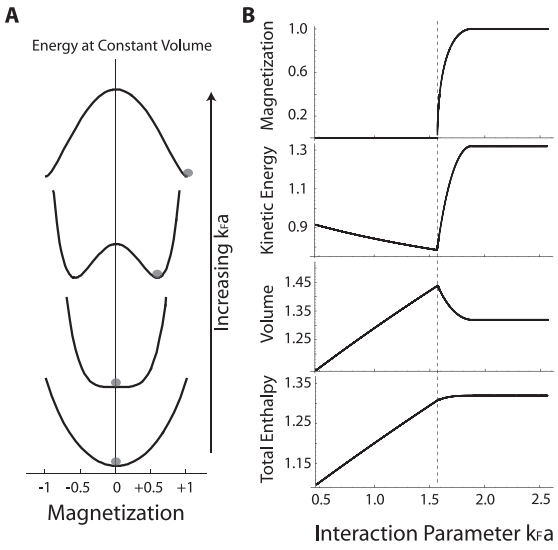

Figure 2-13: Stoner model of ferromagnetism. The onset of magnetization, as repulsive scattering length is increased in a two species Fermi gas. From [40].

repulsive interactions, with small $a > 0$, it is energetically favorable for the system to tolerate small repulsive energy in order to minimuze Fermi energy, and thus $N_1 = N_2$. But for a sufficiently high a, it becomes preferable for the system to spontaneously magnetize, such that either N_1 or $N_2 \approx N$. (see Figure 2-13)

A previous experiment, performed by our next-door-neighbor lab [40], found evidence of this phase transition in strongly interacting ^{6}Li Fermi gases. A noninteracting spin mixture of states $|1\rangle$ and $|2\rangle$ was prepared and confined in an optical dipole trap. Strong repulsion was quickly switched on by jumping the applied magnetic field near to the broad ^{6}Li Feshbach resonance. At these fields, ^{6}Li atoms are known to rapidly form diatomic molecules, which cause heating and trap loss and lead to a short lifetime of trapped atoms (this experiment measured properties of clouds with lifetimes as low as $\sim$5 ms). Nevertheless, by examining loss rate as a function of temperature and interaction strength a, a suppression of loss at low temperature and strong interactions appeared, which was attributed to the atomic samples phase separating into magnetic domains in which molecule formation could only occur at domain boundaries. Domains were never directly observed, but it was believed they were simply too small to be resolved and did not have time to grow during the short gas lifetime.

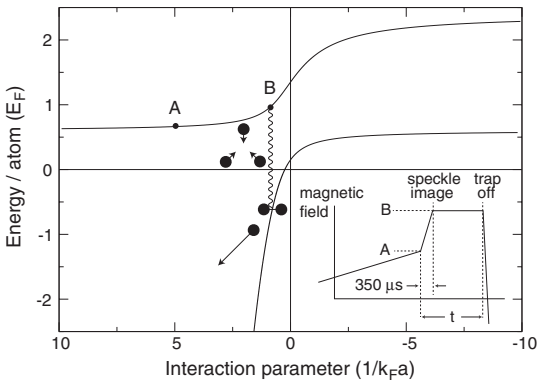

Figure 2-14: Diagram showing energy levels and timing of the experiment. The upper (repulsive) and lower (attractive) branch energies, near a Feshbach resonance, are connected by three-body collisions. In our experiment, we quickly jump from a weakly interacting Fermi gas (A) to a strongly interacting one (B) with a rapid magnetic field change. The evolution of correlations and domains and the molecule formation (population of the lower branch) are studied as a function of hold time t. Adapted from [63].

As discussed in earlier section 2.1.4, fluctuations in the total magnetization of a probe volume can be enhanced by the presence of domains, even when the domains themselves cannot be resolved. Our success in using fluctuation probes led us to try applying our speckle imaging technique to search for domain formation in a Stoner ferromagnet. Even small domains of only a few particles n per domain should lead to strongly enhanced fluctuations by a factor of n.

A similar preparation technique to that in [40] was used. The main difference was that our glass cell experiment did not suffer from eddy currents that make it difficult to achieve fast magnetic field ramps, and thus we were able to jump more cleanly and quickly into the strongly interacting region in about 350 µs instead of 4.5 ms (see Figure 2-14). After this quick ramp, speckle imaging was used to probe for magnetization fluctuations (in $n_1 - n_2$) in the sample. However, after a thorough search through parameter space, no strong enhancement of fluctuations was observed (see Figure 2-15). This appears to rule out the formation of ferromagnetic domains, and indicates that the conclusions of [40] were incorrect. Instead, the observed change in atom loss rate, previously attributed to phase separation, is believed to have been an artifact of the previous experiment's inability to probe very short timescales near

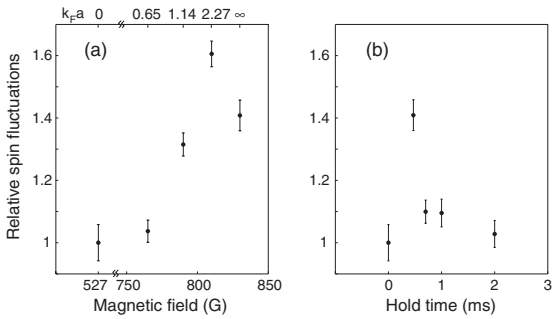

Figure 2-15: Spin fluctuations **(a)** after 350 μs as a function of magnetic field and **(b)** on resonance as a function of hold time scaled to the value measured at 527 G. Even at strong repulsive interactions, the measured spin fluctuations are barely enhanced, indicating only short-range correlations and no domain formation. The spin fluctuations were determined for square bins of 2.6 μm, each containing on average 1000 atoms per spin state.

the beginning of the strong interactions. Armed with faster magnetic field ramps, our experiment observed that atom loss was not simply exponential, but rather had a very fast initial decay followed by a much slower exponential tail (see Figure 2-16).

Whether the underlying assumptions of the Stoner model are realistic remains open to debate [61]. The Stoner model assumes a short ranged yet strong interaction. In systems like ours, which use a broad Feshbach resonance to achieve this interaction, the strong interaction goes hand in hand with a strong coupling from the scattering channel to a molecular state, and hence high loss rate. It appears possible that for any such system the timescale for formation of ferromagnetic domains will always be smaller than the timescale for molecule formation. Using a narrow Feshbach resonance would mean a lower molecular coupling, and hence slower decay rate, for the same achieved scattering length. But narrow Feshbach resonances cannot be treated as yielding purely short-range interactions, once again breaking the Stoner model assumptions.

2.5 Outlook

Fluctuation probes have shown themselves to be a very useful way to examine correlations in trapped atomic systems. In experiments performed already, these probes have

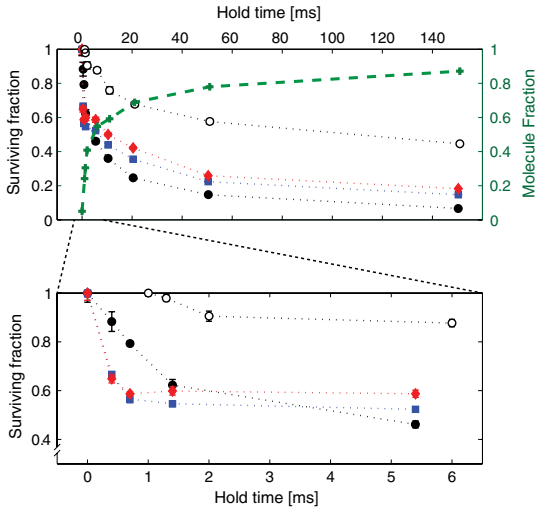

Figure 2-16: Characterization of molecule formation at short and long hold times, and at different values of the interaction strength. The closed symbols, circles (black) at 790 G with $k_F a = 1/14$, squares (blue) at 810 G with $k_F a = 2.27$ and diamonds (red) at 818 G with $k_F a = 3.5$ represent the normalized number of free atoms, the open symbols the total number of atoms including those bound in Feshbach molecules (open circles at 790 G with $k_F a = 1.14$). The crosses (green) show the molecule fraction. The characteristic time scale is set by the Fermi time $\hbar/E_F = 43\mu$s, calculated with a cloud averaged Fermi energy.

demonstrated classic textbook effects such as Pauli blocking of density fluctuations, and raised new questions about another textbook model, the Stoner ferromagnet. Such probes, especially speckle imaging, could prove to be a key technique in diagnosing new phases of atomic gases.

Chapter 3

The Cicero Word Generator

> My whole journey is in suspense till I receive letters from you all of the 1st of August. For if there turns out to be any hope, I am for Epirus: if not, I shall make for Cyzicus or some other place. Your letter is cheerful indeed, but at the same time, the oftener I read it, the more it weakens the suggested ground for hope, so that it is easy to see that you are trying to minister at once to consolation and to truth. Accordingly, I beg you to write to me exactly what you know and exactly what you think.
>
> Marcus Tullius Cicero (106-43BC), *Letters to Atticus*

This chapter is nearly identical to the manuscript *A Distributed GUI-based Computer Control System for Atomic Physics Experiments* [44], which has been submitted for publication.

3.1 Introduction

The study of Bose-Einstein condensates and degenerate Fermi gasses of trapped atoms are one of the most active and exciting sub-fields of atomic physics. Experiments require a sophisticated combination of vacuum, electronic, and laser technology. Most probes of condensates and degenerate gasses are destructive, so data is acquired by repeated "shots" in which a sample is prepared and then probed. A single shot in such experiments takes ∼10-60s to acquire, and requires several hundred precisely timed events, such as opening and closing of laser shutters, ramping and switching magnetic coils, RF evaporation sweeps, and camera triggers. Events may be as long as several seconds (the loading of a magneto-optic trap, for instance), or as short as a microsecond (a blast of laser light to remove unwanted atoms from a trap, for instance). Thus, these experiments require a computer control system capable of outputting a precisely sequenced set of outputs over a large number of analog and digital channels.

Such experiments are also by nature permanent prototypes, in a constant state of being upgraded, tweaked, repaired, and improved. Thus, it is desirable to have a computer control system that is intuitive to use, allowing for easy comprehension, design and modification of output sequence by users who are not experts in the control system's inner workings.

This paper describes a graphical-user-interface-based distributed computer control system developed at MIT for our experiments with ultracold atoms, called the Cicero Word Generator. The software has been used in Fermi gas experiments in the primary author's lab [68, 69, 67]. In addition, the package (and its source code) are freely available for download and use by other groups [42], and has been adopted in a number of atomic physics experiments [10, 81, 40, 71, 73, 36] in groups at over 10 institutions. While designed with BEC and Fermi gas experiments in mind, it is likely that Cicero (or ideas in its design and implementation) could be useful in other types of experiments where elaborate and precise output sequences are required.

Our system provides outputs both on hardware clocked channels, where precise

(∼10ns) timing without shot-to-shot variation is required, as well as on software clocked channels such as GPIB and RS232 (serial) interfaces where deterministic timing is less feasible and generally not required. For deterministic outputs, we use commercial National Instruments (NI) output cards, with the ability to use an FPGA to generate a synchronization signal that allows us to reach time resolutions of ∼100ns over effectively arbitrary length sequences. The deterministic output configuration is discussed in Section 3.4.1. GPIB and RS232 outputs, which run in less reliable software time, are described in Section 3.4.2.

Many experimenters in the field end up writing their own control software in-house, often in isolation from other groups, leading to a large duplication of effort. The authors are aware of a few other published accounts of control software systems that have been shared between institutions [53, 60, 23, 49]. This work is complementary to those, and is distinguished by the fact that it takes a graphical user interface approach to designing sequences (rather than the text-based sequence programming approach offered by others) and by its targeting of commercially available NI output hardware rather than custom made parts. There is a tradeoff between a potentially greater versatility and automation in the programming-interface approach, versus greater ease of use and comprehensibility of the graphical-interface approach, though we attempt to address this with certain advanced features of the graphical approach to be explained in 3.3.1.

An overview of the control system is presented in Section 3.2. The user interface is described in Section 3.3. The details of timing and synchronization schemes are described in Section 3.4.

3.2 Architecture

Cicero splits the job of designing and running output sequences using a client-server architecture. A typical Cicero and Atticus installation is depicted in Figure 3-1. The

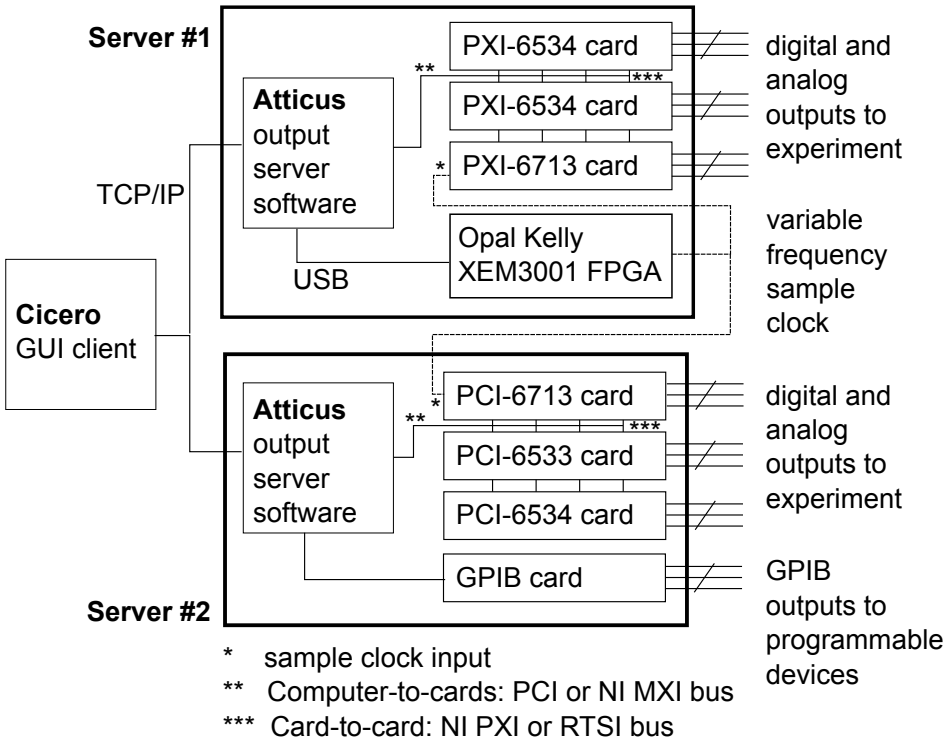

Figure 3-1: A typical installation of Cicero and Atticus, with two output servers. In this case, an FPGA is being used to synthesize a sample clock used to synchronize output channels.

client, generally referred to as Cicero[1], provides a graphical user interface for loading, saving, and editing sequences, and for starting runs. The server, Atticus, handles the output hardware configuration and converts high-level Cicero sequence objects into an output buffer for the output hardware located on the server computer. The client communicates with one or more servers over a standard TCP/IP network.

Splitting the output hardware from the user interface gives several advantages: it allows the system to scale to large numbers of output channels – more than could be supported by a single computer; it allows the system to be generalized to run on other types of hardware, without modification of the graphical user interface, by making other server implementations for different output hardware; and it allows for output hardware to be physically located close to its point of use, rather than necessarily being close to the experiment operator's computer.

An individual shot breaks down into several steps. First, Cicero sends to each server a high level sequence description. The servers turn the sequence description into output buffers for each of the channels hosted by that server. These buffers are loaded into the output card memory, and the cards are armed to begin output. Cicero then sends a trigger command to the servers, which depending on the configuration either initiates a shared sample clock, or outputs a trigger signal to cards using their own internal clocks. After the sequence has run, Cicero polls the servers for any errors encountered in the run. If no error was encountered, and Cicero is set to loop or scan over a parameter list, then Cicero repeats the process for the next shot.

3.3 User Interface

3.3.1 Client – Cicero

Cicero is a descendant of commercial Word Generator control hardware used in early atom cooling and trapping experiments at MIT, which through front-panel programming allowed users to pre-program and then run sequences of synchronized digital

[1]both the full software suite and the user interface client are generally referred to by the same name, Cicero, but the intended meaning is usually clear from context

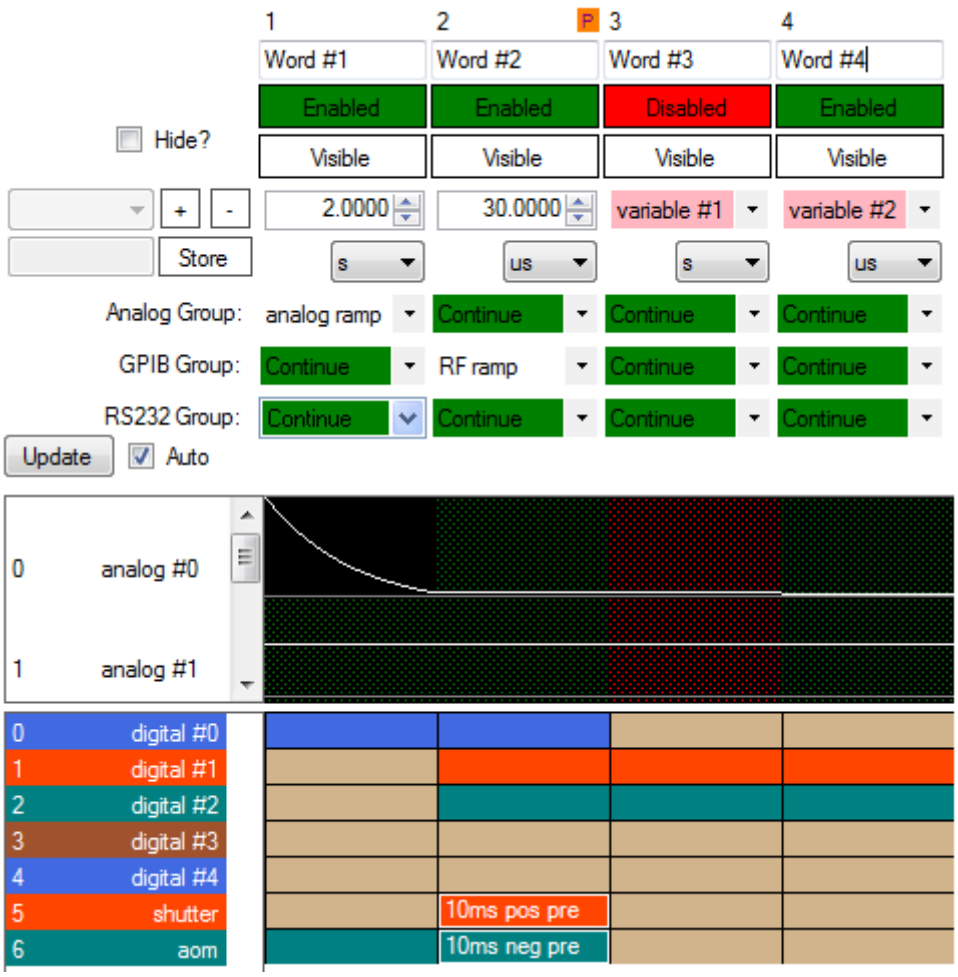

Figure 3-2: Screenshot of the main sequence editing user interface.

outputs over a collection of channels. These manually programmed devices were eventually succeeded by several generations of computerized control systems, based on custom software and computer integrated output cards, but retaining the basic sequence-of-words scheme and the historical Word Generator name.

A screenshot of Cicero's basic sequence editing user interface is depicted in Figure 3-2. A sequence consists of a series of words – columns of user-settable time duration. In each word, the user specifies the output value of digital channels using a grid of toggles. A word may optionally trigger ramps of analog output channels, or trigger GPIB or RS232 output commands.

The essential elements of the user interface were carried over from previous generations of control software. The interface is intuitive to people with no programming

experience, and by glancing at the sequence editing screen it is easy to see which channels are doing what when. Two key user interface enhancements have been introduced to alleviate many of the disadvantages of the GUI approach to the programming interface approach.

In our previous implementations of this basic GUI approach, it was extremely tedious to repeat a sequence while systematically changing a parameter, a task very common when collecting data or optimizing the apparatus. This has been alleviated with the introduction of variable parameters. Any numerical parameter in a sequence can be bound to a variable by right-clicking on it and selecting from a menu of defined variables. Variables can be assigned hard values, or defined in terms of other variables by entering mathematical formulae, or assigned to lists which can be scanned over, allowing the variable to take on a succession of values in successive iterations of the sequence.

In our experience with these experiments and previous GUI implementations, actions which are logically a single operation often required several words in the GUI to accomplish. A classic example is flashing on an imaging laser beam for a short pulse. Such beams are typically controlled by a combination of an acousto-optic modulator (very fast rise time, imperfect extinction ratio) and mechanical shutter (slow rise, perfect extinction ratio). The modulator must be kept pre-warmed for about a second before the pulse, but must be kept off during the slow shutter rise time ($\sim$10ms). This meant every imaging pulse word was accompanied by a pre-trigger word which turned off the modulator but began opening the shutter. Such pre-triggers could be extremely complicated if they overlapped with other pre-trigger words or other time sensitive phases of a sequence (such as the release of atoms from trap for a time-of-flight image). These problems have been alleviated in Cicero by introducing the ability to define more sophisticated digital actions than just turning on during a word. These actions are termed Pulses, and are created and edited in a special section of the GUI. They support a variety a pre- or post-trigger behavior, in essence allowing them to cause digital channel value changes at times that are specified relative to the boundaries of the word that the Pulse is placed in, but not

confined to the word boundaries. Pulses are then assigned to an individual channel at given word by right clicking on the grid of toggles (see word 2 of Figure 3-2). Using these pre-triggers can help ensure that each word of the sequence corresponds to one logical operation, making the sequence more modular, easier to read, and making it much less tedious to accomplish sequences with overlapping pre-triggers.

A slew of other client features have been incorporated as they have become needed, and an exhaustive description of them is beyond this paper's scope, but they include: the ability to loop a keep-warm sequence in the background while editing a sequence in the foreground; grouping a set of words into a module, allowing them to be batch-enabled, -disabled or looped; ramps and waveforms defined graphically or symbolically; logging of run details to explorable log files or to a database (SQL); persistent variables that can be referenced from multiple sequence files; and interspersing of calibration shots into a long set of parameter scanning runs.

3.3.2 Server – Atticus

The Atticus output server is quite versatile, able to communicate with a wide range of output hardware, in many possible timing configurations. This requires a certain amount of installation-specific configuration. Unlike much experiment-specific control software, Atticus makes all such configuration settings accessible to the user through a GUI, without needing to make changes to hard-coded parameters in the source code.

3.4 Output Details

3.4.1 Synchronization scheme for analog and digital channels

Our control system is built around NI output cards, specifically the PXI- and PCI-6713 (12-bit analog outputs, 8 channels) and PXI- and PCI- 6534 (32-bit output digital output). These cards allow for deterministic sequence output, without relying on unreliable timing supplied by a computer operating system.

Generically, all such output cards function in a similar manner. Before running the sequence, an output buffer for each channel is precomputed, containing the value that the channel will take on at each sample time. Part of the buffer resides in the card's on-board memory, while the rest resides on the controlling computer and is streamed to the card as necessary. To run the sequence, a start trigger signal is supplied to the cards, which initiates output generation. A sample clock signal advances each channel to the next sample in its buffer. By physically sharing the start trigger and/or sample clock signals (using a card-to-card bus if the cards are co-located, or a coaxial cable if they are physically separated) all the output samples of all cards in the experiment can be precisely synchronized.

In the simplest realization, a few cards on a single NI bus can share a sample clock that is generated by one of the cards' on-board oscillators. The time resolution of the output sequence (i.e. the shortest word that the sequence may contain) is then set by the the sample clock frequency. In our experience, some legacy PCI cards (still in use in labs at MIT) can only reliable sustain continuous sample generation at rates up to $\sim$50kHz. At rates above this, streaming from the computer memory to the card is not always able to fill the on-board buffer's fast enough. This translates to a shortest word size of 20μs.

In a typical sequence, a minority of the words in which no channel values are changing take up the majority of the sequence time (for instance during MOT loading or RF evaporation sweeps), but it is still desirable to have a few very short words for fast operations. When used with the naive fixed-frequency sample clock described above, the situation is the worst of two worlds. The shortest word size is inconveniently long compared to some of the fastest operations we may want to perform, but the vast majority of the buffer is filled with redundant repeated samples during long words just to achieve a high time resolution, meaning the buffer is both large and slow to generate, as well as insufficiently high resolution. The solution to these problems is to use a sample clock that is not fixed frequency.

Instead of a fixed frequency clock, a variable frequency clock can be synthesized, one that has edges only when the sequence calls for changes in the output values. This

synthesized clock can then be sent to the sample clock input of the output cards, and allows the buffers on those cards to be small even while the time resolution of the sequence is high. We have developed two schemes for creating a variable frequency clock, using either a normal digital output from an NI card, or using an FPGA. In both schemes, for simplicity, all output cards share the same sample clock, so that if any channel on any card needs to change values, all cards are updated. In addition, a clock edge will occur at each word boundary even if no outputs change. In practice, this reduces complications in the code while causing only a limited amount of redundant buffer generation.

NI Cards (such as PXI-6534) typically have two halves which can make use of separate output buffers and sample clocks. Half of a card can be sacrificed to provide a variable frequency clock output. If set up for this form of clock generation, a single large buffer for this synthetic clock is calculated for each sequence run, and the appropriate digital output of the card is then fed into the sample clock inputs of other cards. The synthetic clock buffer itself is clocked using the on-board oscillator of the card, typically at 1MHz, achieving an effective time resolution in the output sequence of 2μs (since the shortest interval in the output sequence requires at least two samples of the clock sequence, one positive trigger edge and one falling edge). The scheme works, but has downsides: Half of a digital output card has to be sacrificed; the very large synthetic clock buffer can take several seconds to generate for each shot, and requires a card with a large on-board buffer.

An alternate approach is to use an FPGA to synthesize the variable frequency clock. We have made use of the XEM3001 FPGA board available from Opal Kelly, which is inexpensive, simple, and provides an easy to use computer-USB-FPGA communication interface. The FPGA is programmed on each Atticus startup with custom clock-synthesis code. Instead of creating the large output buffer necessary for the output-card-synthesized clock, when using an FPGA Atticus merely computes a list of clock frequencies and dwell times for these frequencies. This list is transferred before each run to the FPGA over a USB connection. When the run is triggered, the FPGA begins synthesizing a variable frequency clock on the fly, by counting down

from either its on-board 10MHz oscillator or from an externally provided one. This translates to a time resolution of 100ns, (with a shortest word length of 200ns), vastly finer than needed in our experiments. None of the shortcomings of the synthetic clock buffer apply, since no large buffer needs to be precomputed.

Using an FPGA as the synchronization source also enables a basic form of real-time sequence feedback, namely the ability to pause and retrigger a run in response to some measurement. In the Cicero GUI, a given word can be marked with a "Hold then Retrigger" flag. After the FPGA reaches the part of the clock generation that corresponds to the beginning of this word, it pauses until receiving a retrigger signal on a dedicated digital input. Doing this retriggering in hardware with an FPGA (rather than in software, by having Atticus attempt to pause and resume output cards) allows it to be as fast and precise as any other hardware-timed event. Sequence retriggering of this type can help reduce shot-to-shot fluctuations caused by the environment, for instance by triggering certain parts of the experiment to coincide with a given phase of the AC mains line, or with the number of atoms loaded into a MOT as measured by fluorescence detection.

3.4.2 GPIB, Serial, and other output

In addition to the various digital and analog signals synthesized by output cards, laser cooling experiments often make use of programmable function generators and synthesizers to produce RF and microwave sweeps. A common and obvious example is RF evaporation, in which a synthesizer frequency must be precisely swept over a range of frequencies, often with a precisely tuned and non-uniform ramp profile. With legacy synthesizers, such as those from the Agilent ESG series, this is accomplished by issuing to the device a time-series of GPIB commands jumping the device to the desired frequency. Newer synthesizers, such as the NI-RFSG, accept commands from the computer using a much faster PXI interface. Many other function generators and translation stages accept commands over a RS232 ("Serial") port.

What all these communication methods have in common is that they require a computer to send the command at the correct time in the sequence, at least to the

best ability of a computer clock within the limitations of a non real-time operating system (though the authors recently became aware of a triggerable GPIB controller which can be pre-programmed in much the same way as our analog and digital outputs [35]).

These outputs are described as software clocked, to distinguish them from the hardware clocked outputs which do not rely on the computer's concept of time. Simply relying on a computer's on-board clock is often acceptable. The timing jitter of such an approach is generally less than 10ms, which is good enough considering that the GPIB command latency of a typical Agilent ESG synthesizer is over 100ms. In this mode, Atticus starts a thread at the beginning of a sequence run which continuously polls the computer's on-board clock. This is used to trigger the output of the correct GPIB, serial, or RFSG commands at the correct time in the sequence run.

In some circumstances, this timing scheme fails. When an FPGA clock is being used, along with the above described retriggering feature, any time the FPGA spends waiting for a retrigger translates directly into a skew between the software and hardware clocked outputs. If the retrigger waits are long, this can be an unacceptable long skew. Thus, Atticus can be configured to use a different method of software clocking – FPGA polling. In this mode, Atticus continuously polls the FPGA for its accurate sequence time (which takes into account any pauses and retrigger waits). This FPGA polled time is then used instead of the computer's on board clock to determine when commands are output. When configured to do so, the FPGA-derived software clock can be broadcast over the network using a lightweight UDP stream, both to the Cicero client so that the user interface can have a more accurate display of the sequence position, and to other Atticus hardware servers so that the software clocked events on that server can also be kept synchronized to the hardware clocked ones.

3.5 Conclusion

The Cicero Word Generator control system provides a user-friendly and powerful solution to the problem of running elaborate output sequences for atomic physics

experiments. This system should be generalizable to other types of experiments where realtime sequence feedback (beyond pausing and resuming an output sequence) is not required, and where a rapid and intuitive sequence editing user interface is desired. The separation of the software into a user interface program and an output program should also allow the system to be used with output hardware other that that described here, by writing a custom server implementation. It is the authors' hope that the software itself, or ideas described here, can be of use to other experimentalists.

Chapter 4

A New Apparatus for Lithium Optical Lattice Experiments

Any sufficiently advanced technology is indistinguishable from magic.

Arthur C. Clarke's Third Law

Any technology distinguishable from magic is insufficiently advanced.

Barry Gehm's Corollary

Any sufficiently advanced magic is indistinguishable from technology.

Unattributed

This chapter will discuss the design of our new experimental apparatus. It will focus on design details and decisions that are not often discussed. A familiarity with the basic techniques of atom cooling and trapping, and with the Sodium-Lithium cold fermion production approach, is assumed. For a thorough treatment of the

foundations, the reader is referred to a previous PhD thesis [34] and review paper [46].

4.1 Motivation for a new apparatus

The BEC2 lab was the second machine on the hallway to be upgraded from a Sodium BEC machine to a dual-species Sodium-Lithium machine (original Sodium-only machine described in [19], upgrade described in [15] and [55]). Because of its glass cell design, it was intended to be focused on fermions in optical lattices, and it produced an excellent set of early results – the first interference peaks of a fermionic superfluid released from an optical lattice [14], and an elegant study of the critical velocity for damping of fermions in the crossover between molecular condensates and BCS superfluids [54].

Nevertheless, working with lattices in the apparatus proved to be quite a challenge, and almost three years were spent trying to take these lattice experiments to the next step, without bearing much fruit. Much time was lost due to lattice alignment stability issues, IR laser breakdowns, and general fluctuations in cold gas production. When the experiment was working, some promising preliminary progress was made setting up experiments with optical slicing of lattice samples, with the hope of studying in-lattice density profiles and seeing incompressible shells of a fermionic band insulator and a Mott insulator. However, corrugations in both our optical slicing beams, and in the lattice beams eventually proved to be showstoppers. And meanwhile, competing experiments observed fermionic Mott insulators in different ways, first by seeing the suppression of doubly-occupied lattice sites via an RF-transfer technique [41], and later by studying the compressibility of a trapped sample by examining the cloud size when external confinement was varied independently of lattice depth [72]. Thus, for simplicity, we eliminated lattices from the equation and turned our attention to studying bulk systems with noise probes, ideas we had developed with lattice systems in mind but which were equally applicable in bulk. These fruitful investigations led to the results presented in Chapter 2.

Even studying bulk systems, the experiments were quite a challenge. In addition to the major daily effort required just to keep the machine stable and running, the glass cell design made noise experiments in particular a challenge. Because of the way the glass cell was mounted, suspended by two bellows between the Zeeman slower and the pump body, it had a tendency to vibrate. Due to the cell's lack of anti-reflection coating, these vibrations translated into quite severe moving fringes in the imaging system, which added strong remnant fringe artifacts to normalized transmission images. For experiments where only the overall cloud profile, or an average of profiles, was required, this was not a severe issue. But for the noise experiments, these fringes threatened to totally overwhelm the small fluctuations being measured, and required us to develop techniques to take pairs of images in rapid succession (see the thesis of Christian Sanner for a detailed discussion of cameras that make this possible, and their many subtle and surprising details [66]).

Against this backdrop, at the Sant Feliu BEC meeting in September of 2009, an inspiring collection of speakers both theoretical and experimental presented a compelling picture of the direction of the field of quantum simulation with ultracold atoms. Experiments were getting more technologically sophisticated and more specialized, some with high single-lattice-site imaging resolution [5, 75], or with phase-locked two-frequency lattices ("super-lattices", in effect lattices of tunable double-wells rather than simple sinusoidal lattices) [78, 11]. And theoretical proposals for exciting ways to address hard problems in condensed matter physics seemed to point the way to experiments with a high level of reliability and controllability. Our lab had been loosely considering the idea of a major upgrade already, but after this meeting it was concretely decided to begin designing and planning in detail.

We had a number of interrelated goals and improvements in mind when designing the new apparatus, which we have attempted to address by specific features of the new design.

- **Reliability:** The old BEC2 apparatus went through some periods of reliable operation, but these periods were the exception. Most days in which the experiment was to be run required 3-4 hours spent optimizing, tweaking, and coaxing

the machine back to proper performance, and often the apparatus was only stable enough to operate very late at night. We have attempted to address this by much better control of ambient temperature fluctuations (Section 4.7), by migrating to a solid state laser system for producing 589n, light (Section 4.8), by carefully considering the mechanical stiffness and stability of mounting techniques, and many other improvements.

- **Low complexity:** Intimately related to the above point, the previous experiment had many layers of unnecessary complexity, in part because of its history of upgrades, in which new features (a ^{6}Li MOT, for example) and subsystems had been tacked on over time, and new breadboards hung off the experiment in every conceivable location. In the new apparatus, we have tried to "design-in" as many basic features as possible to avoid this problem, for instance by having a dedicated system for delivering MOT light that does not interfere with future use of high value surfaces of the main breadboards. This was also one reason we selected a plugged quadrupole magnetic trap design, with its much simpler coil configuration, over our previous Ioffe-Pritchard design.

- **Versatility:** Many new cold atom machines are highly specialized, for instance the Quantum Gas Microscope from the Greiner group [5] and its offspring, an experiment which has produced spectacular results studying optical lattice systems with 1 or a few lattice planes, but is not well suited to studying bulk samples or large 3D lattices. We elected to continue the Ketterle group tradition of making general purpose cold atom machines, which may not be the ultimate tool for any specific study, but are adaptable to a wide variety of experiments.

- **Optical access:** The glass cell design of the old apparatus nominally provided almost 2π of solid angle optical access to trapped atoms. In reality, of course, most of this was obscured by magnet coils, and most of the access was afforded only at steep angles relative to the glass surfaces. From our lattice studies we began to understand that not all "optical access" is created equal, and that it is better to have near-normal incidence through glass surfaces than very steep

incidence angles. This eventually dictated the steel chamber with many windows approach that we used in the new apparatus.

- **Good imaging:** Our exploration of imaging techniques in the old apparatus convinced us of the need to design with a clean imaging system in mind. This means including vacuum viewports with a high enough numerical aperture for reasonably high resolution imaging (or, equivalently, for high light collection in fluorescence imaging, should future experiments make use of that), with working distances from the trapped cloud that are compatible with available microscopic lens systems, and with coatings than minimize reflections and fringes.

- **Excellent Vacuum:** To paraphrase an old IBM ad campaign, *nobody got fired for a higher vacuum*[1]. In particular, future experiments with Fermi gases in optical lattices may be even more sensitive to background gas collisions than cold atom experiments in general. Every practical effort was taken to eliminate outgassing sources in the chamber and to maximize the pumping speed, including application of a novel getter coating to the interior of the chamber.

- **Magnetic fields:** ^{6}Li has a broad s-wave Feshbach resonance near 830G, which is of huge importance in strongly interacting Fermi gas studies. This is a relatively high field, but readily achievable in an apparatus designed with high current electromagnets, and achieving at least this field was a minimal requirement. One goal of the DARPA OLE project under which the apparatus construction was funded was to achieve fast experimental cycle times, allowing an apparatus to rapidly map out phase diagrams of condensed matter systems, for instance. One long phase of the experiment, magnetic trap evaporation, can be shortened by having higher compression traps, so a relatively ambitious benchmark of 1000 G/cm for the achievable magnetic field gradient also guided the design of the coils.

[1]Except perhaps a Ti filament.

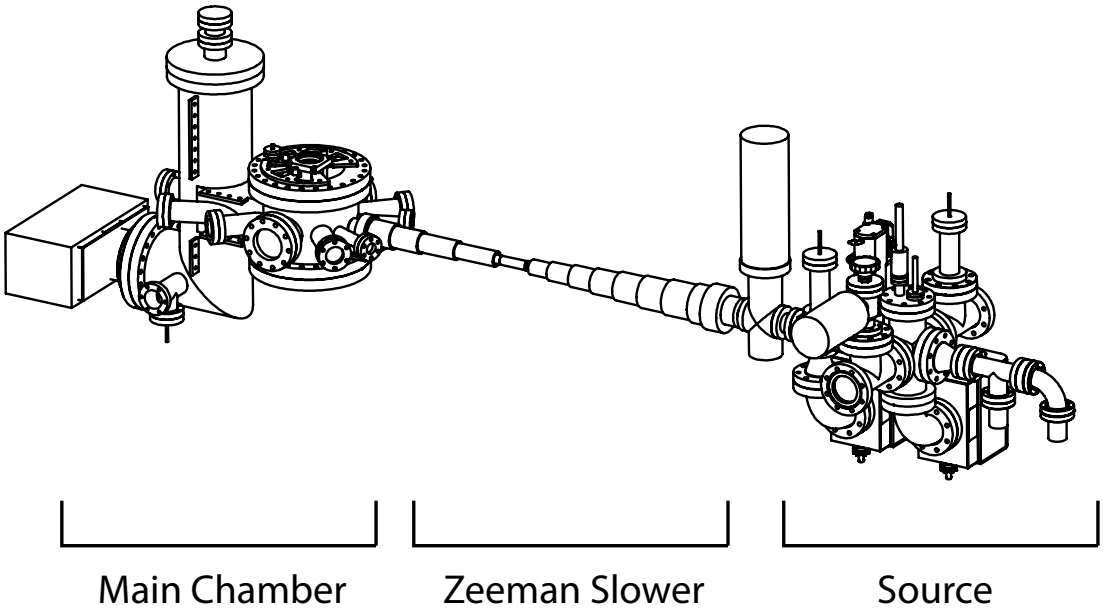

Figure 4-1: Overview of new apparatus. Heated cups containing Sodium and Lithium (far right) act as atom sources. An oven chamber houses a beam-shutter mechanism, followed by an intermediate chamber for differential pumping. Atoms then pass through a Zeeman Slower (center), and arrive in the main chamber (left) where all experiments take place. The main chamber is a custom steel chamber with numerous viewports for optical access, magnetic coils close to the atoms, and a L-shaped pump body accommodating an ion pump and Titanium sublimation pump.

4.2 Chamber layout and viewports

An overview of the design is presented in Figure 4-1. The apparatus follows the same basic pattern as previous generations of Sodium-Lithium experiments in the Ketterle group. A two-species oven [77] acts as the source for ^{23}Sodium and ^{6}Lithium atoms. The oven chamber holds a collimating plate and a mechanical atomic beam shutter. Unlike previous experiments, the motion feedthrough is a magnetically coupled linear motion feedthrough (Lesker MPPL16-150-H) to avoid potentially leak-prone bellows. The oven chamber is connected, through a differential pumping tube, to a small intermediate chamber with its own pump. A second stage of differential pumping connects the intermediate chamber to the beginning of the Zeeman slower. The oven-intermediate and intermediate-slower interfaces can be sealed off with VAT gate valves, allowing the main chamber to be kept under vacuum during oven refills (and

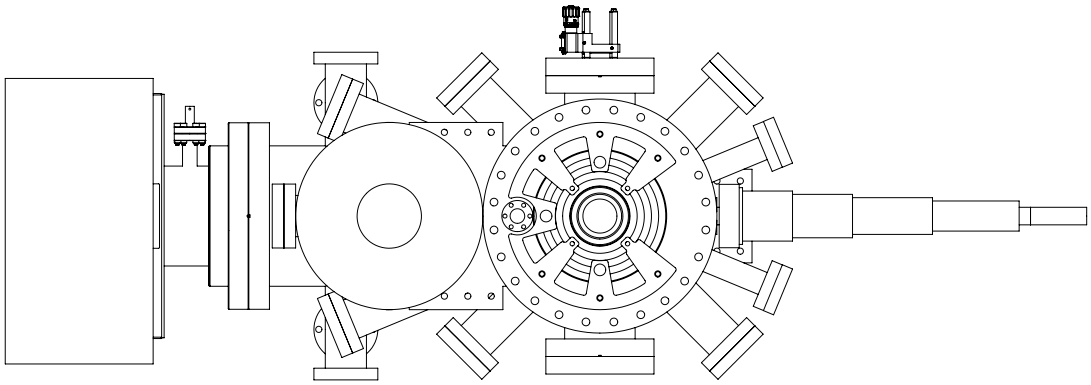

Figure 4-2: Top view of main vacuum chamber.

hopefully the intermediate chamber too, though the long term sealing performance of VAT valves in an alkali-heavy environment is not fully known from experience). The slower ends in a custom-built steel vacuum chamber, the "main chamber", in which all cooling, trapping, and subsequent lattice experiments take place.

The main chamber is designed to provide as much optical access as possible, and to accomodate reentrant bucket windows on two axes to allow for strong magnetic fields and field gradients and high resolution imaging. The basic top plan is presented in Figure 4-2, while a view showing the tight squeeze of the various reentrant buckets is depicted in 4-3. A fully detailed and dimensioned drawing of the main chamber is available in Appendix A, and of the bucket windows in Appendix B.

Horizontal mounting plates allow the main chamber to be held up by 3 contact points (in addition, the weight of the large ion pump is separately supported by a lab jack). Vertical mounting plates allow for a small vertical breadboard mounted to the chamber, for delivery of slower light.

4.2.1 Bucket windows

Like previous steel chamber experiments, the experiment makes use of custom reentrant "bucket windows" – these viewports allow the chamber to make use of standard Conflat vacuum fittings, while also allowing for windows and coils to be brought much closer to the atom cloud position than would be possible with standard flat viewports.

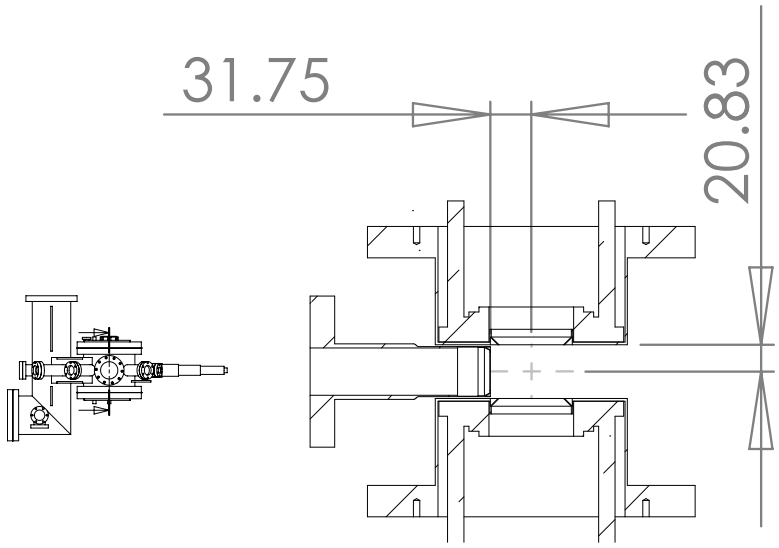

Figure 4-3: Section view of the main chamber, depicting positioning of top, bottom and side bucket windows. Side bucket is designed to fit with 1mm of clearance. High current magnet coils are shown, along with their mounting rods, in the top and bottom buckets. Dimensions are mm.

The main chamber accommodates bucket windows on its two vertical 10" OD ports, and on one of its horizontal 4 5/8" port. The two vertical buckets are designed to bring a window very close to the atoms for high numerical aperture imaging and optical access, and to bring magnetic coils close to the atoms to apply strong fields and gradients. The side bucket is designed solely for high numerical aperture imaging, its dimensions selected to accomodate a standard microscope objective (5X Mitutoyo Plan Apo NIR) at its infinite-conjugate working distance away from the atom location. The side bucket is so close to the center of the chamber that it begins to occlude the field of view of other viewports (see Figure 4-4), but this occlusion was deemed to be compatible with the use of those viewports as MOT / lattice ports.

The top bucket window flanges are equipped with tapped mounting holes, allowing magnetic coils and vertical axis optics to be mounted directly to the chamber. The side bucket is also equipped with tapped holes, for mounting to it a standard optics cage-rod system to hold a microscope objective deep in the bucket.

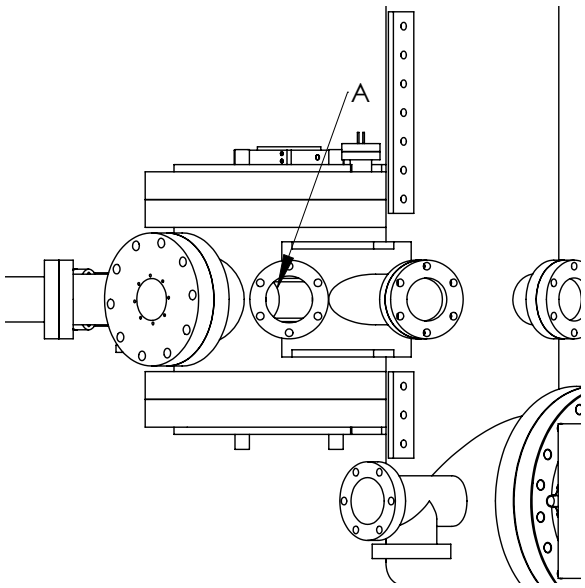

Figure 4-4: View into vacuum chamber through MOT/lattice viewport. The window field of view to opposing window is partially occluded by **A**, the side bucket window tube, which reaches deeply into chamber.

4.2.2 Standard windows

In addition to the 3 custom bucket windows, the main chamber has 10 other windows in the horizontal plane. Opposite the side bucket window is a large 4-5/8" window, used as a general purpose window to observe the MOT, and through which the atoms are illuminated for side bucket absorption imaging. Four 2-3/4" windows are set at 45° from the side axis. These windows are dual-purpose MOT / lattice windows, the optical access shared by translating a mirror as described in section 4.2.5. A 2-3/4" windows opposite the slower tube is used to apply slowing light. Since this window has a line-of-sight to the oven, it is heated to $\sim$ 180°C to protect it from alkali deposition. A second heated window is added immediately over the under-vacuum one, to shield the under-vacuum window from air currents and any source of potentially glass-stressing temperature gradients. Four windows are offset at 22.5° from the slower axis. These are intended as general purpose windows for optical plugs, dark spot repump beams, low resolution imaging, or any other uses that do not require a dedicated axis; the two windows on the far side from the slower are 2-3/4" in size, whereas the other two are 2-1/8" due to space constraints.

For all the relevant dimensions, consult the drawings in Appendix A.

4.2.3 Window materials, coatings, and purchase process

The 3 bucket windows were supplied by the UK Atomic Energy Agency (UKAEA) vacuum techniques group (contact: Simon.Hanks@ccfe.ac.uk), while the other windows were from ISI / MDC. Coatings were provided by American Photonics (contact: barry@americanphotonics.com). The windows flats were of fused silica, at the best flatness spec available from the suppliers ($\lambda/8$ for the 3 bucket windows, $\lambda/5$ for the others).

All the windows on the main chamber were given anti-reflection (AR) coatings. The side bucket window and its facing observation/illumination windows were given a single-V antireflection coating for 671nm – this is intended to be the highest performance Lithium imaging axis, and we wanted a coating that did not compromise in achieving the lowest possible reflectance. All the other windows were given a multi-wavelength coatings optimized for 532nm, 589nm, 671nm, and 1064nm.

Coating standard vacuum windows is a common technique for coating companies. The bucket window coating was a more elaborate multi-stage process. The top bucket windows would be too large to fit in a coating machine once fully fabricated, but the high temperatures required to create their glass-metal seals would be damaging to any coatings that are pre-applied to the glass flat. Therefore, the buckets were first partially constructed, bonding the window the a metal subassembly. This subassembly was send to the coating company to be AR coated, and then sent back to UKAEA to be welded to the bucket.

For the side bucket, the situation was more complicated. To achieve a uniform coating thickness, coatings are generally performed by having a planetary gear system move either the part or the coating source in a pseudo-random pattern. However, the smallest subassembly that the window could be pre-bonded to presented a large tube length compared to the size of the window, meaning that a substantial region of the window would have been partially shadowed from the coating source and would not receive a proper AR coating. This difficulty was overcome thanks to the cooperation

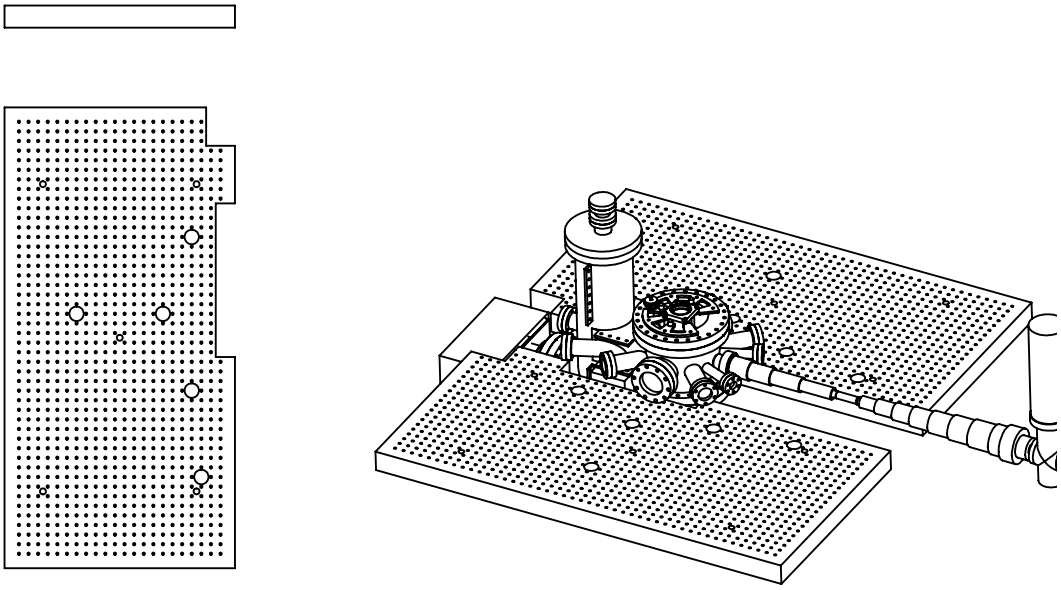

Figure 4-5: Custom breadboards nesting with vacuum chamber. Each board has 5 1.5 inch diameter beam holes, as well as 5 smaller mounting holes. Built by TMC (contact mckopt@aol.com).

of the coating engineer at American Photonics, who agreed to perform some coating test shots without using a planetary gear system, allowing them to characterize the deposition onto a stationary substrate well enough to apply a coating to the side bucket without the shadowing problem.

Reflectance graphs produced by American Photonics, for all the coatings described, are reproduced in Appendix C.

4.2.4 Breadboards

Custom breadboards were supplied by TMC (contact: MCKOPT@aol.com). The top and bottom skins were made from 304 Stainless Steel (a less magnetic alloy than the typical default), with a non-magnetic honeycomb core and sidewalls. The design depicted in Figure 4-5 (or with detailed dimensions in Appendix B) was based on careful consideration of how to optimize space and make the most of our viewports.

Cutouts along the perimeter allow the breadboards to nest close to the vacuum chamber. Circular cutouts (5 per board) are strategically located for passing beams from the breadboards' top surfaces to their undersides or to the main table below. In particular, cutouts near the 45-degree MOT / lattice ports allow us to feed MOT beams from below the breadboard and send them into the chamber with translatable mirrors (see section 4.2.5) which allow the windows the be shared between MOT and lattice beams. Having the bulky MOT telescopes tucked away frees up an enormous amount of valuable real estate on the breadboard's upper surface. Additional cutouts on the 22.5 degree axis allow for convenient delivery of the optical plug beam, and cutouts on the side imaging axis allow for reconfigurable imaging pathways which make use of both breadboard surfaces.

The breadboards and the chamber were mounted on 2"×4" cross-section extrusions from 80/20. The large hollows of these mounting posts were filled with lead shot. The 80/20 plus lead shot solution was found to provide a simultaneously stiffer and more vibration damping combination than off-the-shelf vibration isolation posts from Thorlabs (DP14).

4.2.5 MOT mirror translation

The pneumatic-translation-stages for the MOT beams are shown in Figure 4-6. They are constructed by modifying a standard translation stage (Newport 433), adding a pneumatic actuator from Bimba. This design has a few advantages over any commercially available automated translation solution. It is far more compact and inexpensive then servo-motorized translation stages with similar travel. Servo-positioning is not required – in the mirror's retracted position (with pneumatic actuator extended) we obviously do not care about its exact location, and in the engaged position the stage stops against a micrometer screw for reasonably repeatable positioning. In addition, the mirror and stage and aligned in such a way that the stage's movement is in the plane of the mirror, so the exact stop position does not affect the reflected MOT beam pointing. Testing this stage configuration using a camera over several thousand cycles revealed a beam pointing repeatability of less than 10μrad, which is certainly good

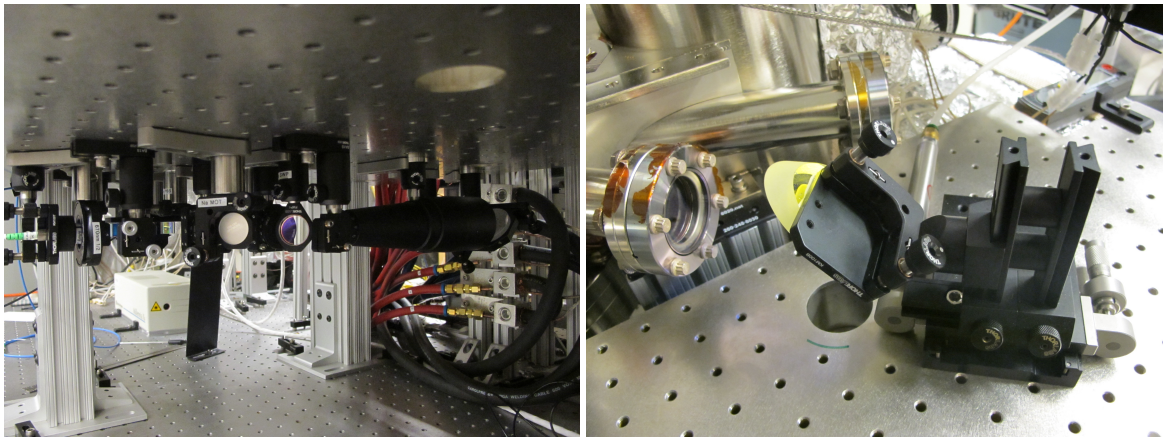

Figure 4-6: MOT mirror translation allows viewports to serve as both lattice and MOT viewports, without compromising either performance. **Left**: On the underside of the 2nd layer breadboards, MOT light for Na and Li are cleaned in polarization, combined on a dichroic beamsplitter, and then expanded in a telescope. Placing this seldom-adjusted set-up on the underside of the table frees up a substantial amount of space that would otherwise take up on the top of the breadboard. **Right**: After being expanded by the telescope, MOT light is fed up through 1.5" holes in the breadboard, to a translatable mirror. When the stage's pneumatic tube is depressurized the mirror redirects MOT light into the vacuum chamber. When pressurized, the stage moves the mirror out of the way, freeing up the viewport for use with lattice beams from the top of the breadboard.

enough for a MOT beam (compared with tested ∼1mrad repeatability from flipper mirror Newport 8892-K).

4.2.6 MOT beam distribution

Making a MOT requires illuminating the atomic cloud from several directions (generally 6, as in our experiment), often with additional repumping light frequencies present in one or all illumination beams. In our experiment, ^{6}Li is illuminated with 6 beams that each have roughly equal power in both MOT and repump frequencies, while ^{23}Na just receives 6 beams of MOT light, with the repumping provided by separate dark-spot repump beam.

In the early experiments, MOT light was prepared with the correct set of frequencies on laser tables, then fiber- (or even free-space-) coupled to the experiment table, where its power was split into 6 beams using waveplates and polarizing beamsplitters.

These beams were then distributed in free space to 6 MOT telescopes, and sent into the chamber. This tried-and-true technique certainly worked, but because of the long free-space-propagation paths was very prone to misalignment.

Modern experiments have mostly abandoned free-space-MOT distribution thanks to developments in fiberized systems to accomplish the same. Our experience with fiberized MOT splitters began when we replaced our old experiment's Li MOT system with an evanescent fiber coupler splitting system manufactured by Evanescent Optics Inc. (formerly known as Canadian Instrumentation and Research Ltd.). The splitter module, designed for 671nm light, has 2 input fibers (one for MOT, the other for repump light) and equally splits these powers into 6 output fibers. Changing to this splitter system significantly improved the alignment stability of our Li MOT – instead of fixing it on a near-daily basis, we needed to adjust the MOT alignment only every 6 months or so.

A few years later, based on this extremely positive experience, we tried to tackle the Na MOT distribution problem in the same way, with a new fiber splitter for 589nm light from the same supplier. However, after installing the system, we encountered problems with the splitter that were not exhibited in the Li 671nm version. Though the splitter is made using polarization maintaining (PM) fiber, and the splitting mechanism itself relies on a certain polarization, we observed significant polarization drifts in the splitter output on the ∼minute timescale. These drifts made achieving a stable Na MOT difficult. After discussion with the splitter supplier, it became evident that their fiber splitting technique is not yet well controlled at these shorter wavelengths.

In the new experiment, we have replaced the evanescent fiber splitter with a splitter unit from Schäfter+Kirchhoff, a miniaturized free-space splitter with fiber coupled inputs and outputs. While this system is more expensive than the evanescent wave system, its performance has made this a worthwhile investment. In the future, I recommend the evanescent system for wavelengths of ∼671nm or longer, and the Schäfter+Kirchhoff for shorter wavelengths.

4.3 Vacuum system

4.3.1 Background gas collisions, Fermi gases, and pressure goals

Atomic physics experiments have demanding vacuum requirements – for clouds that do not suffer from inelastic collisions or spontaneous emission heating due to resonant light, losses are only due to collisions between trapped atoms and background gas. Experiments with degenerate Fermi gases are even more sensitive to background gas collisions than Bose-Einstein condensates.

In a classical Boltzman distribution gas, if a randomly chosen trapped atom has a collision with a background gas atom and leaves the trap without any further collisions, the temperature of the remaining gas is unchanged. In a weakly interacting finite temperature BEC, losing a random atom causes a slight rise in the remaining gas temperature, roughly equivalent to adding kT of heat. For a Fermi degenerate gas, however, the atom will leave behind a hole in the sea, and when the remaining gas relaxes to fill this hole it release heat in the cloud on the order of the Fermi energy. Starting from a $T = 0$ Fermi gas, randomly removing 1% of the atoms, and then allowing the cloud to relax will result in a cloud temperature of $T \approx 0.01 T_F$ (where T_F is the Fermi degeneracy temperature). Estimates for the temperature required to observe Néel ordering are around $T/T_F \approx 0.06$ [47], so in a trapped cloud with a fairly long vacuum lifetime of 100s, the heating due to background gas collision losses would limit the lifetime of Néel temperatures to only a few seconds.

Our old apparatus had decent but not extraordinary vacuum relative to its peers. About once or twice per year, when ion gauge in the main chamber began to read a value above its minimum threshold of 9.7×10^{-11} Torr, we would fire our Titanium pump until the pressure dropped below the gauge's threshold. Thus a rough estimate for the pressure in the old machine would be in the high 10^{-11} Torr range. With the stringent vacuum requirements to see Néel ordering in mind, we set for ourselves the goal of improving the vacuum in our new experiment by roughly an order of magnitude

in the new machine, compared to the previous experiment. Since the construction of our old apparatus, new ion gauges such as the UHV-24p from Varian have become available capable of measuring much lower pressures down to 5×10^{-12} Torr. Reading from this newer model of gauge in our main chamber, after the chamber has been in operation for several months, we estimate an achieved pressure in the region of 1.6×10^{-11} Torr.

4.3.2 Evaporable getter coating

At the low pressures of experiments like ours, the pressure achieved in a vacuum chamber is simply set by the ratio between outgassing rate and pumping rate. One approach to achieve high pumping speeds in a chamber is to turn the whole chamber into a pump. Getter coatings can allow one to do just that, though standard getter coatings like that from a Titanium sublimation pump cannot be reactivated once they are exposed to air (new Ti needs to be deposited, and this is not practical in the main body of a chamber like ours with many viewports that must be kept deposition free). Facing a similar need, wanting to turn their large particle accelerator tubes into pumps, vacuum researches at CERN came up with a getter alloy of Titanium, Zirconium, and Vanadium that can be exposed to air and then reactivated by baking at a moderate temperature of ∼180°C [7, 12].

This getter coating is now becoming a common ingredient in newly built atomic physics experiments. Some groups have managed to collaborate with CERN or their technology licensee SAES to get their chambers coated. Others try to apply the coating themselves. We followed in the footsteps of the Zwierlein group's Fermi1 experiment, which attempted applying these coatings using thermal evaporation from Ti, Zr, and V wires. In order to better quantify deposition rates of the three elements as function of current, we built a test chamber incorporating a quartz crystal monitor to measure film deposition rate. Resistively heated Ti and V wires could be made to deposit at measurable (though slow) rates, but Zr, due to its very low vapor pressure right up to its very high melting point of $\approx$ 2128 K was impossible to evaporate thermally in a controllable fashion.

Indeed, thermal evaporation is not the preferred method for depositing this coating. At CERN, coatings are by magnetron sputtering in a rig with a complexity far beyond the scope that we could implement ourselves. Fortunately, the Ti-Zr-V coating is used at accelerator facilities in the US as well, and the very helpful vacuum scientists at Jefferson Lab who were willing to sputter coat our chamber for us as an experiment (Phil Adderley and Marcy Stutzman of Jefferson Lab). The main chamber was shipped to the Jefferson Labs facility in Newport News, VA, where it received a getter coating, and then was driven under vacuum in a rented minivan back to Cambridge, MA. It is difficult to quantitatively verify the performance of the coating, but our achievement of low pressures in the main chamber suggests that the getter coating is either acting as a pump, or at least acting as a suppressor of the normal outgassing from the steel chamber walls.

4.3.3 Supplier considerations

When building a complicated vacuum chamber, one is often at the mercy of part suppliers. As such, it seems worthwhile to pass along lore and wisdom that has bee accumulated about potential vacuum suppliers, to guide those who would build the next vacuum chamber. Given the number of components purchased from these suppliers, it was inevitable that certain components would have flaws, thus the judgement of a supplier's quality should come from how the supplier responded to and addressed flaws once discovered.

MDC is to be avoided whenever possible. Unfortunately, they have the largest catalogue of windows and standard conflat fittings. For simple parts like these, they are reasonably reliable. For valves they should be avoided at all costs – 2 of their gate valves failed almost immediately after first use, and 1 brand new angle valve failed out of the box. A far superior valve supplier is **VAT** – though their gate valves are pricier, they are of much higher quality, and their angle valves are both cheaper, better, and faster shipping than MDC's. Other MDC products, such as their high current electrical feedthroughs, are shoddy in quality. When pressed for service or support for defective parts, MDC's customer service was *reliably useless*. Their large

catalog also contains many parts that are not stocked, and many have lead times measured in months. It is typically impossible to be sure a given part is in stock without speaking to a customer service rep.

Sharon Vacuum made our custom main chamber, as well as some other custom components. Discussions with them were generally quite informative and helpful. Somewhat bizarrely, the slower tube of our vacuum chamber fell off the chamber in shipment to to Jefferson Lab. Thankfully, both Sharon Vacuum and the welders and Jefferson Lab were very responsive in preparing a new tube and getting it welded to the chamber.

Varian Inc (now a division of Agilent) was, overall, easy to work with. A turbopump purchased from them had issues early in its life cycle, and they replaced it with minimal hassle. **Duniway Stockroom** is a good source of basic hardware, such as gaskets, screws, plate nuts, blanks, and uncoated viewports, and keeps a large selection in stock and ready to ship quickly. **Kurt J. Lesker** was good for the evaporation sources that we experimented with when trying to thermally deposit our getter coating, as well as a source of bellows, insulating beads, and other assorted parts. However, a window of theirs, installed in our oven chamber, imploded after being heated while exposed to alkali, which caused several months of down time as it necessitated a full re-bake of the main chamber. This is one of the only known instances of window implosion in the hallway, an event freakishly unlikely, and it is not clear whether to judge this as a failure of Lesker or just a freak event.

4.4 Magnetic coils

4.5 Trap coil design, fields, wiring

The first BECs, at JILA and MIT, were produced in magnetic quadrupole traps. Quadrupole traps are simple to build, and simple to understand. A pair of coils run current in opposing directions, creating a point of zero field at the trap center and a field strength gradient in the radial and axial directions. However, when a

magnetically trapped atom (with its magnetic dipole moment tracking the local field) passes through the zero-field trap center, the atom's magnetic dipole alignment cannot adiabatically follow the field direction, resulting in Majorana losses as the atoms get flipped into a magnetically anti-trapped state. This problem was resolved by either moving the location of the zero field point to create a time-averaged trapping potential (in JILA experiments), or by "plugging" the hole in the trap using the dipole force of a tightly focused laser beam, blue detuned from the resonance of the atoms.

Further BEC studies at MIT abandoned the quadrupole trap in favor of Ioffe-Pritchard traps, in which a harmonic trap is created on top of a bias field. This eliminated the need for plugs, and allowed for clean studies of BECs released from harmonic magnetic traps, and became the standard magnetic trapping tool in MIT cold atom experiments.

In the newer generations of experiments (such as ours, or the new Zwierlein group Fermi1 experiment), the pendulum is now swinging back towards quadrupole traps. Particularly in experiments using strongly interacting fermions in a Feshbach resonance bias field, most of the interesting science is being done in optical dipole traps rather than in the magnetic trap, which is just a cloud preparation step. Thus, considerations of the clean harmonicity of the magnetic trap are not as relevant. The coil geometry in a quadrupole trap is much simpler, and all the trapping coils can serve as Feshbach bias coils as well, making the trap fully dual-purpose. And optically plugged quadrupole traps are demonstrably capable of fast production of large condensates [36] and Fermi gases.

The magnetic trap coil set design is depicted in Figure 4-7. The coil is constructed from fiberglass insulated square cross section copper tubing, allowing for water cooling by pumping water through the coils. The coil set is 10 layers at its widest, wound as 5 two-layer coils each with independent current and water breakouts to a bulkhead near the chamber. From the bulkhead, the coils are wired in series to combine them into an Outer and Inner segment, as shown.

Each coil layer has a different number of turns. This design gives a number of advantages over one with equal turns in each layer. The 5 layers have nearly the

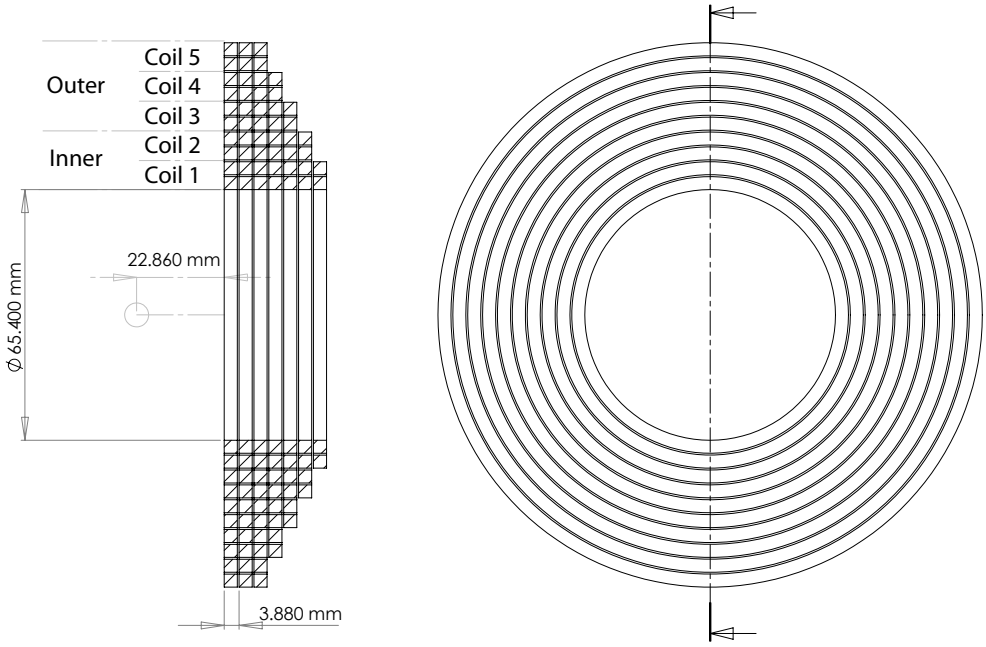

Figure 4-7: Design of magnetic trapping and bias field coil set. The coil set is electrically divided into an "Inner" and "Outer" segment. Each coil layer receives independent parallel water cooling. Bucket window design allows coils to be close to the atoms, ~ 23 mm. One of a matching pair of coils.

same wire length despite their different diameter (their lengths ranging from 2.5m to 3.3m), meaning their power consumption at a given current is roughly matched. This means water cooling for the layers is more uniform, with no layer having substantially higher heat load. Coil turns are on average closer to the atoms that a equal-turns-per-layer design, resulting in a higher magnetic gradient for the same total power. When running 500A in both coil sets, in counter-current configuration, simple simulations yield a magnetic field gradient of 1000 Gauss / cm in the axial direction, with a total power consumption of 17.4 kW (not including leads).

The same coils that are used for the magnetic trap can also be used to apply the strong bias fields required for making use of a Feshbach resonance. Once again, the unequal winding number of the layers is a boon. The Helmholtz condition for magnetic bias coils is fulfilled for a pair of coils when their diameters D and distance apart L satisfy $D = 2L$. In this configuration, a bias field applied with the coils has no curvature, $B''(r = 0, z = 0) = 0$. Coils closer together than Helmholtz have a negative curvature $B''/B < 0$ at the field center, and coils further than Helmholtz have a positive curvature $B''/B > 0$. In our coil design, the outer segment coils are close to the Helmholtz configuration. The inner segments are further from Helmholtz, giving more curvature for the same bias. This allows the outer coils to be used to apply a strong bias field, while a smaller current in the inner coils shims out their curvature without reducing the applied bias by much. A simulated bias field profile, with the field curvature at the center nulled by the inner segment coils, is depicted in Figure **??**.

Having only 4 independently addressable coils for all our magnetic trapping and Feshbach bias fields is a substantial simplification compared to our previous Ioffe-Pritchard trap. The coils are wired to capitalize on the simplicity, as sketched in Figure 4-9. For both inner and outer segments, the top and bottom coils are wired in series, driven by the same power supply. The polarity of the bottom coil in each pair is switched by an H-bridge relative to the top, to switch between the gradient (magnetic trap) and bias (Feshbach) configurations. The H-bridges are made using high-current mechanical relays (Tyco Kilovac LEV200A4NAF), rated to 500A.

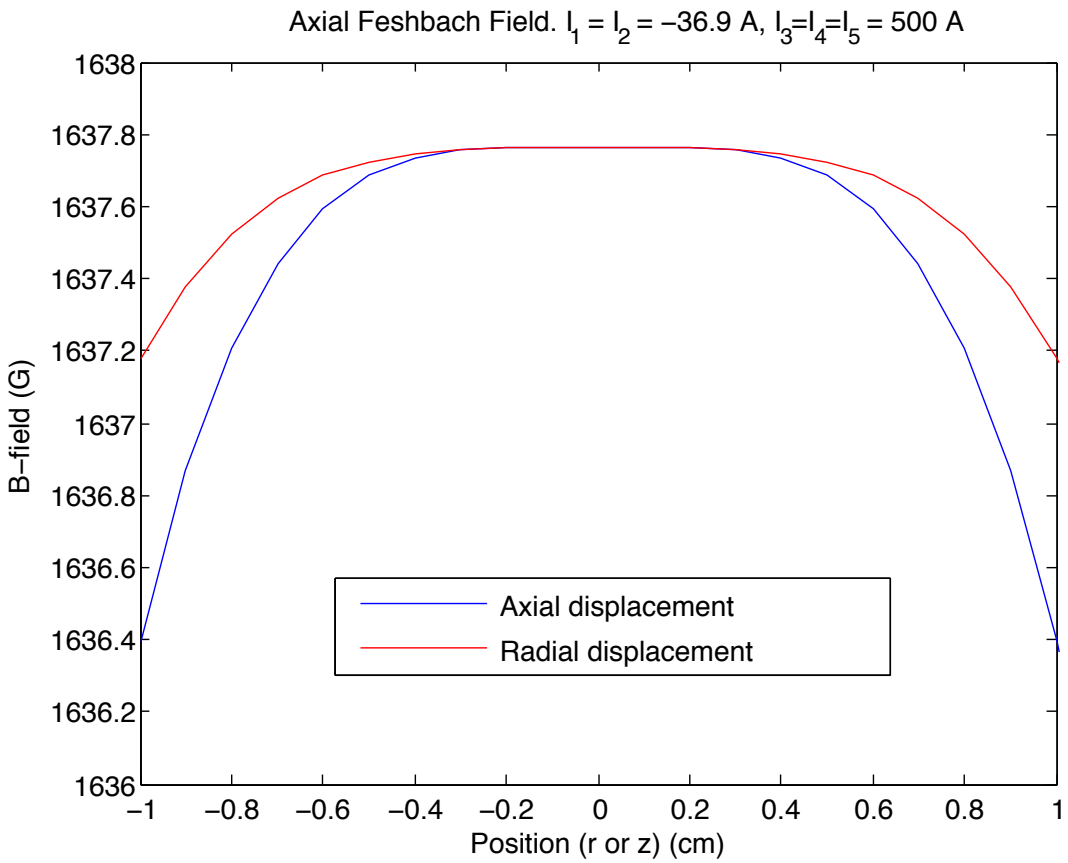

Figure 4-8: Magnetic bias field profile, when current is run in the same direction in matching coil sets.

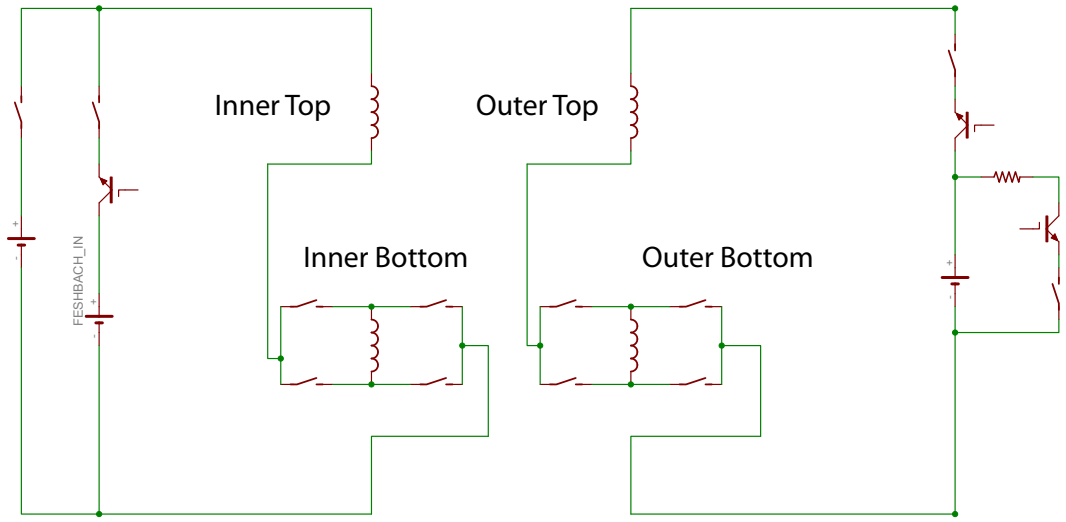

Figure 4-9: Wiring diagram for high current coils. For each segment (Inner or Outer), the Top and Botton coils are run by one power supply in series. Polarity of bottom coils can be flipped by a mechanical relay H-bridge. This wiring is dramatically simpler than in our previous Ioffe-Pritchard trap.

Though these are relatively slow to actuate compared to IGBTs, they bring the advantage of having no voltage drop during operation (eliminating the need for many water-cooled IGBTs), and providing true galvanic isolation when open (making circuit tracing and debugging substantially easier). The slow switching time is not expected to be capability-limiting – operations which require a very fast switch between a bias field and a gradient field can be accomplished by having the Outer set in one configuration while the Inner set is in the other configuration. Using the Inner coils with one power supply and Outer with another also ensures that current fluctuations during do not shake the center position of the magnetic trap.

4.5.1 Trap coil construction, mounting, connectorization, cooling

Following the standard lab practice, coils were wound using an old lathe. To keep the windings of the coil rigidly connected, it is important to apply liberal quantities of epoxy during the winding process, and allow the epoxy to harden overnight before

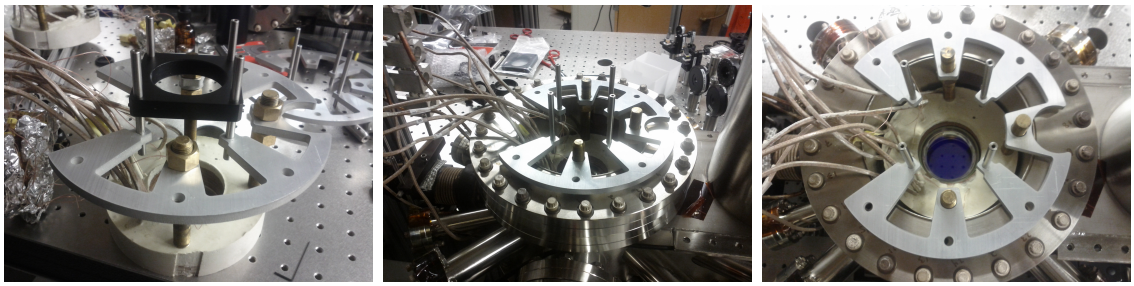

Figure 4-10: **Left** Epoxy-encased coil, with mounting rods, mounting plate, and a lens tube holder attached to mounting plate. **Center** Coil assembly inserted into top bucket. **Right** Top view of bucket, with viewport in center, and coil inserted (about to bolted in place, via visible bolt holes on mounting plate).

tension on the windings is released. After the coils were wound, they were potted in epoxy to enhance rigidity and to connect them to 3 threaded rods for mounting. It is crucial to use nonmagnetic epoxy; we followed the lab tradition of using Duralco NM 25 from Cotronics. Before using any particular batch of this epoxy, it is prudent to mix a small test sample and ensure that it mostly sets overnight – in our experience about 20% of batches do not set at all (or set very slowly, over the course of weeks), which would not be pleasant to discover after an extensive amount of coil winding.

A waterjet cut mounting plate is used to mount both the coils and a lens tube holder to the top and bottom ports of the main chamber. See Figure 4-10.

Each coil (top and bottom) has 10 electrical leads. These are broken out to a high-current manifold located close to the chamber. The distance to the breakout was made short in order to reduce the significant voltage drop that these leads can accumulate at target currents of 500A. The square cross-section leads are clamped to large aluminum lugs. These lugs are mounted to vertical aluminum 80/20 posts (see Figure 4-11). The limited amount of space in this high-value section of real estate necessitated the use of nylon spacers to insulate the lugs from the 80/20 posts and from the screws that hold them to the post (it is important that the lugs be mounted rigidly, so that they do not move when tightening and losing their high-current set-screw contacts, and thus mounting them using plastic screws was not appropriate). Care should be taken that the uninsulated sections of lead do not come in contact with either the aluminum posts or the mounting screws.

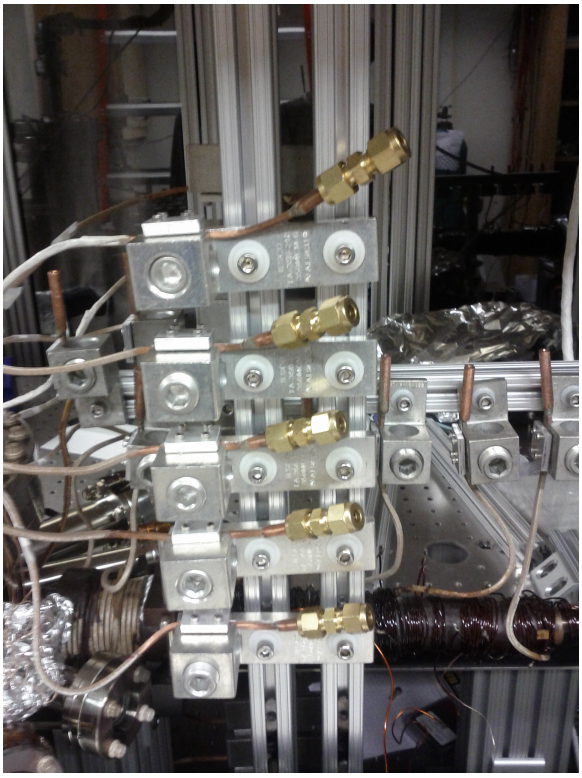

Figure 4-11: Coil electrical and water bulkhead. Coils leads are clamped to high current aluminum lugs, which are then connected to high current welding cable (not shown). Lugs are rigidly clamped to vertical 80/20 posts, using nylon spacers to isolate them from posts and mounting screws. This design is more compact than previous designs using plexiglass base for lugs, and allows for adjustment of lugs with access from one side only. Downstream of electrical connection, coil leads are adapted to round tubes (as described in Figure 4-12) and then to standard tube fittings for water cooling.

At the high current bulkhead, the coils are also connected to cooling water. The square cross-section tube of the coil must be sealed to a round cross-section tube in order to accomodate standard tube fittings. This is the classic square-peg round-hole problem that is encountered by every coil builder in the Ketterle group history, and every coil builder tries their own approach. At first, we experimented with reshaping the square tubing into a circle, either by forcing the tube through a round aperture, by manually sanding it into a circle, or by using a custom end-mill tool with a circular hole in it. While the last technique worked, it required a lot of finesse and was not very repeatable. In the end, we opted for the more traditional route of silver soldering the square tubes into circular tubes. This work was performed by the MIT central machine shop. In previous coils, there was a worry that the soldering process could cause solder to plug the small free-aperture of the coils. In response to this, the machine shop developed a new soldering technique which eliminated this worry. The technique worked flawlessly and is described in Figure 4-12.

Having safety interlocks that prevent running current in the coils when they are not water cooled is crucial in avoiding accidental destruction of the coils (which has occurred to experiments on the hallway on at least 2 occasions, always when safety interlocks were defeated or absent). In our experience, it is preferable to combine a water flow interlock with a coil temperature interlock. Selecting the correct water flow-switch is important – lower quality flow switches are prone to getting clogged, which invariably leads to those interlocks being defeated. The high quality 0804BN1 flowmeters from Proteus Industries proved itself very reliable in our old experiment, operating for over 10 years with minimal maintenance.

These flowmeters are, however, quite bulky. In addition, to protect the coils from clogging we elected to have particulate filters upstream of coil. And to improve the modularity and reparability of the plumbing, we wanted isolation valves on the supply and return side of each coil. These components, times 10 channels for the coils (plus some spare channels) add up to a lot of hardware, and it took some careful mechanical design to fit all of this in a confined space. This water manifold provides water cooling for all our coils, and fits under the optics table, rather than towering

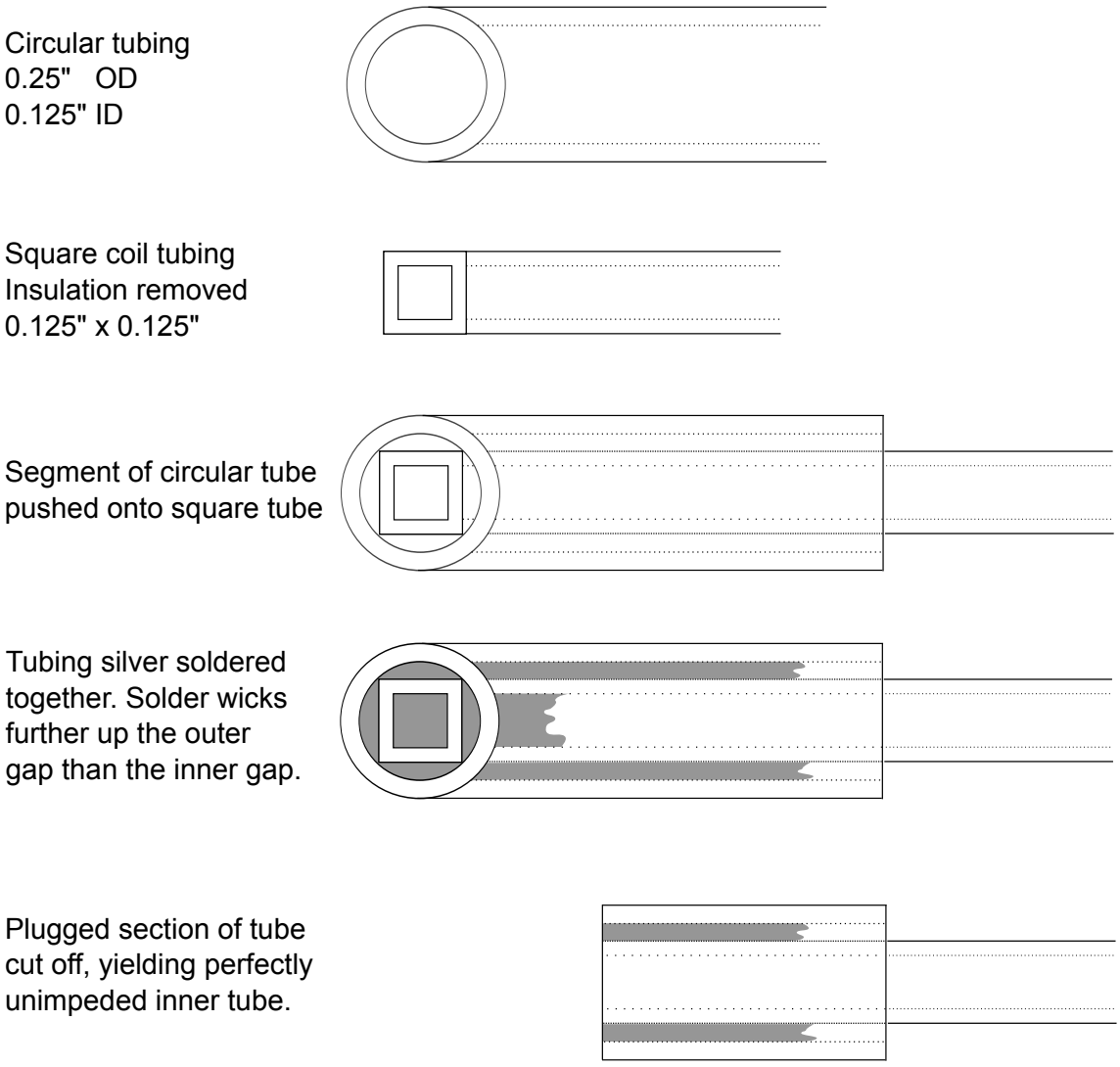

Figure 4-12: Improved tube soldering technique. Drawings not to scale.

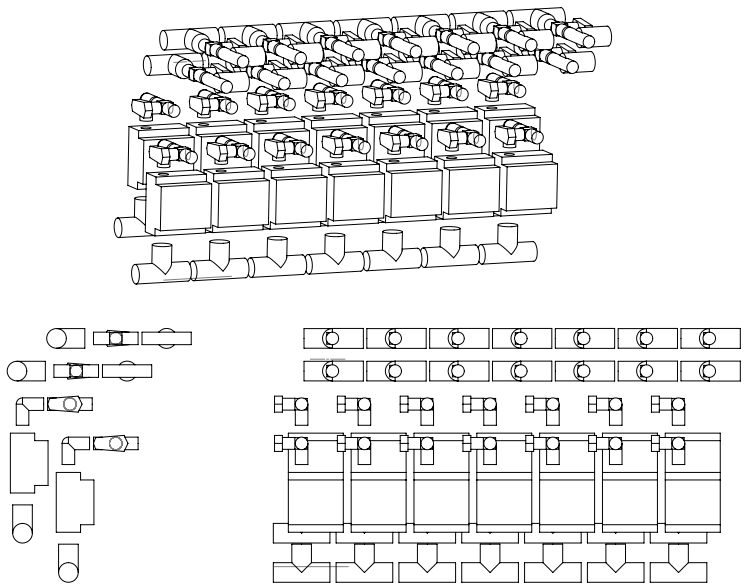

Figure 4-13: High pressure (200 psi) water distribution manifold. Some fittings and adapters excluded for clarity. Supply ports are the top two rows. Each supply port includes a valve and inline filter. Return ports are the bottom two rows. Each return port includes a valve and a Proteus flow meter. Flow meters are oriented so that their trip points can be adjusted from the front of the manifold. The ports are built on a backbone of 1/2" tube fitting Ts, adapted down to 1/4" tube fitting elbows, valves, and filters. The entire manifold fits underneath the experiment optics table. All parts except the flow meters are standard Swagelok parts. Not shown: tube to NPT adapters for flow meters, pressure gauge on supply and return manifold, hoses connecting the two supply and two return backbones, main supply valve, and main return valve.

over the machine, on the experiment table, as in our previous experiment. This has the added safety feature that leaks or work done on the water manifold does not risk getting water onto the experiment. The manifold design eventually used is depicted in Figure 4-13.

4.5.2 Safety Interlocks

Integrated into the coils are 10 thermocouples, sandwiched one per coil layer, to monitor coil temperatures. The thermocouples are scanned by a commercial thermocouple reader, with an alarm relay that opens when any coil rises above a set safety temperature. This alarm relay is wired in series with flow-ok relays of all of the used

flow meters. This safety signal is then multiplexed to a collection of relays which are connected to the safety interlock interrupts of all our high current power supplies. In this way, unless a user manually defeats the interlocks, our coils are protected from overheating – current cannot be run whenever water flow is insufficient or their temperature is too high.

4.5.3 Zeeman slower

Our Zeeman slower follows almost exactly the design laid out by [13]. In a dual-species experiment such as ours, the required length of the slower is set by the length required to slow the heavier species (^{23}Na in our case). This design is a spin-flip slower with a decreasing-field section starting just after the oven, a zero-field bellows section to help with alignment, and an increasing field section leading up to the chamber body. A side benefit of the long slower is a large differential pumping rate between the main chamber and the higher pressure intermediate and oven chambers.

A key technique invented in [13] is a major reduction in the inner diameter of the Zeeman slower coils, made possible by using "split ring" miniflange bolt rings that can be assembled in place after the slower solenoid is slid over the vacuum tube. In [13] and its descendants, these rings were simply normal rotatable bolt rings that had been cut in half in such a way that each half had 3 full bolt holes. However, because of their non-uniform compression of the gasket, these split rings have occasionally been responsible for leaks during vacuum assembly. We developed a superior interlocking split ring, using a horseshoe design in which each ring segment contains 4 bolt holes (see Figure 4-14). These parts were inexpensively machined for us by Sharon Vacuum. When assembled in place over the tube, this interlocking ring design acts like a solid bolt ring, and eliminated sealing difficulties.

4.6 In-Vacuum Antenna

Like previous experiments, the vacuum chamber is equipped with an in-vacuum antenna. This consists of a single loop of wire, normal to the slower axis, held in place

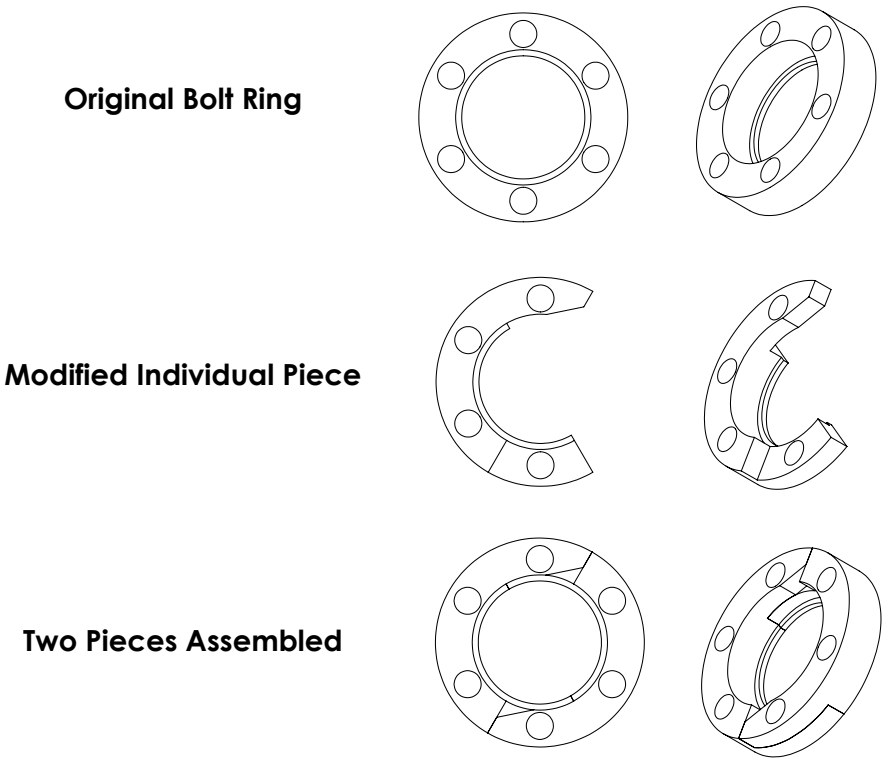

Figure 4-14: Concept for interlocking split ring design. See Figure B-3 in Appendix B for detailed dimensioned drawing.

by its own elasticity sandwiched between the top and bottom buckets, in such a way that it does not block the line of sight of any viewports. The outgassing rate of kapton insulation is inconsistently reported in the literature, varying over several orders of magnitude; the upper estimates would have given outgassing from just the small loop of wire that would have been the dominant gas load in the chamber. Thus, we avoided kapton insulation – the antenna is constructed from UHV grade uninsulated oxygen free copper wire. Ceramic insulation beads are applied to the wire at strategic locations to insulate it from the walls of the vacuum chamber.

The antenna is mainly intended for driving $|1\rangle \rightarrow |2\rangle$ transitions in Lithium in the presence of a bias field. These magnetic dipole RF transitions, in the 80 MHz range, are useful in RF spectroscopy studies and in preparing and manipulating spin mixtures. In some experiments it is important to apply these pulses quickly, thus having a high Rabi frequency for the drive, and thus a close proximity between antenna and atoms, is desired. The matrix element for these transitions in a vertical bias field is also maximized by having the antenna apply a horizontal oscillating magnetic field.

Thinking of the in-vacuum coil as an antenna can be misleading – it is more appropriate to think of it as a small coil with which we apply oscillating magnetic fields. At the frequency we plan to use it for, atoms are in the coil's near field, and impedance matching the "antenna" to achieve high radiative efficiency is irrelevant. Instead, what is desired is to apply as large a magnetic field as possible. The number of turns of the antenna was limited to one – with just one turn the self inductance of the coil already gives an imaginary impedance of approximately 50 Ω at 80 MHz, and increasing the number of turns would cause it to present an even higher impedance to its driving amplifier.

Space constraints inside the chamber led us to chose a 2-wire electrical feedthrough (Lesker EFT0023032) to connect to the antenna. However, this feedthrough turned out to be very fragile, with both out-of-vacuum leads breaking off at some point during the chamber wrapping or baking process. Wires have been reconnected to the feedthrough using conductive epoxy, but the connection is extremely fragile. Thus,

it is strongly recommended not to apply any stress to the antenna wires. Future experiments that use this feedthrough should take positive measures to protect its out-of-vacuum leads from any strain.

4.7 Environmental control

Temperature fluctuations are the bane of an atomic physics experimentalist's existence, and nothing is more frustrating than spending hours aligning optics because the ambient temperature changed. The old BEC2 experiment suffered terribly from this problem, and for many experiments the only practical hours of data taking were in the middle of the night, after several hours of warming up the machine, when temperatures were more stable. Addressing this issue was a major goal of the rebuilding project.

The large size of the BEC2 lab, with its many heterogenous and fluctuating heat sources and large windows, makes it very difficult to control the lab's average temperature, let alone eliminate significant temperature gradients within the room. Depending on the weather, turning on all of the power supplies, lasers, and other sources of heat in the lab routinely results in a temperature jump in parts of the lab of 5°C over the course of 2 to 4 hours. Tuning the feedback parameters of the lab's build-in air conditioning system was unable to address this, due to the slow response of the room temperature to the AC. Exacerbating the matter are the fluctuations in MIT-supplied chilled water temperature – in the summer the chilled water is kept at ~ 5°C while in the winter it averages ~ 11°C (since general cooling demands are much lower), meaning that the capacity of the air conditioning system is reduced by as much as 40%. On top of the annual cycle, the water temperature also fluctuates by ~ 1°C throughout the day due to changing loads and cost saving adjustments by MIT facilities.

To address the problem, the approach taken for stabilizing the experiment temperature was to enclose the experiment in a much smaller dedicated air volume, with its own dedicated environmental control, de-coupling it to a large degree from the

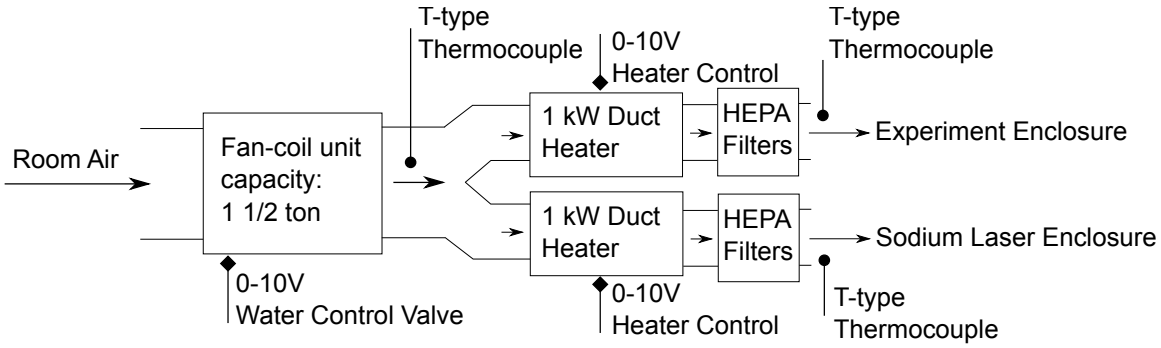

Figure 4-15: Enclosure air conditioning system schematic. Cooling capacity of the fan-coil unit is nominally 1 1/2 tons. The ton as a unit of refrigeration is fascinatingly archaic unit that is still standard; 1 ton of cooling is equivalent to the cooling provided by the melting of a daily delivery of 1 short ton of ice (so 1 ton = 3.52 kW). System installed by Guy Fossiano guyf@ahcmechanical.com.

problems of the larger room temperature. During the renovations to install this system, it was decided to extend this environment control to the Sodium laser table in the same room as well, with its own enclosure.

A schematic of the enclosure air conditioning system is presented in Figure 4-15. Air from the room is drawn into a dedicated fan-coil unit mounted in the lab ceiling. The output of this unit is fed to two ducted 1kW electric heaters, and then to HEPA filters feeding the two enclosures. Three simultaneous feedback loops, provided by a Stanford Research PTC10, are used to stabilize temperature. First, the water control valve of the fan-coil unit is used to feedback on the temperature directly after, servoing it to 20°C. Next, the heater controls for each enclosure servo the temperature directly after the corresponding HEPA to 22°C. The response time of the fan-coil unit is 20 minutes, while the heaters are closer to 1 or 2 minutes. This cascading air handling combination allows for much tighter temperature control at the enclosure than could be accomplished with just fan-coil units. With this system we find that the the output temperature of the HEPAs are easily stabilized to better than .1°C over the long term, with occasional minute-long .5°C bumps caused by the water control valve moving between discrete positions (these temperature bumps at the HEPA output are not expected to have any measurable impact on the table temperature).

Building codes for laboratories require that the air in the room has some fresh air

exchange. This is accomplished by "makeup air conditioning" ducts with supply a small but steady flow of external air to the room, and room exhaust ducts which suck stale air out. The effective AC capacity of our lab could be improved by exhausting air from the hottest parts of the room. To this end, during the AC renovations we had a accessible duct for exhaust air installed. In future, if AC capacity in the room needs to be increased, this access duct can be connected by a flexible extension duct to concentrated heat sources in the lab, most prominently the Millenia laser controller and chiller.

Something as deceptively simple as an enclosure for an experimental table actually requires and demands careful attention to get right, and getting it wrong can easily defeat the enclosure's entire purpose. The fate of the removable hanging curtain enclosures around our laser tables served as an object lesson – the curtains were frequently left un-hung, or lying on the ground, were frequently in the way when trying to work, and were always a chore to remove and replace. This inconvenience lead to their "temporary" removal from the Lithium laser table, a removal later made permanent.

We needed an enclosure that when closed, provided a strong air separation from the room, when opened provided nearly unobstructed access for working on the apparatus, was rigid enough to stand or lean on, and could be easily and quickly opened and closed hundreds of times per day. These requirements were eventually met by using a custom design, using components from 80/20, and based on bifold sliding doors mechanisms. The design is described in sufficient sufficient to duplicate in Appendix D.

4.8 Solid state sodium laser

Experiments with large Sodium condensates, such as ours, require at least $\sim$1.5 W of light at 589 nm, locked to the D2 line and with a linewidth of $\sim$1 MHz or better. Historically, this was achieved by using tunable dye lasers with Rhodamine 6G dye. However, as anyone who has worked with them knows, dye lasers can be fussy and

messy, and our aging Coherent 899 lasers was a major source of experiment downtime. Advances in solid state laser technology have made a few alternatives available, and several of them were pursued to find a replacement for our dye laser.

Our initial line of development was to clone a system developed at ENS [56] based on sum-frequency generation. Both 1064 nm and 1319 nm light are readily achievable lines of Nd:YAG lasers, a favorable conspiracy of nature because these two frequencies sum to 589 nm. The ENS system used two non-planar ring oscillator Innolight master lasers, outputting 1.1 W @ 1064 nm and 500 mW @ 1319 nm. Their nonlinear sum-frequency generating element was a periodically-poled KTP crystal. A doubly-resonant bowtie cavity was used to cycle both 1064 and 1319 light through the crystal many times, achieving very high conversion efficiency and resulting in 800 mW of 589 nm light.

Our clone system was to be a higher power version of the same system, using the same crystal and cavity design, but with higher pump powers (2W @ 1064 nm, 800mW @ 1319 nm) to achieve output powers in the range needed for our larger sodium clouds. Unfortunately, when scaling up to higher powers, we encountered numerous roadblocks. With the originally tested crystals (supplied by KTH), thermal effects at the higher powers caused major complications in locking the doubly resonant cavity. Specifically, when 1064 was coupled into the cavity, this would cause localized heating and index change in the crystal, which would push the cavity off resonance (evidence for this was highly asymmetric cavity transmission traces, and an inability to lock the cavity). Crystals from other suppliers (Raicol) suffered less from this problem, but instead exhibited nonlinear absorption of 1064nm which also prevented cavity enhancement. Crystals in a different material were also tried (PPSLT, from HC Photonics) but these had too low a conversion efficiency. In the end, after many dead ends, we abandoned this high power SFG project. In the process of trying to lock a doubly resonant cavity using a complex mixture of feedback signals (as described in [56]), a feature-rich FPGA-based laser lock / signal processing package was developed, which may may still be useful, and is provided online at [43].

Ultimately, a separate turnkey yellow laser solution became available from MPB

Photonics. The scheme was made possible by advances in Raman amplifiers, allowing these amplifiers to reach high powers of 1178nm light, which when frequency doubled even with a relatively low efficiency can produce ∼1.5 W or more at 589 nm. Our current yellow laser system uses a Thorlabs 1178 single mode diode maser laser, fiber coupled into an 1178 raman amplifier from MPB, which is fed directly into an MPB-supplied doubling crystal. In our experience, the system is substantially less hassle than the old dye laser. However, being a beta product, it does still suffer from relatively frequent component breakdowns (on average one breakdown every 4 to 6 months). Fortunately, MPB has been very responsive in repairing the units they have sold us, and we are confident that they will improve the reliability as the product matures.

4.9 The Future

The transformation from conception to construction of the new machine took substantially longer than initially estimated. In part this was due to our desire to finish up ongoing experiments on the old apparatus, and in part because of unexpected slow lab renovations, and unexpected problems such as the aforementioned window implosion. As of this writing, the next generation of BEC2 grad students is bringing the new apparatus fully online, so far having achieved magnetic trapping of Sodium atoms and seen the first signs of effective RF evaporation.

Designing the new experiment, obsessing over hundreds of details, and trying to get everything just right, has been a labor of love, a mixture of great frustrations and joys. I hope the experiment proves to be as reliable and versatile as it was envisioned, and that it can be a platform on which the next generations can do amazing science.

Chapter 5

Outlook and Conclusions

> My friend asked me if I wanted a frozen banana, I said "No, but I want a regular banana later, so... yeah".
>
> Mitch Hedberg

This chapter will briefly discuss potential directions for the new experiment in preparing cold lattice samples.

5.1 Future of cold atoms in lattices

5.1.1 Cooling atoms in the lattice

Preparing fermionic Mott insulators in optical lattices is now a standard process in many labs, and is expected to be readily achievable in our new apparatus. Reaching the next level of ordering, a Néel phase, will require further reduction in temperature or entropy. A simple estimate of entropy at the onset of antiferromagnetism is ln(2) per particle, which is the entropy of a Mott insulator with no spin correlations at all (in a simple 1-band single occupancy picture), since each site has two possible states (spin $\uparrow$ or $\downarrow$).

At temperature T, a system with a gap E between a manifold of ground and

excited states of $E >> kT$ will carry much less entropy than a system with a similar number of total states spread continuously in energy. This is simply because entropy $S = -k \sum_i p_i \ln(p_i)$ goes to zero if all states are either surely occupied or surely unoccupied $p_i \in \{0, 1\}$, which is much closer to the case in the gapped system than the continuous one.

Thinking in terms of entropy has lead to creative proposals for cooling atoms in a lattice atoms that focus on squeezing out the entropy, by transferring entropy from gapped degrees of freedom to continuous ones (which carry a larger amount of entropy at a given energy). For instance, in [37] it is proposed to trap a band insulator of fermions in a lattice, with a background heat reservoir BEC that doesn't feel that lattice soaking up entropy from the fermions. The overall confining potential would then be ramped down to allow the fermionic cloud to expand into a half-filled lattice, with hopefully low enough entropy for Néel ordering. It is not clear how experimentally realizable this proposal is – for Sodium-Lithium mixtures with a 1064nm lattice, the low mass of Lithium means that Sodium will feel the lattice much more strongly than Lithium. Other entropy schemes for bosons have been experimentally realized, such as using spin entropy in a bosonic Mott insulator as a thermometer [80], or as a refrigerator for kinetic degrees of freedom in a demagnetization cooling scheme [52].

5.1.2 Being cold already

One line of approach toward Néel ordering could be to prepare a large band-insulator sample with unity filling, and then adiabatically halve the lattice spacing along one dimension [51]. This can be accomplished with 532nm lattice beams phase stable to 1064 lattices, produced by frequency doubling. If the entropy of the band insulator can be made low enough, and the lattice ramp made adiabatic, a very low entropy half filled system would result.

Some simple calculations are presented here which may be of use in such a scheme. A starting point will be 3D band insulator samples that are as large and low-entropy as possible. Having tightly focused lattice beams means that a deep lattice can be achieved with low laser power, but also leads to a strong compression due to the

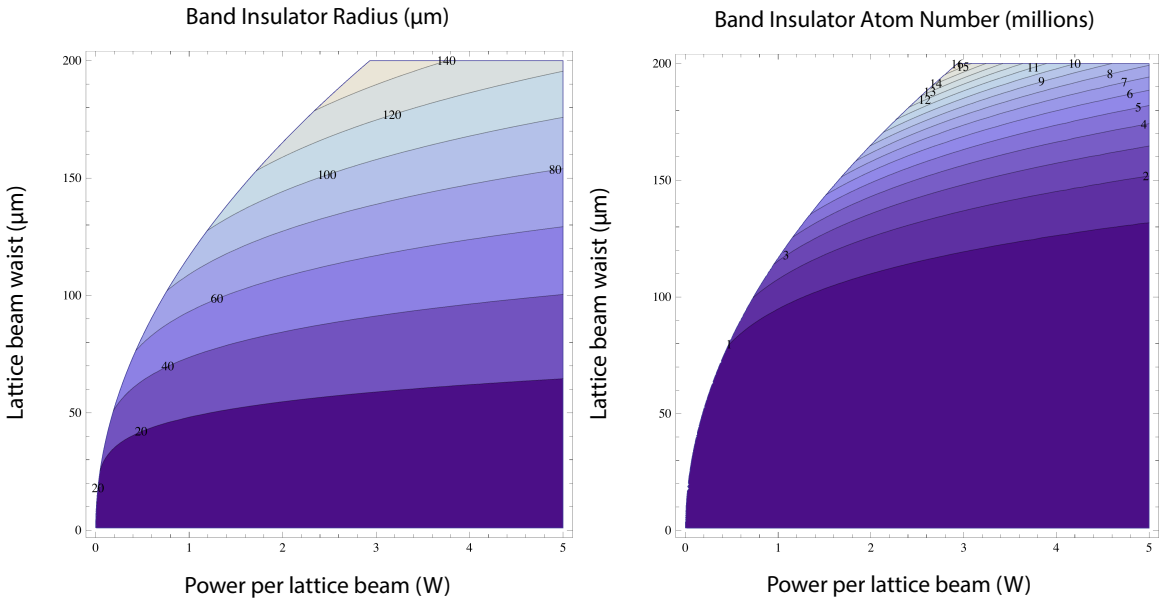

Figure 5-1: Size and atom number of the largest possible ^{6}Li band insulator as a function of lattice beam parameters. The simulations assume a 3D lattice made of 3 retroreflected 1064 nm lattice beams, each with the same beam waist and beam power. The excluded white area of the plots are the region for which there is no true band insulator; for which at the center of the cloud, the lattice depth is less than or equal to $8E_r$ where $E_r = \hbar^2 k_L^2/(2m)$ is the recoil energy for lattice beams $k_L = 2\pi/\lambda$, $\lambda = 1064$ nm.

lattice beams which limits the size of a band insulator that can be filled before the confinement promotes atoms in the center of the cloud to the second band. The tradeoff between power and beam waist, and the optimum band insulator size that can be achieved for a given lattice, is presented in Figure 5-1. The source code for this simulation is reproduced in Appendix I.

5.2 Conclusion

Quantum simulation of condensed matter systems with ultracold atomic gases remains one of the most exciting avenues of atomic physics. While some results have already been achieved, especially in bulk systems in the BEC-BCS crossover, most of the exciting work with lattice systems still lies ahead. Catching up with and then surpassing theory will be a major challenge in these experiments, but offers huge potential payoff in the insight it could deliver about condensed matter systems of

profound real-world relevance.

I hope the work in this thesis proves to be one small step towards those goals.

Appendix A

Mechanical drawings of main chamber

This appendix contains a fully detailed drawing of the custom steel chamber for the new machine, as sent to Sharon Vacuum for production.

Main Chamber
Overview and Coordinate Reference

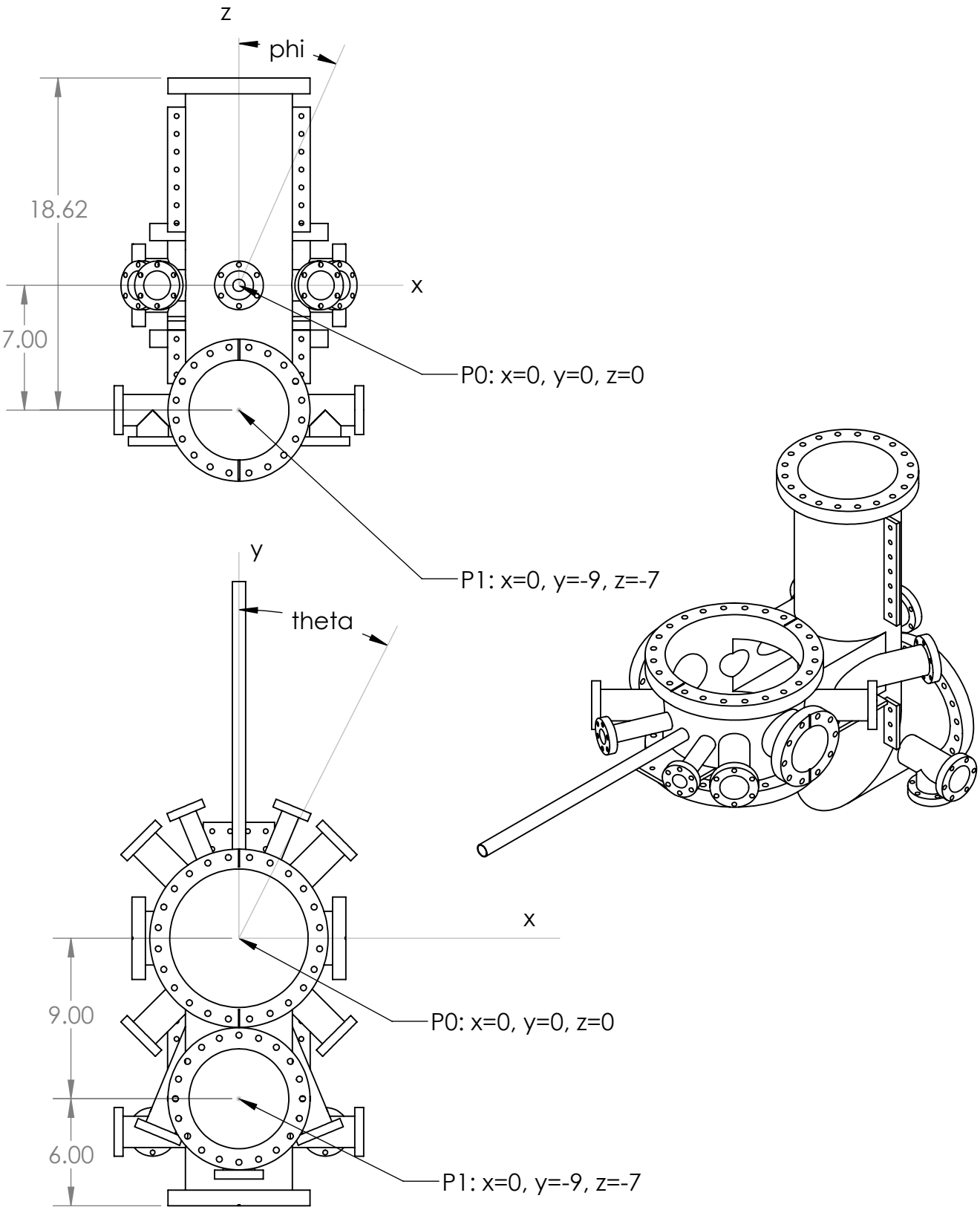

Main Chamber
Conflat Ports

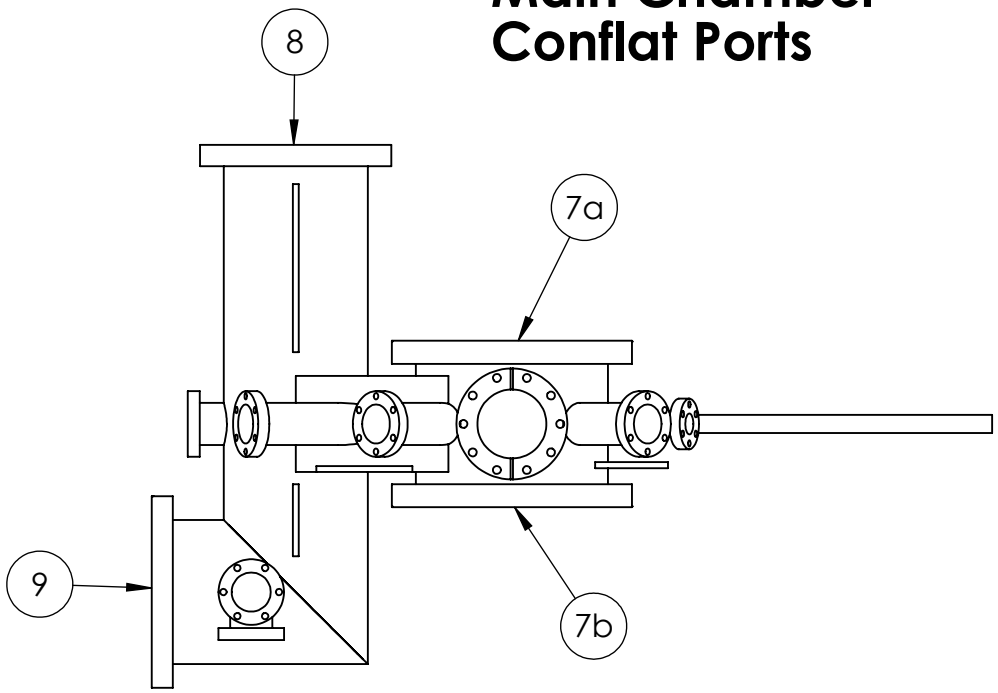

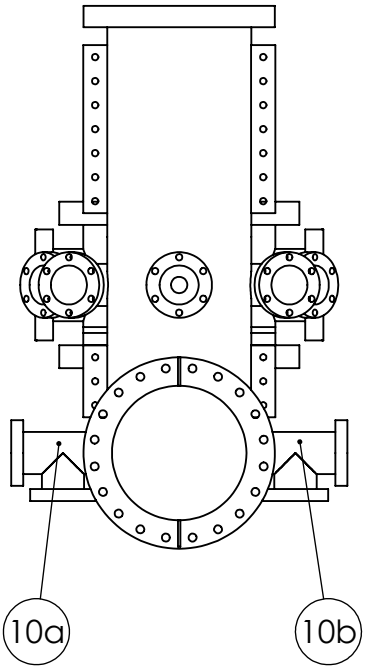

Port Location / Information Table						
Port #	Flange OD	Focal Point	Flange Distance (inches)	theta (deg)	phi (deg)	Special notes
1	1-1/3	P0	20	0	90	Tube and flange knife edge only! Omit Bolt ring. Instead, please supply 2 bolt rings cut in half such that all bolt holes are intact.
2	2-1/8	P0	8	a: -22.5 b: 22.5	90	
3	2-3/4	P0	8	a: -45 b: 45 c: -135 d: 135	90	
4	4-5/8	P0	6	a: -90 b: 90	90	Rotatable flange
5	2-3/4	P0	12	a: 157.5 b: -157.5 (facing ports 2a, 2b)	90	
6	2-3/4	P0	13.5	180	90	
7	10	P0	3.47	n/a	a:0 b: 180	Sniffer port aligned with y axis

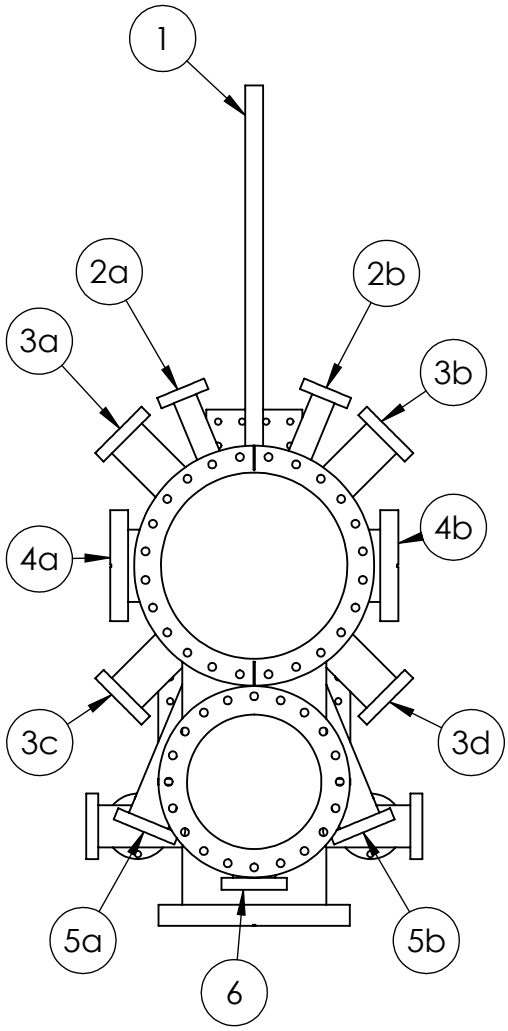

Table continues on next page...

Main Chamber Conflat Ports ...Continued

Port #	Flange OD	Focal Point	Flange Distance (inches)	theta (deg)	phi (deg)	Special notes
8	8	P1	18.62	n/a	0	
9	8	P1	6	180	90	Sniffer port aligned with z axis
10	2-3/4					a and b should be 2-3/4 conflat T junctions, somewhere convenient on the centerline of the horizontal tube for port 9. Exact location is not important.

Main Chamber
Mounting plates & mounting holes

34 mounting holes total

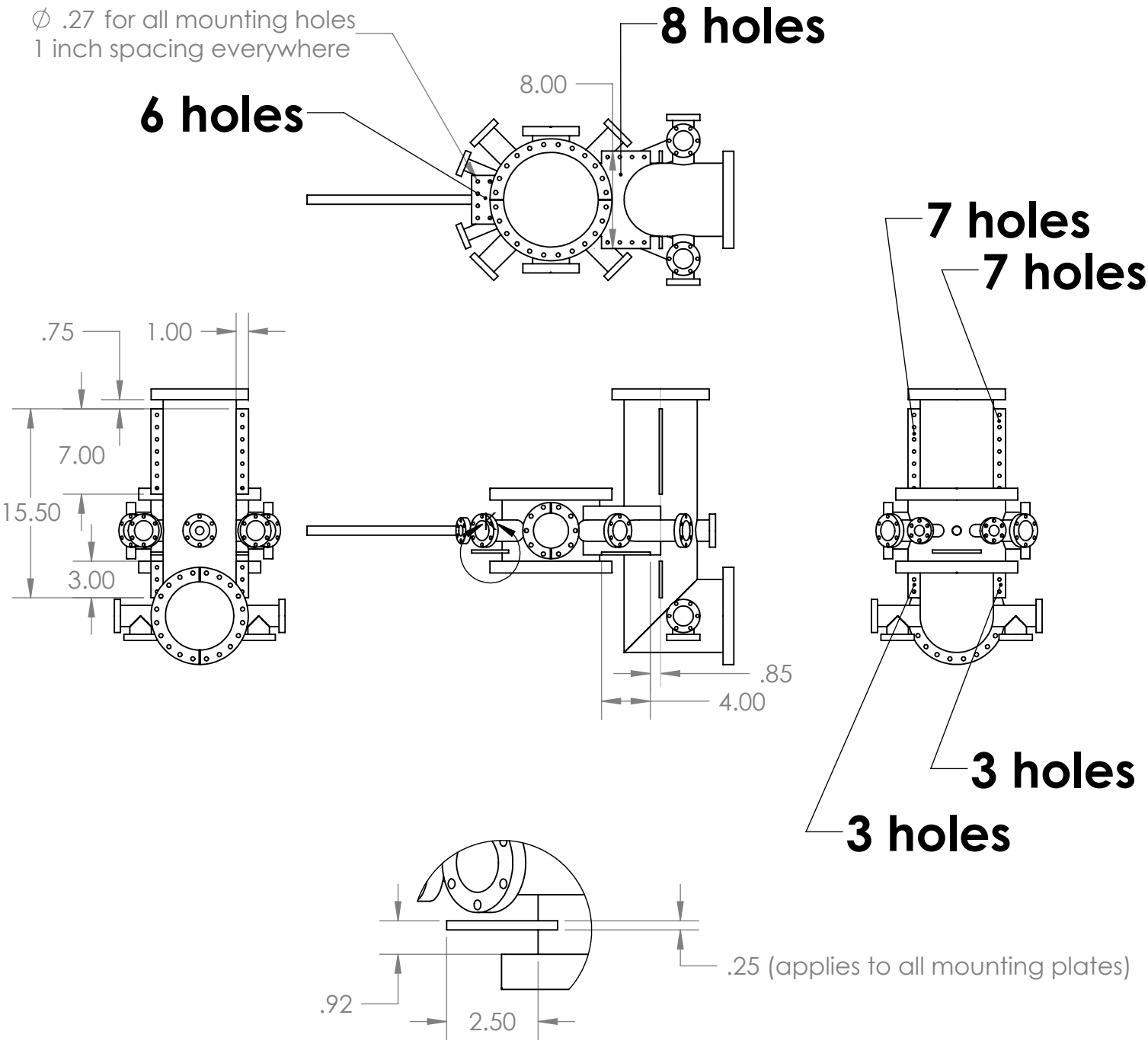

DETAIL K
SCALE 1 : 4

Main Chamber
Section Views

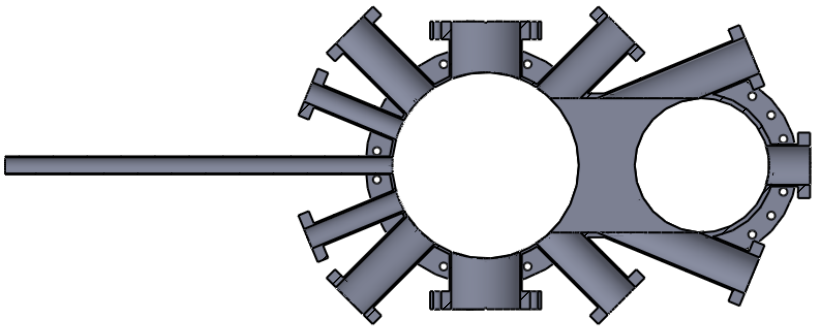

SECTION D-D
SCALE 1 : 8

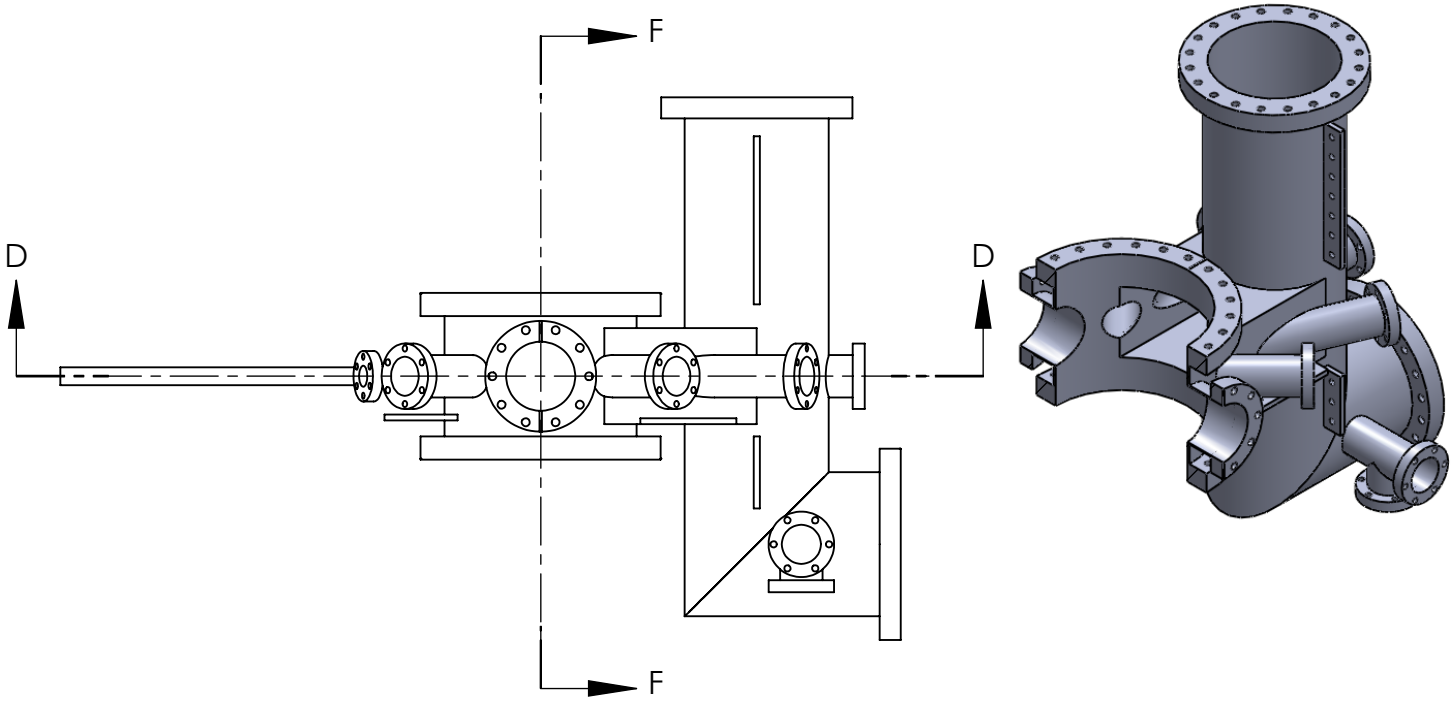

SECTION F-F
SCALE 1 : 8

Main Chamber
Section Views
...Continued

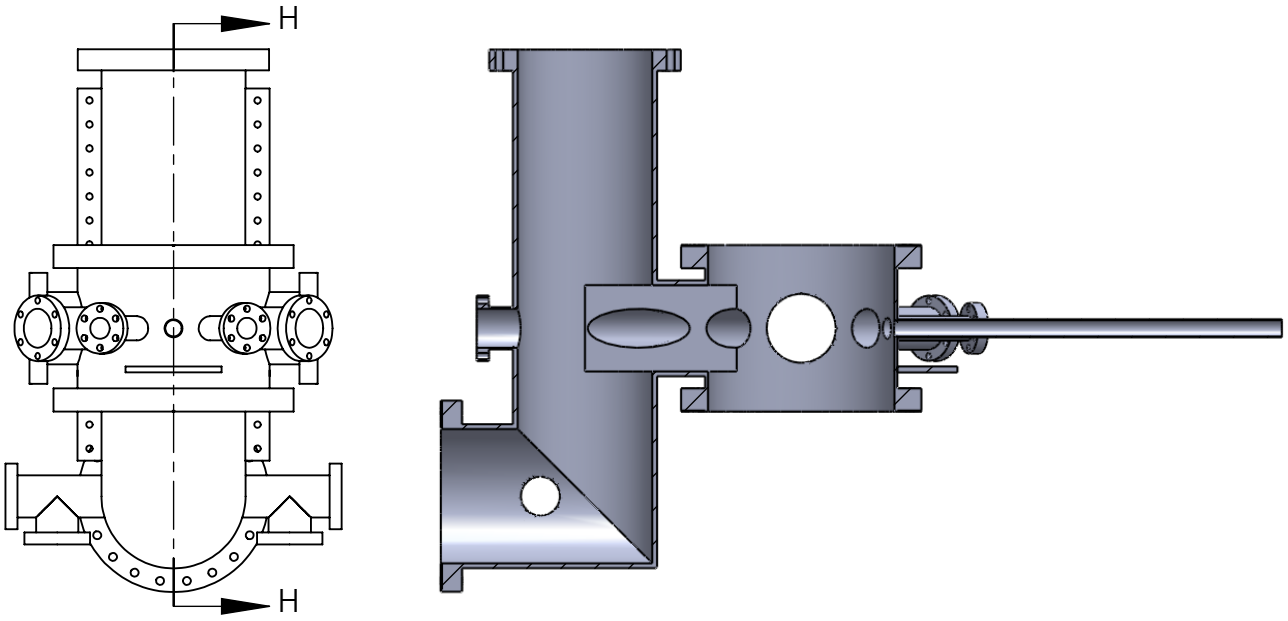

SECTION H-H
SCALE 1 : 8

Appendix B

Mechanical drawings of other custom components

This appendix contains various dimensioned mechanical drawings, suitable for sending to parts suppliers if parts are to be duplicated. The buckets depicted in Figures

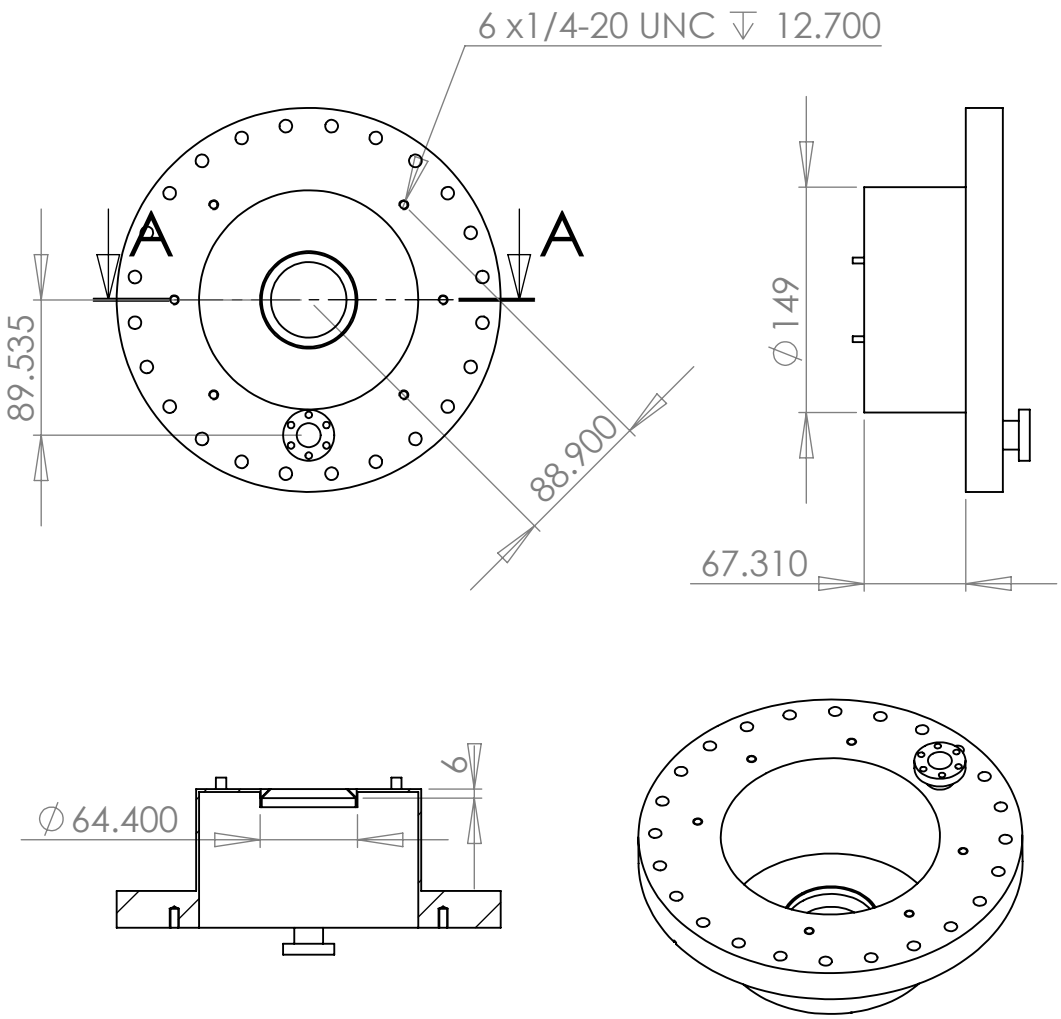

Figure B-1: Mechanical drawing of top and bottom reentrant bucket window (the depicted miniflange UHV port, used for in-vacuum antenna RF feedthrough, is excluded on one of the two buckets). Built by UKAEA (contact Simon.Hanks@ccfe.ac.uk). Dimensions are mm.

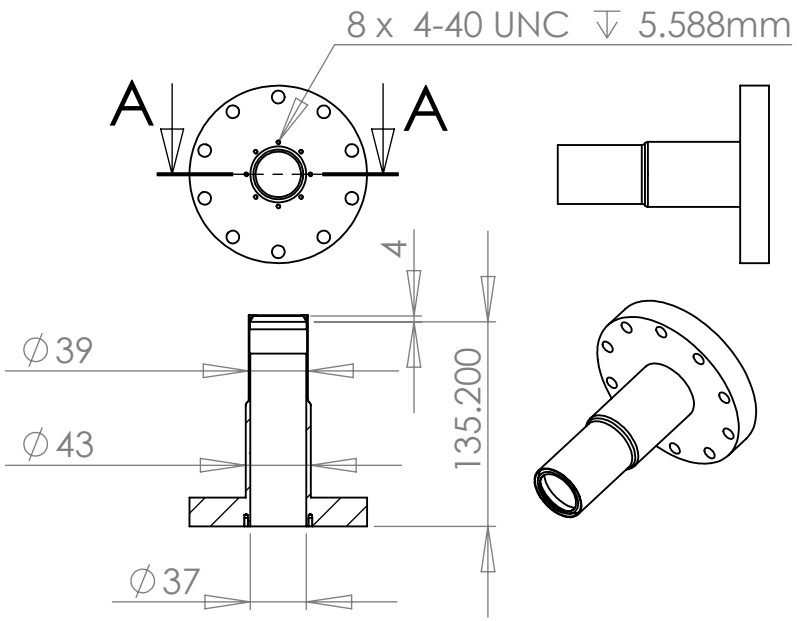

Figure B-2: Mechanical drawing of side reentrant bucket window. Built by UKAEA (contact Simon.Hanks@ccfe.ac.uk). Dimensions are mm.

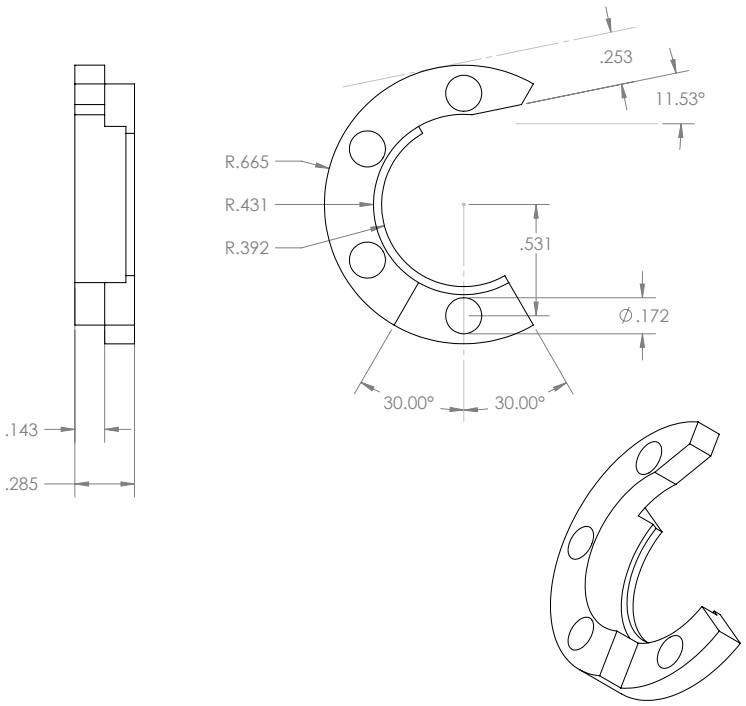

Figure B-3: Mechanical drawing of interlocking split ring design. Any unspecified dimensions are based on the starting part, a standard miniflange rotatable bolt holding ring. Built by Sharon Vacuum (contact larry@sharonvacuum.com). Dimensions are inches.

PART A
Quantity 2

Modified double-sided
2.75 inch flange.

4 tapped blind holes
1 through hole
1 45 degree taper of specified depth

Starting part MDC part number 140007

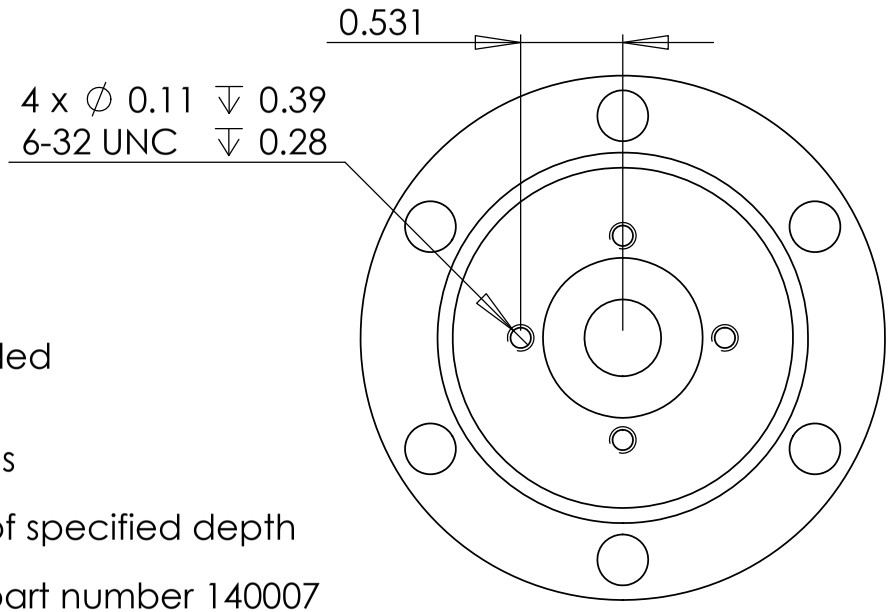

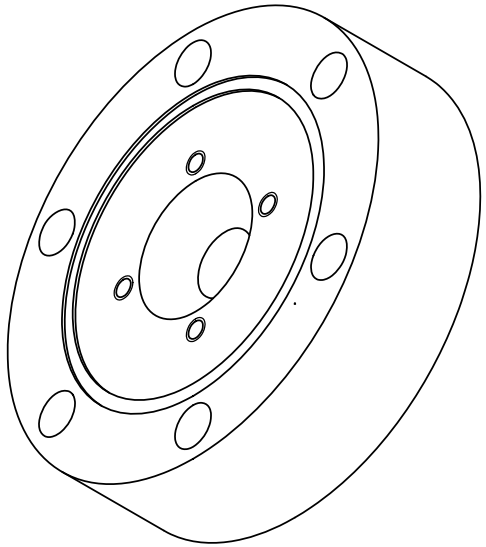

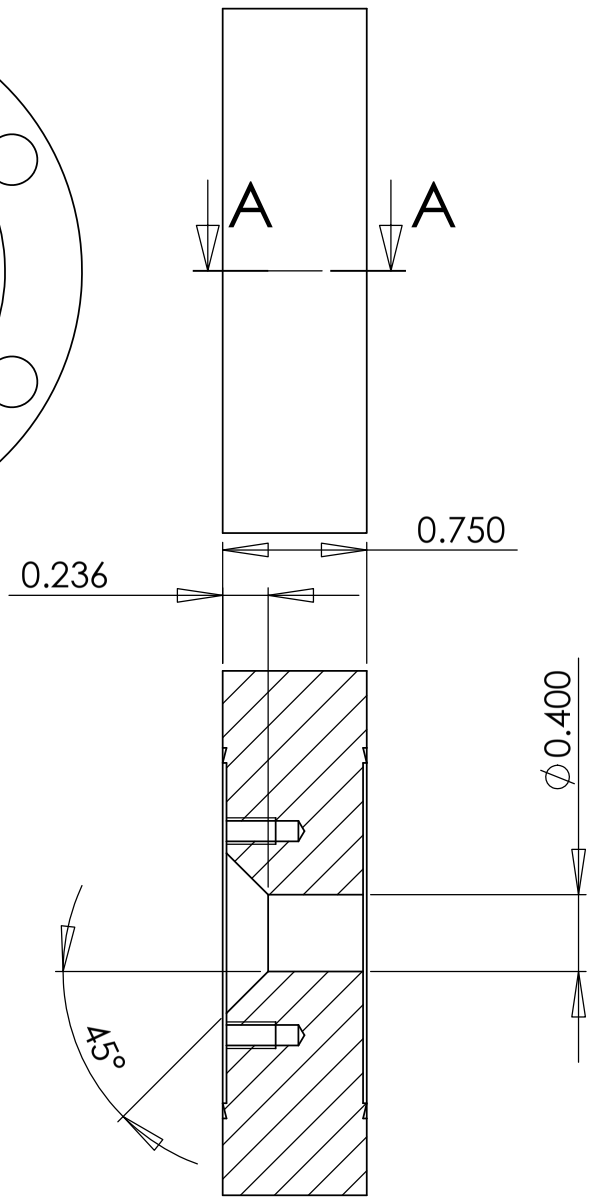

SECTION A-A

PART B
Quantity 2

Retaining ring, made of UHV quality stainless steel

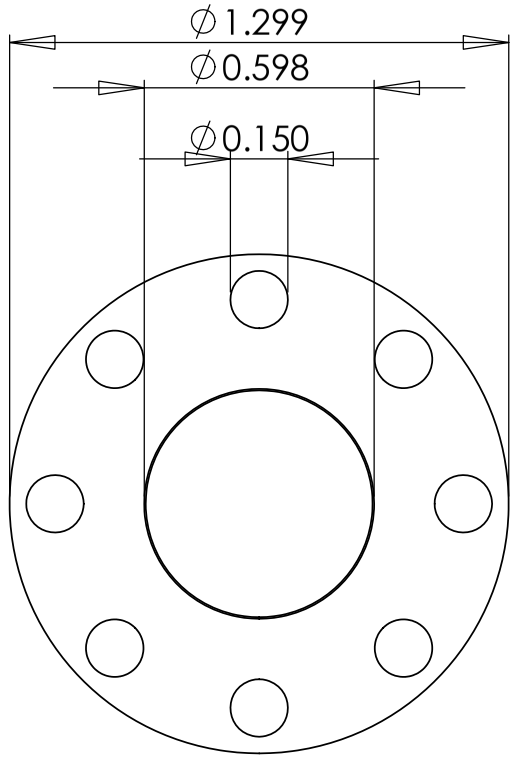

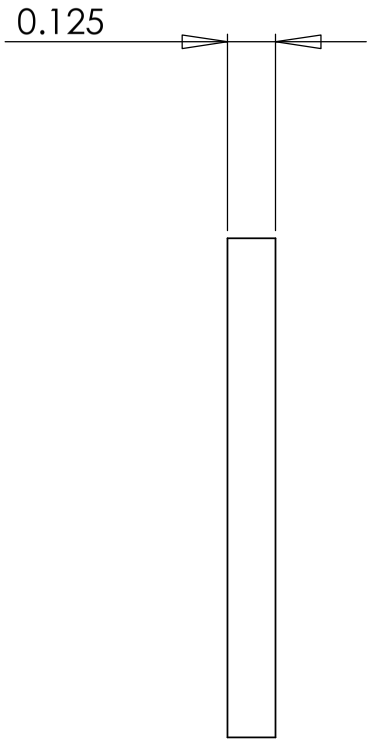

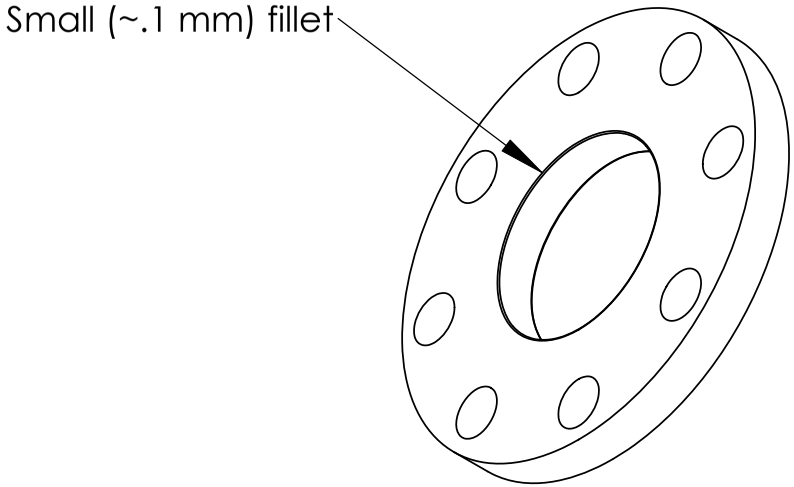

PART C
Quantity 1

Differential pumping tube

UHV steel tube welded
to UHV compatible steel ball
with through hole

Ball centered lengthwise along tube

Tube cross section is based on
MDC part number 480000 vacuum tubing

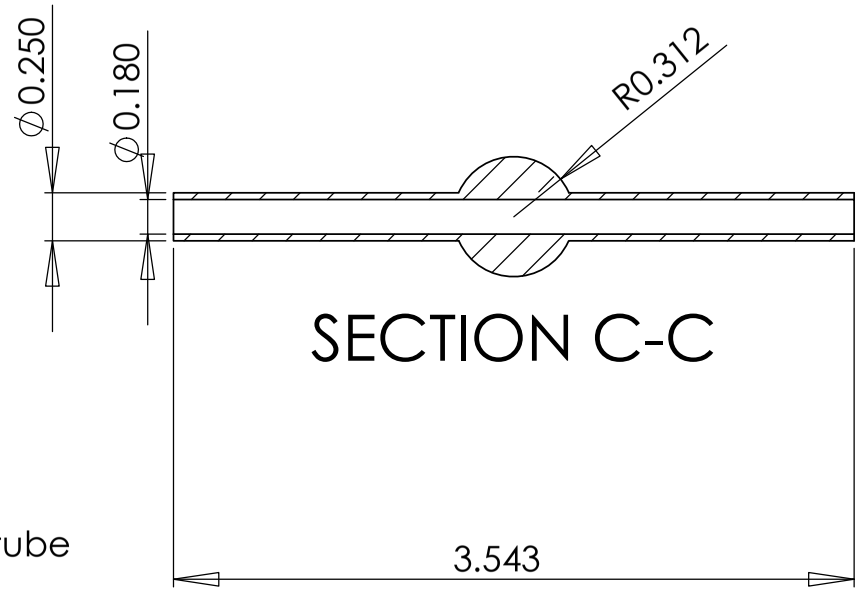

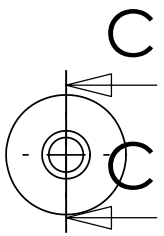

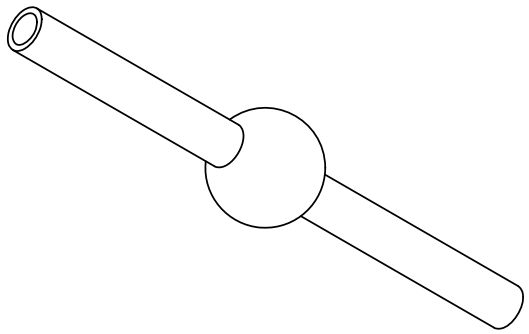

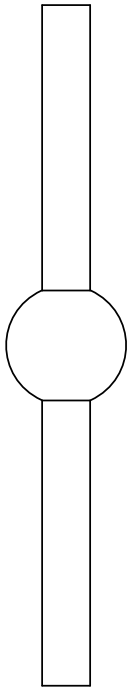

PART D
Quantity 1

Differential pumping tube 2
Same as PART C, but with a different tube length

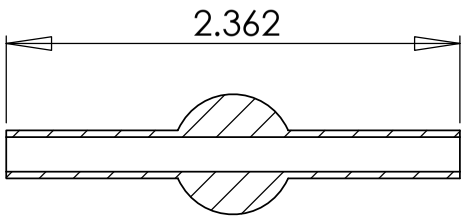

SECTION D-D

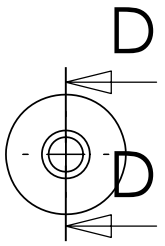

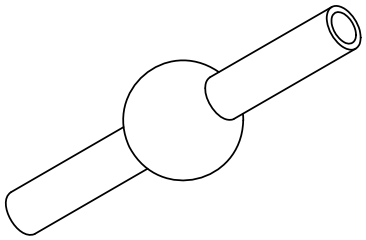

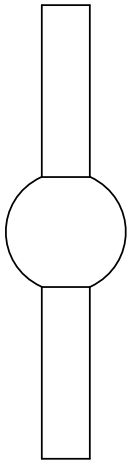

Example: assembled differential
pumping tube with alignment adjustment

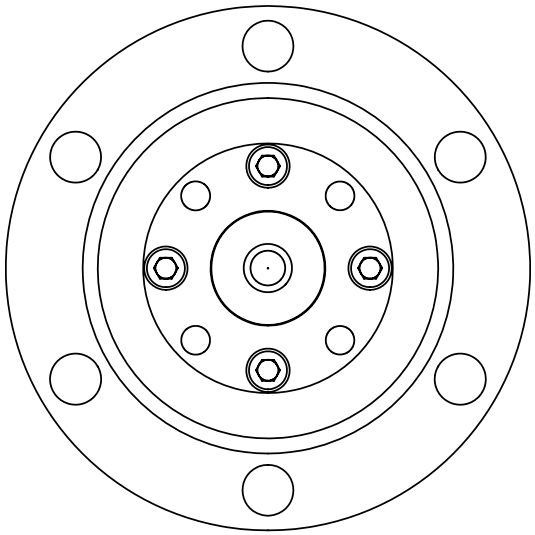

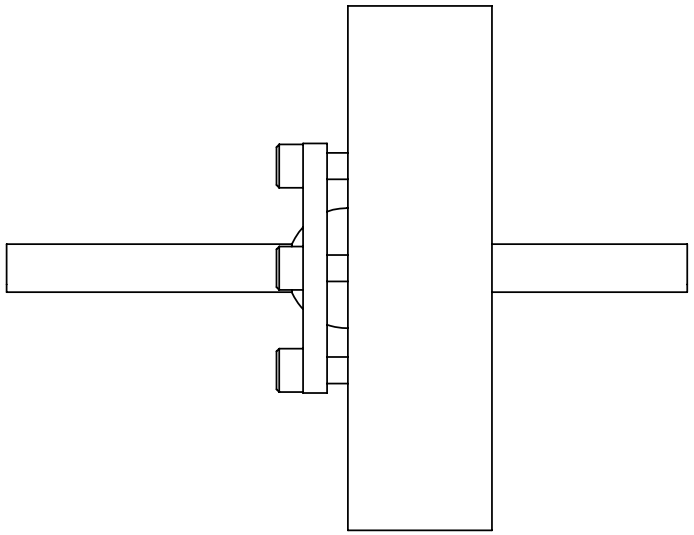

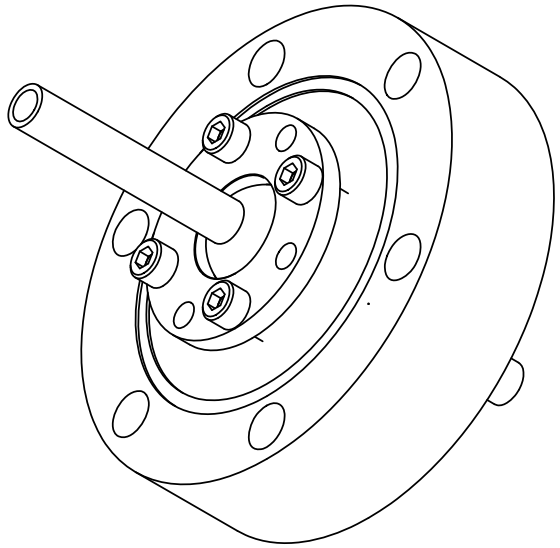

REV.	DATE	DESCRIPTION

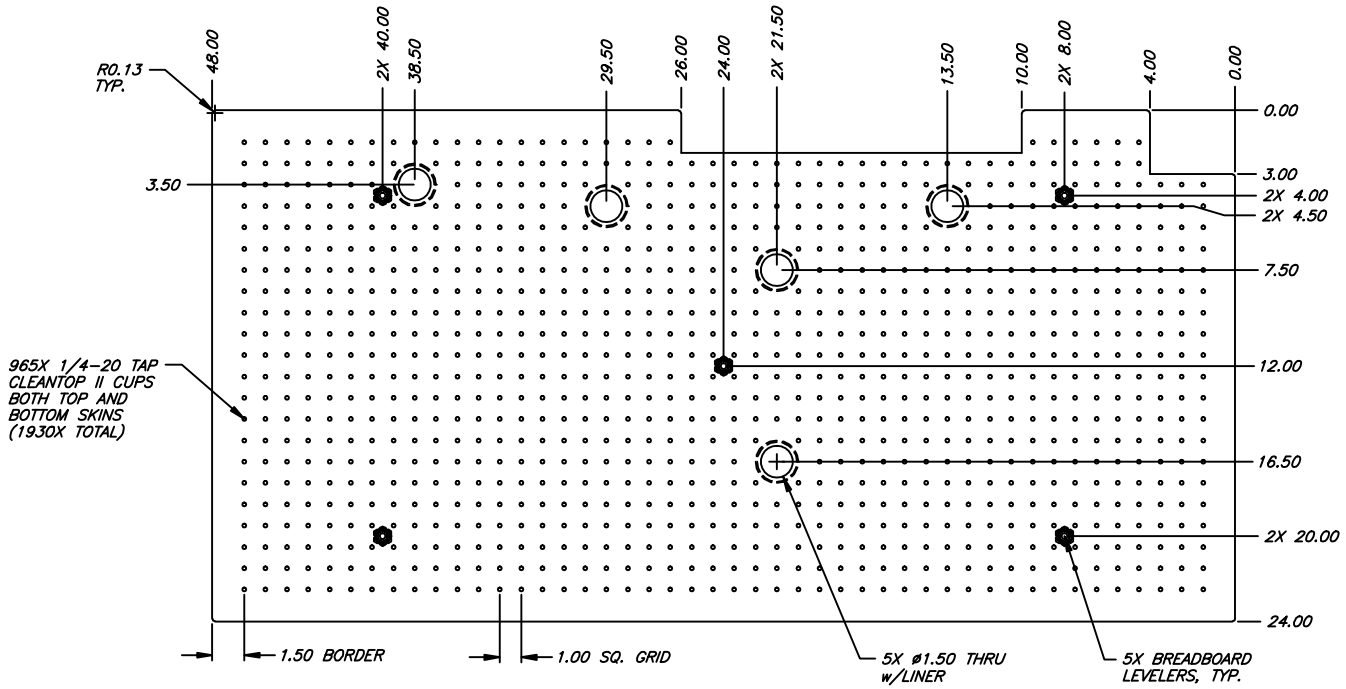

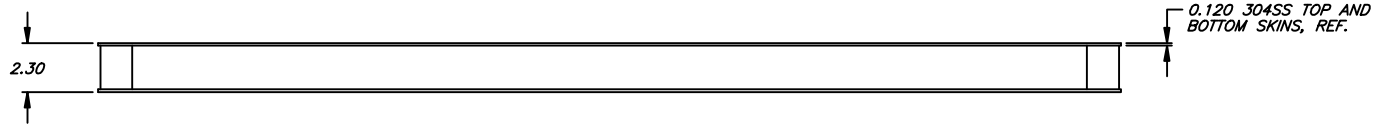

TMC SALES DRAWING
Date: _____
Eng: _____

UNCONTROLLED

NOTES:
1. BB/24x48x2.49 w/NOTCHES, LEVELERS AND HOLES/NON-MAG.
2. .120 304SS TOP + BOTTOM SKINS.
3. 1930X CLEANTOP II NYLON CUPS (CUPS BOTH SIDES).
4. 5X BREADBOARD LEVELERS, NON-MAGNETIC.
5. NON-MAGNETIC CORE, SIDEWALLS AND INSERTS.

Technical Manufacturing Corporation
15 Centennial Drive, Peabody,MA 01960,USA
Tel:978-532-6330, Fax:978-531-8682

REF:
MATERIAL:
FINISH:

TITLE: BB/24x48x2.30 w/NOTCHES, LEVELERS AND HOLES/NON-MAG.

TOLERANCES UNLESS NOTED: .XXX=±.005/.XX=±.02/FRACTION=±1/16 <±.5°

DRW.	CH	07-19-17	C	DWG NO. MIT/38338-3	REV.
CHK.					

Appendix C

Window coating specs

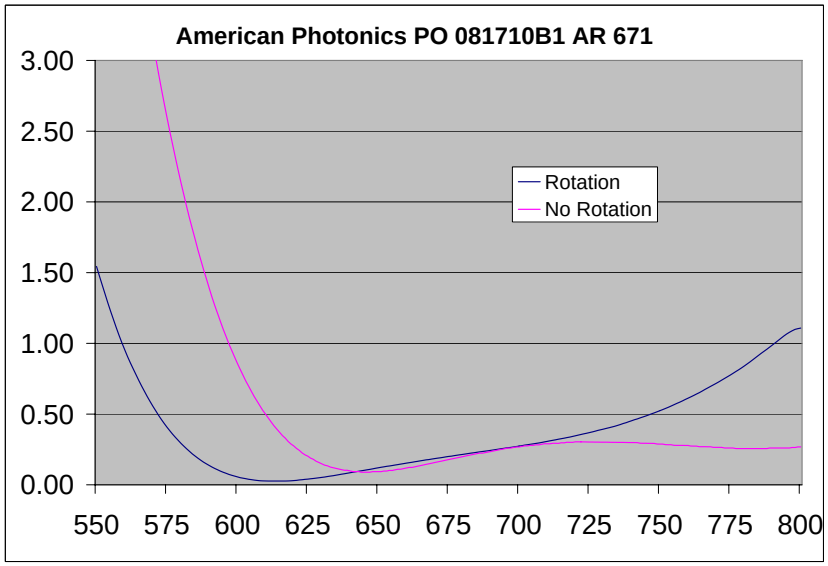

Figure C-1: Measured AR coating performance for 671nm coating windows. The "No Rotation" trace is for the out-of-vacuum surface of the side bucket windows, for which the coating applied onto the stationary window..

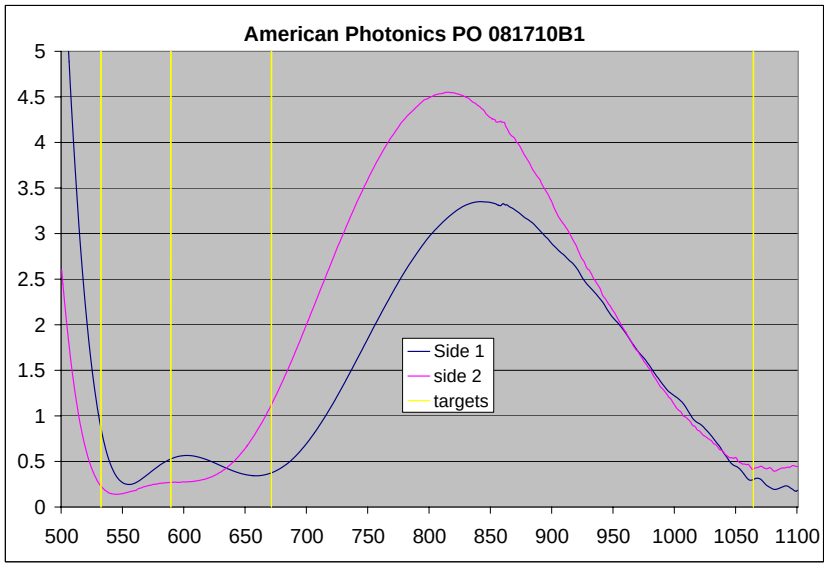

Figure C-2: Measured AR coating performance for multi-wavelength coating windows..

Appendix D

Experiment enclosure design

The parts (part numbers from the 80/20 company) as specified in Table D.1 create an enclosure with total exterior dimensions width x length x height of 63.875 x 100.875 x 60 inches (interior 60.865 x 97.875 x 57 inches). To increase the size by dW x dL x dH, modify the parts as follows. Increase B's length by dW; A by dL; and D, E, and G by dH. Increase F and J by $dL/2$. Increase H and I by $dL/8$. Increase the height of plastic panels K and L by dH, and their width by $dL/8$.

Note that this part list includes parts necessary for doors on the sides of the enclosures only. It does not include parts for doors at the two ends, since in our apparatus these ends are blocked by objects that do not allow for the bifold opening design. On these ends, we have used simple sliding doors that grants limited accessibility but require no opening clearance.

The enclosure uses a mix of the 1-inch and 1.5-inch series of 80/20 extrusions. The thicker extrusions are used for structural beams for extra stiffness, while the 1-inch series is used in the bifold doors to keep them light. Using a mixture of these two series is the reason that an extra set of horizontal bars is required to act as the door guides (part F). This small added complexity was deemed to be worth the reduction in door weight.

The enclosure is intended to hung from a framing system above the laser table, and to hang down to a few inches below the table, with a gap of about .5 - 1 inch between the outside of the table and the inside of the enclosure. The 7257 machining

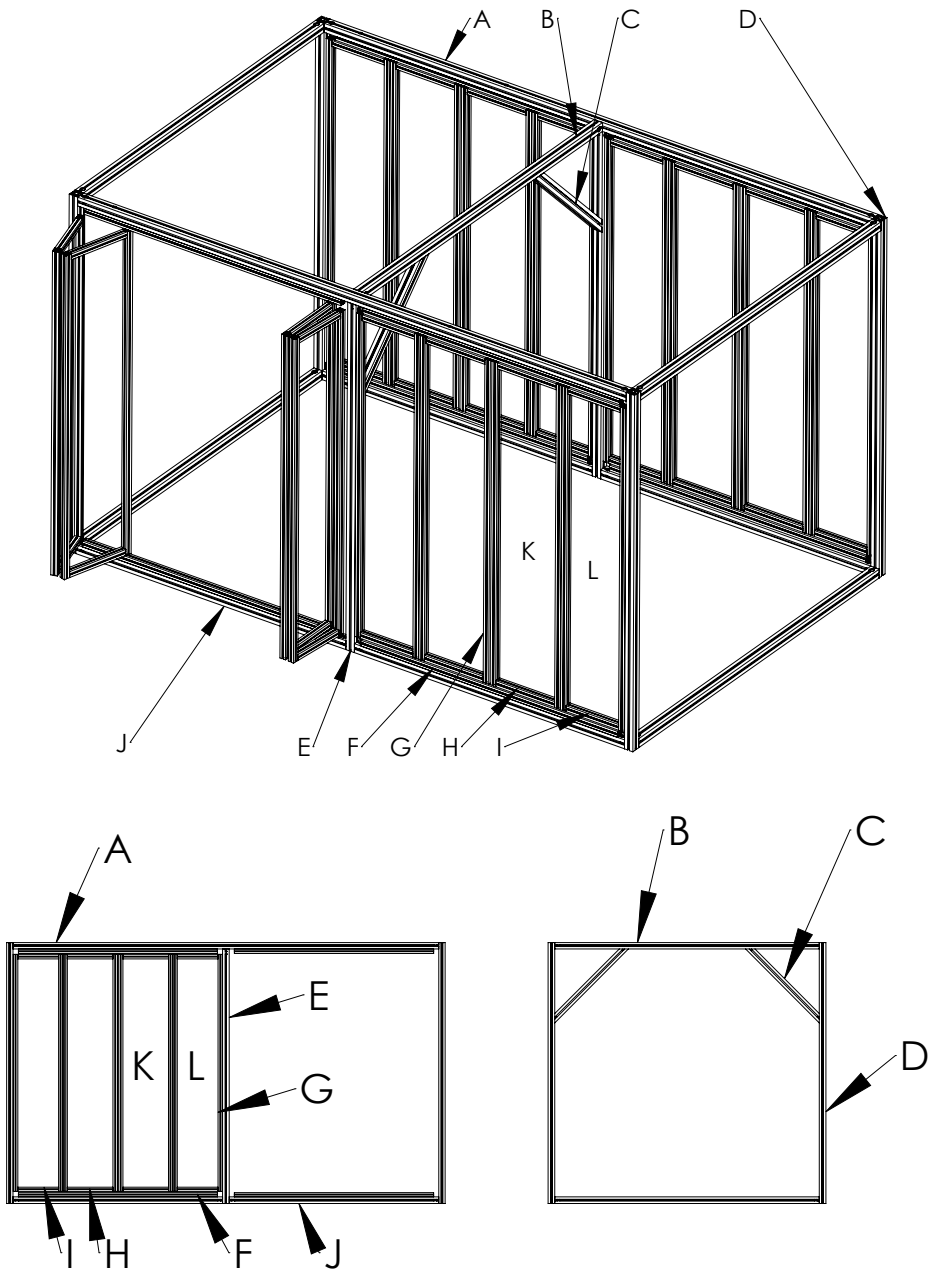

Figure D-1: Experiment enclosure. See Table D.1 for detailed part list. For clarity, only 1 out of the 4 bifold door sets is shown in the lower drawing.

Table D.1: Parts list for enclosure

Label	80/20 Part #	Quantity	Length (in)	Options
A	1515	2	97.875	7010 to length. 7040 sides A and C, both ends. 7257 side A at 6" and 32" from Left End and 6" and 32" from Right End
B	1515	4	60.875	7010 to length. 7040 sides A and C, both ends. 7257 side A at 6" and 24" from Left End and 6" and 24" from Right End
C	2555	2		
D	1515	4	60	7010 to length.
E	1515	2	58.5	7010 to length. 7040 sides A and C, one end only.
F	1010	8	45.79	7010 to length
G	1010	32	54.5	7010 to length. 7061 both ends. 7051 Access holes, style C, in S, both ends
H	1010	16	10.48	7010 to length. 7061 both ends.
I	1010	16	9.36	7010 to length. 7061 both ends.
J	1515	4	48.19	7010 cut to length. 7040 sides A and C, both ends.
K	2610	8		7155 Cut to size 10.98 x 53 inches
L	2610	8		7155 Cut to size 9.86 x 53 inches
	3098	24		
	3383	64		
	2059	8		
	2067	8		
	2103	16		
	2066	16		
	2850	16		
	2116	170 feet		
	2079	24		
	4515	16		
	3321	32		
	3320	32		

operations for parts A and B supply counter-sunk holes for 1/4-20 screw to hang the enclosure. Alternate hanging schemes are possible.

No further machining operations are required to the specified parts. A team of two can assemble the full enclosure in a day. When hanging the doors, to ensure that they open and close smoothly, ensure that their weight is being carried by the door hinges rather than by the door hanger.

Appendix E

Suppression of Density Fluctuations in a Quantum Degenerate Fermi Gas

Suppression of Density Fluctuations in a Quantum Degenerate Fermi Gas

Christian Sanner, Edward J. Su, Aviv Keshet, Ralf Gommers, Yong-il Shin, Wujie Huang, and Wolfgang Ketterle

MIT-Harvard Center for Ultracold Atoms, Research Laboratory of Electronics, and Department of Physics, Massachusetts Institute of Technology, Cambridge Massachusetts 02139, USA

(Received 7 May 2010; published 19 July 2010)

We study density profiles of an ideal Fermi gas and observe Pauli suppression of density fluctuations (atom shot noise) for cold clouds deep in the quantum degenerate regime. Strong suppression is observed for probe volumes containing more than 10 000 atoms. Measuring the level of suppression provides sensitive thermometry at low temperatures. After this method of sensitive noise measurements has been validated with an ideal Fermi gas, it can now be applied to characterize phase transitions in strongly correlated many-body systems.

DOI: 10.1103/PhysRevLett.105.040402 PACS numbers: 03.75.Ss, 05.30.Fk, 67.85.Lm

Systems of fermions obey the Pauli exclusion principle. Processes that would require two fermions to occupy the same quantum state are suppressed. In recent years, several classic experiments have directly observed manifestations of Pauli suppression in Fermi gases. Antibunching and the suppression of noise correlations are a direct consequence of the forbidden double occupancy of a quantum state. Such experiments were carried out for electrons [1–3], neutral atoms [4,5], and neutrons [6]. In principle, such experiments can be done with fermions at any temperature, but in practice low temperatures increase the signal. A second class of (two-body) Pauli suppression effects, the suppression of collisions, requires a temperature low enough such that the de Broglie wavelength of the fermions becomes larger than the range of the interatomic potential and p-wave collisions freeze-out. Experiments observed the suppression of elastic collisions [7] and of clock shifts in radio frequency spectroscopy [8,9].

Here we report on the observation of Pauli suppression of density fluctuations. This is, like the suppression of collisions between different kinds of fermions [10], a many-body phenomenon which occurs only at even lower temperatures in the quantum degenerate regime, where the Fermi gas is cooled below the Fermi temperature and the low lying quantum states are occupied with probabilities close to 1. In contrast, an ideal Bose gas close to quantum degeneracy shows enhanced fluctuations [11].

The development of a technique to sensitively measure density fluctuations was motivated by the connection between density fluctuations and compressibility through the fluctuation-dissipation theorem. In this Letter, we validate our technique for determining the compressibility by applying it to the ideal Fermi gas. In future work, it could be extended to interesting many-body phases in optical lattices which are distinguished by their incompressibility [12]. These include the band insulator, Mott insulator, and also the antiferromagnet for which spin fluctuations, i.e., fluctuations of the difference in density between the two spin states are suppressed.

Until now, sub-Poissonian number fluctuations of ultracold atoms have been observed only for small clouds of bosons with typically a few hundred atoms [13–16] and directly [17,18] or indirectly [19] for the bosonic Mott insulator in optical lattices. For fermions in optical lattices, the crossover to an incompressible Mott insulator phase was inferred from the fraction of double occupations [20] or the cloud size [21]. Here we report the observation of density fluctuations in a large cloud of fermions, showing sub-Poissonian statistics for atom numbers in excess of 10 000 per probe volume.

The basic concept of the experiment is to repeatedly produce cold gas clouds and then count the number of atoms in a small probe volume within the extended cloud. Many iterations allow us to determine the average atom number N in the probe volume and its variance $(\Delta N)^2$. For independent particles, one expects Poisson statistics, i.e., $(\Delta N)^2/\langle N\rangle = 1$. This is directly obtained from the fluctuation-dissipation theorem $(\Delta N)^2/\langle N\rangle = nk_BT\kappa_T$, where n is the density of the gas, and κ_T the isothermal compressibility. For an ideal classical gas $\kappa_T = 1/(nk_BT)$,

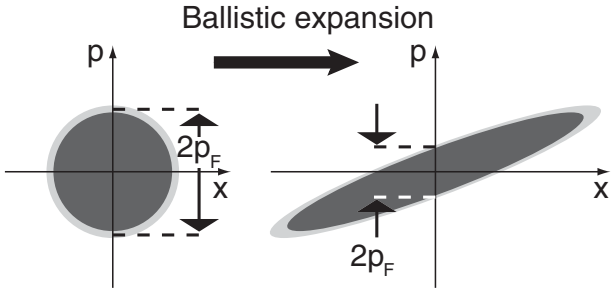

FIG. 1. Phase space diagram of ballistic expansion of a harmonically trapped Fermi gas. Ballistic expansion conserves phase space density and shears the initially occupied spherical area into an ellipse. In the center of the cloud, the local Fermi momentum and the sharpness of the Fermi distribution are scaled by the same factor, keeping the ratio of local temperature to Fermi energy constant. The same is true for all points in the expanded cloud relative to their corresponding unscaled in-trap points.

and one retrieves Poissonian statistics. For an ideal Fermi gas close to zero temperature with Fermi energy E_F, $\kappa_T = 3/(2nE_F)$, and the variance $(\Delta N)^2$ is suppressed below Poissonian fluctuations by the Pauli suppression factor $3k_BT/(2E_F)$. All number fluctuations are thermal, as indicated by the proportionality of $(\Delta N)^2$ to the temperature in the fluctuation-dissipation theorem. Only for the ideal classical gas, where the compressibility diverges as $1/T$, one obtains Poissonian fluctuations even at zero temperature.

The counting of atoms in a probe volume can be done with trapped atoms, or after ballistic expansion. Ballistic expansion maintains the phase space density and therefore the occupation statistics. Consequently, density fluctuations are exactly rescaled in space by the ballistic expansion factors as shown in Fig. 1 [22,23]. Note that this rescaling is a unique property of the harmonic oscillator potential, so future work on density fluctuations in optical lattices must employ in-trap imaging. For the present work, we chose ballistic expansion. This choice increases the number of fully resolved bins due to optical resolution and depth of field, it allows adjusting the optimum optical density by choosing an appropriate expansion time, and it avoids image artifacts at high magnification.

We first present our main results, and then discuss important aspects of sample preparation, calibration of absorption cross section, data analysis and corrections for photon shot noise. Figure 2(a) shows an absorption image of an expanding cloud of fermionic atoms. The probe volume, in which the number of atoms is counted, is chosen to be 26 μm in the transverse directions, and extends through the entire cloud in the direction of the line of sight. The large transverse size avoids averaging of fluctuations due to finite optical resolution. From 85 such images, after careful normalization [24], the variance in the measured atom number is determined as a function of position. After subtracting the photon shot noise contribution, a 2D image of the atom number variance $(\Delta N)^2$ is obtained. For a Poissonian sample (with no suppression of fluctuations), this image would be identical to an absorption image showing the number of atoms per probe volume. This is close to the situation for the hottest cloud (the temperature was limited by the trap depth), whereas the colder clouds show a distinct suppression of the atom number variance, especially in the center of the cloud where the local T/T_F is smallest.

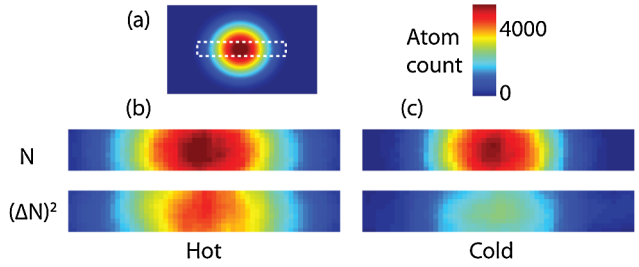

FIG. 2 (color online). Comparison of density images to variance images. For Poissonian fluctuations, the two images at a given temperature should be identical. The variance images were obtained by determining the local density fluctuations from a set of 85 images taken under identical conditions. (a) Two dimensional image of the optical density of an ideal Fermi gas after 7 ms of ballistic expansion. The noise data were taken by limiting the field of view to the dashed region of interest, allowing for faster image acquisition. (b) For the heated sample, variance and density pictures are almost identical, implying only modest deviation from Poissonian statistics. (c) Fermi suppression of density fluctuations deep in the quantum degenerate regime manifests itself through the difference between density and variance picture. Especially in the center of the cloud, there is a large suppression of density fluctuations. The variance images were smoothed over 6×6 bins. The width of images (b) and (c) is 2 mm.

In Fig. 3, profiles of the variance are compared to theoretical predictions [25,26]. Density fluctuations at wave vector q are proportional to the structure factor $S(q, T)$. Since our probe volume (transverse size 26 μm) is much larger than the inverse Fermi wave vector of the expanded cloud ($1/q_F = 1.1$ μm), $S(q = 0, T)$ has been integrated along the line of sight for comparison with the experimental profiles. Within the local density approximation, $S(q = 0, T)$ at a given position in the trap is the binomial variance $n_k(1 - n_k)$ integrated over all momenta, where the occupation probability $n_k(k, \mu, T)$ is obtained from the Fermi-Dirac distribution with a local chemical potential μ determined by the shape of the trap. Figure 4 shows the dependence of the atom number variance on atom number for the hot and cold clouds. A statistical analysis of the data used in the figure is in [24].

The experiments were carried out with typically 2.5×10^6 ^{6}Li atoms per spin state confined in a round crossed dipole trap with radial and axial trap frequencies $\omega_r = 2\pi \times 160$ s^{-1} and $\omega_z = 2\pi \times 230$ s^{-1} corresponding to an in-trap Fermi energy of $E_F = k_B \times 2.15$ μK. The sam-

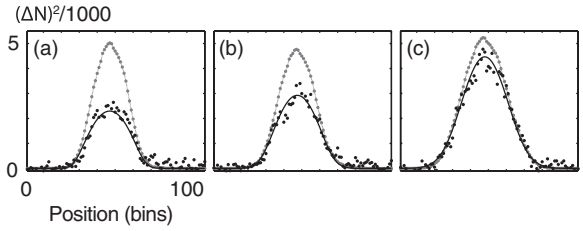

FIG. 3. Comparison of observed variances (black dots) with a theoretical model (black line) and the observed atom number (gray), at three different temperatures (a, b, and c), showing 50, 40, and 15% suppression. Noise thermometry is implemented by fitting the observed fluctuations, resulting in temperatures T/T_F of $0.23 \pm .01$, $0.33 \pm .02$, and $0.60 \pm .02$. This is in good agreement with temperatures $0.21 \pm .01$, $0.31 \pm .01$, and $0.6 \pm .1$ obtained by fitting the shape of the expanded cloud [32]. The quoted uncertainties correspond to 1 standard deviation and are purely statistical.

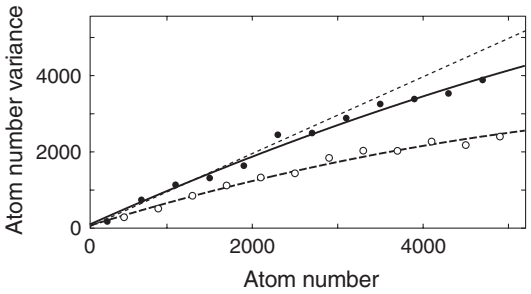

FIG. 4. Atom number variance vs average atom number. For each spatial position, the average atom number per bin and its variance were determined using 85 images. The filled and open circles in the figure are averages of different spatial bin positions with similar average atom number. For a hot cloud at $T/T_F = 0.6$ (filled circles), the atom number variance is equal to the average atom number (dotted line, full Poissonian noise) in the spatial wings where the atom number is low. The deviation from the linear slope for a cold cloud at $T/T_F = 0.21$ (open circles) is due to Pauli suppression of density fluctuations. There is also some suppression at the center of the hot cloud, where the atom number is high. The solid and dashed lines are quadratic fits for the hot and cold clouds to guide the eye.

ple was prepared by laser cooling followed by sympathetic cooling with ^{23}Na in a magnetic trap. ^{6}Li atoms in the highest hyperfine state were transferred into the optical trap, and an equal mixture of atoms in the lowest two hyperfine states was produced. The sample was then evaporatively cooled by lowering the optical trapping potential at a magnetic bias field $B = 320 \pm 5$ G where a scattering length of -300 Bohr radii ensured efficient evaporation. Finally, the magnetic field was increased to $B = 520 \pm 5$ G, near the zero crossing of the scattering length. Absorption images were taken after 7 ms of ballistic expansion.

We were careful to prepare all samples with similar cloud sizes and central optical densities to ensure that they were imaged with the same effective cross section and resolution. Hotter clouds were prepared by heating the colder cloud using parametric modulation of the trapping potential. For the hottest cloud this was done near 520 G to avoid excessive evaporation losses.

Atomic shot noise dominates over photon shot noise only if each atom absorbs several photons. As a result, the absorption images were taken using the cycling transition to the lowest lying branch of the $^2P_{3/2}$ manifold. However, the number of absorbed photons that could be tolerated was severely limited by the acceleration of the atoms by the photon recoil, which Doppler shifts the atoms out of resonance. Consequently, the effective absorption cross section depends on the probe laser intensity and duration. To remove the need for nonlinear normalization procedures, we chose a probe laser intensity corresponding to an average of only 6 absorbed photons per atom during a 4 μs exposure. At this intensity, about 12% of the ^{6}Li saturation intensity, the measured optical density was 20% lower than its low-intensity value [24]. For each bin, the atom number variance $(\Delta N)^2$ is obtained by subtracting the known photon shot noise from the variance in the optical density $(\Delta \mathrm{OD})^2$ [24]:

$$\frac{\sigma^2}{A^2}(\Delta N)^2 = (\Delta \mathrm{OD})^2 - \frac{1}{\langle N_1 \rangle} - \frac{1}{\langle N_2 \rangle} \qquad (1)$$

Here, $\langle N_1 \rangle (\langle N_2 \rangle)$ are the average photon numbers per bin of area A in the image with (without) atoms and σ is the absorption cross section.

The absorption cross section is a crucial quantity in the conversion factor between the optical density and the number of detected atoms. For the cycling transition, the resonant absorption cross section is 2.14×10^{-13} m^2. Applying the measured 20% reduction mentioned above leads to a value of 1.71×10^{-13} m^2. This is an upper limit to the cross section due to imperfections in polarization and residual line broadening. An independent estimate of the effective cross section of 1.48×10^{-13} m^2 was obtained by comparing the integrated optical density to the number of fermions necessary to fill up the trap to the chemical potential. The value of the chemical potential was obtained from fits to the ballistic expansion pictures that allowed independent determination of the absolute temperature and the fugacity of the gas. We could not precisely assess the accuracy of this value of the cross section, since we did not fully characterize the effect of a weak residual magnetic field curvature on trapping and on the ballistic expansion. The most accurate value for the effective cross section was determined from the observed atom shot noise itself. The atom shot noise in the wings of the hottest cloud is Poissonian, and this condition determines the absorption cross section. Requiring that the slope of variance of the atom number $(\Delta N)^2$ vs atom number N is unity (see Fig. 4) results in a value of $(1.50 \pm 0.12) \times 10^{-13}$ m^2 for the effective cross section in good agreement with the two above estimates.

The spatial volume for the atom counting needs to be larger than the optical resolution. For smaller bin sizes (i.e., small counting volumes), the noise is reduced since the finite spatial resolution and depth of field blur the absorption signal. In our setup, the smallest bin size without blurring was determined by the depth of field, since the size of the expanded cloud was larger than the depth of field associated with the diffraction limit of our optical system. We determined the effective optical resolution by binning the absorption data over more and more pixels of the CCD camera, and determining the normalized central variance $(\Delta N)^2/N$ vs bin size [24]. The normalized variance increased and saturated for bin sizes larger than 26 μm (in the object plane), and this bin size was used in the data analysis. We observe the same suppression ratios for bin sizes as large as 40 μm, corresponding to more than 10 000 atoms per bin.

For a cold fermion cloud, the zero temperature structure factor $S(q)$ becomes unity for $q > 2q_F$. This reflects the

fact that momentum transfer above $2q_F$ to any particle will not be Pauli suppressed by occupation of the final state. In principle, this can be observed by using bin sizes smaller than the Fermi wavelength, or by Fourier transforming the spatial noise images. For large values of q, Pauli suppression of density fluctuations should disappear, and the noise should be Poissonian. However, our imaging system loses its contrast before $q \approx 2q_F$ [24].

Observation of density fluctuations, through the fluctuation-dissipation theorem, determines the product of temperature and compressibility. It provides an absolute thermometer, as demonstrated in Fig. 3 if the compressibility is known or is experimentally determined from the shape of the density profile of the trapped cloud [17,27]. Because variance is proportional to temperature for $T \ll T_F$, noise thermometry maintains its sensitivity at very low temperature, in contrast to the standard technique of fitting spatial profiles.

Density fluctuations lead to Rayleigh scattering of light. The differential cross section for scattering light of wave vector k by an angle θ is proportional to the structure factor $S(q)$, where $q = 2k\sin(\theta/2)$ [26]. In this work, we have directly observed the Pauli suppression of density fluctuations and therefore $S(q) < 1$, implying suppression of light scattering at small angles (corresponding to values of q inversely proportional to our bin size). How are the absorption images affected by this suppression? Since the photon recoil was larger than the Fermi momentum of the expanded cloud, large-angle light scattering is not suppressed. For the parameters of our experiment, we estimate that the absorption cross section at the center of a $T = 0$ Fermi cloud is reduced by only 0.3% due to Pauli blocking [28]. Although we have not directly observed Pauli suppression of light scattering, which has been discussed for over 20 years [28–30], by observing reduced density fluctuations we have seen the underlying mechanism for suppression of light scattering.

In conclusion, we have established a sensitive technique for determining atomic shot noise and observed the suppression of density fluctuations in a quantum degenerate ideal Fermi gas. This technique is promising for thermometry of strongly correlated many-body systems and for observing phase-transitions or cross-overs to incompressible quantum phases.

We acknowledge Joseph Thywissen and Markus Greiner for useful discussions. This work was supported by NSF and the Office of Naval Research, AFOSR (through the MURI program), and under Army Research Office grant no. W911NF-07-1-0493 with funds from the DARPA Optical Lattice Emulator program.

Note added in proof.—Results similar to ours are reported in Ref. [31].

[1] W. D. Oliver, J. Kim, R. C. Liu, and Y. Yamamoto, Science **284**, 299 (1999).
[2] M. Henny *et al.*, Science **284**, 296 (1999).
[3] H. Kiesel, A. Renz, and F. Hasselbach, Nature (London) **418**, 392 (2002).
[4] T. Rom *et al.*, Nature (London) **444**, 733 (2006).
[5] T. Jeltes *et al.*, Nature (London) **445**, 402 (2007).
[6] M. Iannuzzi *et al.*, Phys. Rev. Lett. **96**, 080402 (2006).
[7] B. DeMarco *et al.*, Phys. Rev. Lett. **82**, 4208 (1999).
[8] M. W. Zwierlein, Z. Hadzibabic, S. Gupta, and W. Ketterle, Phys. Rev. Lett. **91**, 250404 (2003).
[9] S. Gupta *et al.*, Science **300**, 1723 (2003).
[10] B. DeMarco, S. B. Papp, and D. S. Jin, Phys. Rev. Lett. **86**, 5409 (2001).
[11] J. Estève *et al.*, Phys. Rev. Lett. **96**, 130403 (2006).
[12] Q. Zhou, Y. Kato, N. Kawashima, and N. Trivedi, arXiv:0901.0606.
[13] C. S. Chuu *et al.*, Phys. Rev. Lett. **95**, 260403 (2005).
[14] J. Estève *et al.*, Nature (London) **455**, 1216 (2008).
[15] S. Whitlock, C. F. Ockeloen, and R. J. C. Spreeuw, Phys. Rev. Lett. **104**, 120402 (2010).
[16] A. Itah *et al.*, Phys. Rev. Lett. **104**, 113001 (2010).
[17] N. Gemelke, X. Zhang, C. L. Hung, and C. Chin, Nature (London) **460**, 995 (2009).
[18] M. Greiner (unpublished).
[19] M. Greiner, O. Mandel, T. W. Hänsch, and I. Bloch, Nature (London) **419**, 51 (2002).
[20] R. Jördens *et al.*, Nature (London) **455**, 204 (2008).
[21] U. Schneider *et al.*, Science **322**, 1520 (2008).
[22] S. Gupta, Z. Hadzibabic, J. R. Anglin, and W. Ketterle, Phys. Rev. Lett. **92**, 100401 (2004).
[23] G. M. Bruun and C. W. Clark, Phys. Rev. A **61**, 061601(R) (2000).
[24] See supplementary material at http://link.aps.org/supplemental/10.1103/PhysRevLett.105.040402 for additional details.
[25] Y. Castin, in *Proceedings of the International School of Physics Enrico Fermi, Course CLXIV*, edited by M. Inguscio, W. Ketterle, and C. Salomon (IOS, Amsterdam, 2008).
[26] D. Pines and P. Nozières, *The Theory of Quantum Liquids* (Addison-Wesley, MA, 1988), Vol. 1.
[27] Q. Zhou and T. L. Ho, arXiv:0908.3015.
[28] A. Görlitz, A. P. Chikkatur, and W. Ketterle, Phys. Rev. A **63**, 041601(R) (2001).
[29] K. Helmerson, M. Xiao, and D. E. Pritchard, in *International Quantum Electronics Conference 1990, Book of Abstracts*, econf QTHH4 (1990).
[30] B. Shuve and J. H. Thywissen, J. Phys. B **43**, 015301 (2010). (and references therein)
[31] T. Mueller *et al.*, Phys. Rev. Lett. **105**, 040401 (2010).
[32] W. Ketterle and M. W. Zwierlein, in *Proceedings of the International School of Physics Enrico Fermi, Course CLXIV*, edited by M. Inguscio, W. Ketterle, and C. Salomon (IOS, Amsterdam, 2008).

Suppression of Density Fluctuations in a Quantum Degenerate Fermi Gas: Supplementary Information

EXPERIMENTAL DETAILS

To accurately measure the atom number variance it is necessary to eliminate patterns in the absorption images whose fluctuations increase the observed noise. Weak reflections of the probe beam from the walls of the glass cell and from optical elements in the imaging system can interfere with the probe beam itself, leading to spatial fluctuations in its intensity profile. To reduce interference fringes and ensure uniform illumination, the central area of the probe beam is imaged onto the sample through a 2 mm aperture. Even though the residual fringes are small, there are two significant effects of inhomogeneous illumination which must be addressed.

First, if the time elapsed between the image with atoms and the reference image without atoms is too large, mechanical vibrations of the optics will cause the intensity profile of the probe to change between the two images, creating artifacts in the absorption image. To reduce this effect, we operate our CCD in fast kinetics mode, with a time interval $\approx 500\mu s$ between exposures. Since there is no longer enough time for the atoms to exit the frame between images, before taking the reference image we optically pump the atoms from the $|1\rangle$ state to the $|6\rangle$ state, and from the $|2\rangle$ state to the $|5\rangle$ state ($|1\rangle$ refers to the lowest hyperfine state, etc.), by exciting them to the $m_J = 1/2$ excited state manifold. At the magnetic fields used in the experiment, these levels are separated in frequency from the $|2\rangle$ state used for imaging by ≈ 2 GHz and contribute negligibly to resonant imaging.

Second, if the average probe intensity is too high, the atoms subjected to higher intensities will have a lower effective cross-section, and so any spatial fluctuations in the beam intensity will be 'imprinted' onto the absorption images. As a result, in our experiment we use a probe beam with maximum intensity of 0.12 of the saturation intensity I_{sat}=2.54 mW/cm^2, where these effects are relatively small. The variation of optical density with intensity is shown in Fig. 1.

Additionally, the exposure time must be kept very short to prevent the atoms from moving between pixels during the exposure. The expected motion of atoms during the 4 μs exposure is on the order of 1 μm, much smaller than the effective pixel size.

NOISE DETERMINATION

In this experiment the local atom number variance is determined by comparing the measured number of atoms in the same bin across a series of images. To do this, we must first eliminate the effect of fluctuations in the total atom number between experimental cycles. Initially, we select the 85 images used in the analysis from a larger group of ≈ 150 images, using an automated procedure to choose the images whose total atom numbers are closest to the center of the distribution. A very small number of images ($< 1\%$) are manually excluded because of obvious artifacts in the frame due to dust particles or other large perturbations. Then, we subtract a fitted profile from each OD image before computing the variance. Initially we subtracted a fitted 2D Thomas-Fermi profile, but we replaced this with a Gaussian fit which had an insignificant effect on the variances, while taking considerably less computation time.

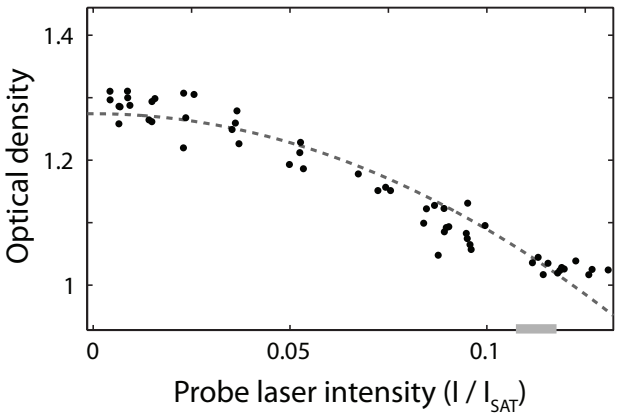

FIG. 1: Determination of the absorption cross section. The observed optical density decreases with increasing probe light intensity. The line is a quadratic fit to the data. The reduction of the cross section is mainly due to the Doppler effect caused by acceleration of the atoms by radiation pressure; a smaller reduction results from the partial saturation of the optical transition. At the probe light intensity chosen in this study (shaded bar), the number of photons absorbed per atoms is about 6. The decrease of the cross section is slightly larger than that predicted by simple models.

We then compute the variance in optical density at each position. That variance has contributions from photon and atom shot noise, given by the following formula:

$$(\Delta(OD))^2 = \frac{1}{\langle N_1 \rangle} + \frac{1}{\langle N_2 \rangle} + \frac{\sigma^2}{A^2}(\Delta N_{atom})^2 \qquad (1)$$

This equation holds bin by bin: N_1 is the average number of photons measured in a given bin position for the image with atoms, and N_2 is the average number of photons measured in that bin for the reference image. $(\Delta N_{atom})^2$ is the variance in atom number for that bin, σ is the

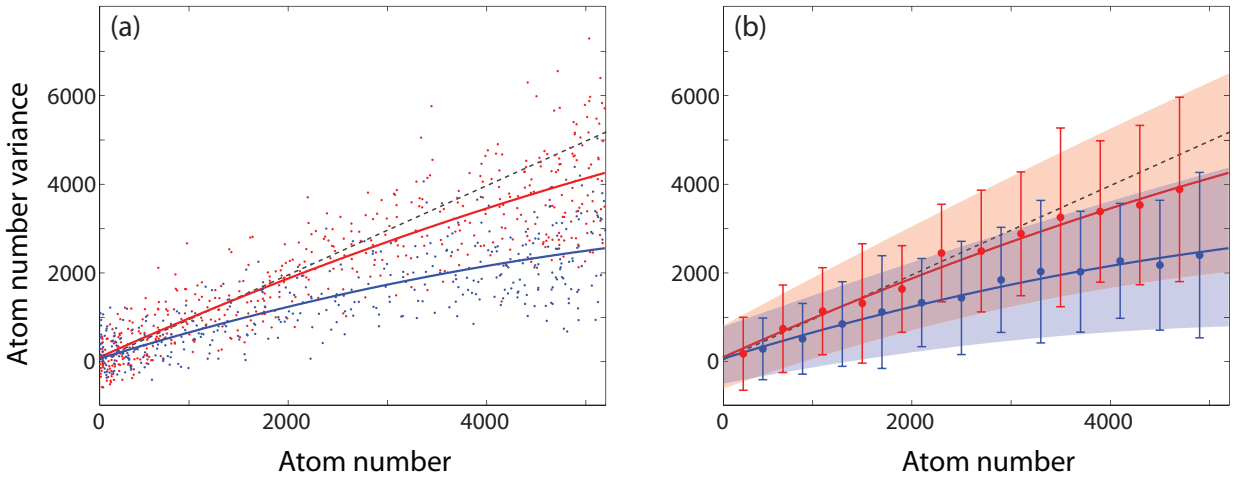

FIG. 2: Atom number variance vs. atom number. (a) Data for all of the resolution elements is plotted. Red points are from the hot cloud at $T/T_F = 0.6$, blue points from the cold cloud at $T/T_F = 0.21$. There is significant scatter in the variance data, and there are many "cold" pixels which actually have higher variance than their corresponding "hot" pixel. (b) The red and blue shaded regions indicate the expected 2σ scatter in sample variance that is expected due to atom and photon counting statistics. The large circles are variance data averaged over pixels with similar atom number for hot (red) and cold (blue) cloud. The bars show the measured 2σ scatter of the data points. The measured scatter agrees very well with the expected scatter, indicating that the scatter of the data is fully accounted for by counting statistics. Negative values of the observed atom number variance result from the subtraction of photon shot noise.

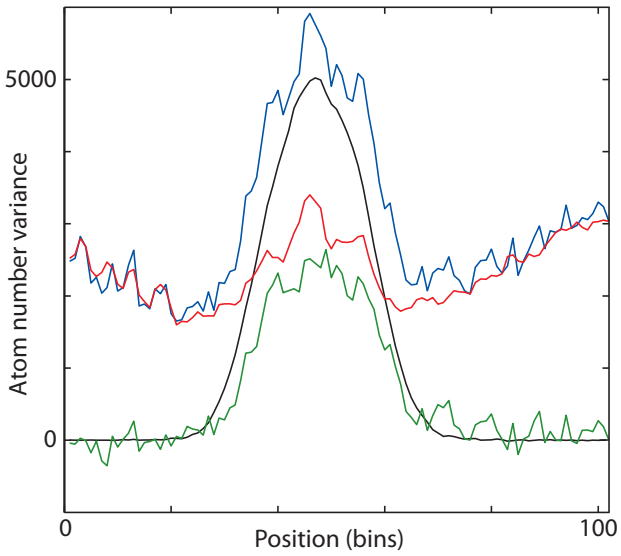

FIG. 3: Determination of profiles of the atom number variance for a cold cloud. For each bin, the total photon count is determined, and its contribution (red) to the total variance of the optical density (blue) is subtracted. The obtained atom number variance (green) is compared to the average atom number (black). The displayed trace reveals 50% noise suppression in the center of the cloud. The apparently high suppression of atom variation in the wings is a statistical fluctuation. Fig. 2 shows that the suppression is monotonic in atomic density.

absorption cross section, and A is the effective bin area. The atom number variance is isolated by calculating the first two photon shot noise terms and subtracting them. The analysis used in the paper also subtracts contributions from detector read noise and photon shot noise in the dark field, but these are fairly small contributions.

The determination of N_1 and N_2 depends on the CCD gain, which is measured to be 1.18 (counts/electron) from ≈ 240 pairs of images without atoms, employing the assumption that the detector statistics are Poissonian. After the subtraction of photon shot noise (and technical noise), the remaining variance in optical density is due to the atom number variance. Fig. 3 shows the contributions of photon and atom number variance to the overall noise in optical density.

The large scatter of the measured atom number variance, as depicted in Fig. 2, is not primarily due to technical noise, but instead a statistical property of the sampling distribution of the variance. The shaded areas are derived from theoretical values for the variance of the sample variance. This is given by

$$\mathrm{Var}(\mathrm{Var}(N)) = \frac{(m-1)^2}{m^3}\mu_4 - \frac{(m-1)(m-3)}{m^3}\mu_2 \quad (2)$$

where m is the number of observations in each sample. The moments μ_2 and μ_4 are the central moments of the population distribution. For a Poisson distribution, $\mu_2 = \langle N\rangle^3$ and $\mu_4 = \langle N\rangle(1 + 3\langle N\rangle)$, and for $m, \langle N\rangle \gg 1$, this expression reduces to $2\langle N\rangle^2/m$. Fig. 2b shows the

comparison between the expected and measured variance in the sample variance.

IMAGING SYSTEM CHARACTERIZATION

The blurring of adjacent pixels due to finite optical resolution effectively decreases the measured atom number variance. This effect is avoided by binning the data using a sufficiently large bin size (Fig. 5). In our experiment, this bin size is determined by the extension of the cloud along the optical axis, which is much larger than the depth of focus of the diffraction limit of the lens system.

Atom noise allows us to characterize the transfer function of our imaging system. Fig. 4 shows the average power spectrum (modulus squared of the spatial Fourier transform) of the optical density images. Because the Fourier transform of uncorrelated fluctuations is flat, the deviation from flatness of the density noise corresponds to blurring induced by the lens, barring the central peak corresponding to the shape of the cloud. For wavevectors q much larger than the resolution limit of the detection scheme, the atom number fluctuations are no longer imaged, and the power spectrum is the photon shot noise. For our experiment this happens for $q < q_F$. Comparison of the power spectra for the cold and the hot cloud shows, at small values of q, a 50% suppression, consistent with the results obtained using spatial bins. If the imaging system still had contrast at $q > 2q_F$, we would expect the ratio of the power spectra to approach unity, since momentum transfer $q > 2q_F$ to a Fermi cloud has negligible Pauli suppression.

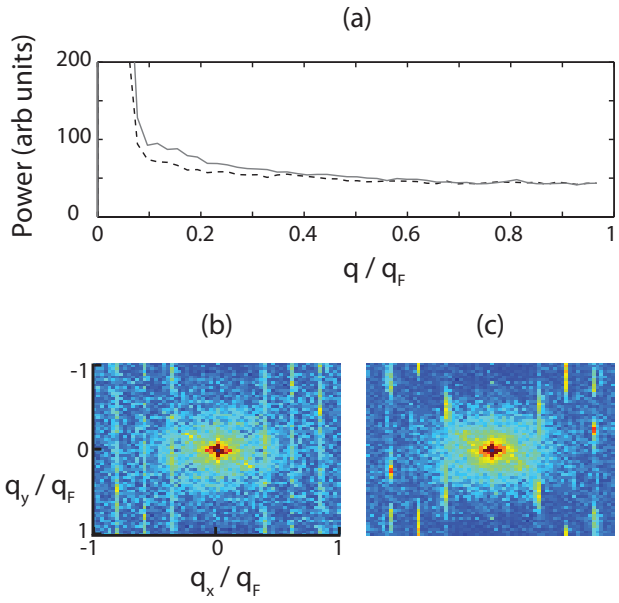

FIG. 4: (a) Radially averaged power spectra of optical density images for hot (solid line) and cold (dashed line) samples (b) Power spectrum of cold sample (arbitrary units) (c) Power spectrum of hot sample (arbitrary units). A constant offset is added to the power spectrum for the hot sample to equalize the levels of photon shot noise.

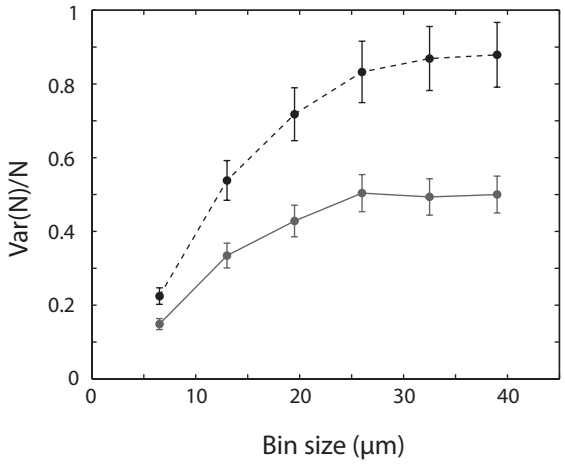

FIG. 5: Observed atom number variance versus bin size for heated (dashed line) and cold (solid line) samples, normalized to 1 for Poissonian statistics. A plateau is reached when the blurring of the bins due to finite optical resolution is negligible.

Appendix F

Speckle Imaging of Spin Fluctuations in a Strongly Interacting Fermi Gas

Speckle Imaging of Spin Fluctuations in a Strongly Interacting Fermi Gas

Christian Sanner, Edward J. Su, Aviv Keshet, Wujie Huang, Jonathon Gillen, Ralf Gommers, and Wolfgang Ketterle

MIT-Harvard Center for Ultracold Atoms, Research Laboratory of Electronics, and Department of Physics, Massachusetts Institute of Technology, Cambridge Massachusetts 02139, USA

(Received 8 October 2010; revised manuscript received 10 December 2010; published 6 January 2011)

Spin fluctuations and density fluctuations are studied for a two-component gas of strongly interacting fermions along the Bose-Einstein condensate-BCS crossover. This is done by *in situ* imaging of dispersive speckle patterns. Compressibility and magnetic susceptibility are determined from the measured fluctuations. This new sensitive method easily resolves a tenfold suppression of spin fluctuations below shot noise due to pairing, and can be applied to novel magnetic phases in optical lattices.

DOI: 10.1103/PhysRevLett.106.010402 PACS numbers: 05.30.Fk, 03.75.Ss, 67.85.Lm

One frontier in the field of ultracold atoms is the realization of quantum systems with strong interactions and strong correlations. Many properties of strongly correlated systems cannot be deduced from mean density distributions. This has drawn interest toward novel ways of probing cold atoms, e.g., via rf spectroscopy [1,2], Bragg and Raman scattering [3], interferometric methods [4,5], and by recording density correlations [6–8]. Further insight into quantum systems is obtained by looking not only at expectation values, but also at fluctuations. Several recent studies looked at density fluctuations, either of bosons around the Mott insulator transition [9–11], or of a gas of noninteracting fermions [12,13].

In this Letter, we extend the study of fluctuations of ultracold gases in several ways. First, we introduce the technique of speckle imaging as a simple and highly sensitive method to characterize fluctuations. Second, we apply it to a two-component Fermi gas across the Bose-Einstein condensate (BEC)-BCS crossover. Third, we directly measure fluctuations in the magnetization, i.e., the difference of the densities in the two different spin components, bypassing the need to measure the individual densities separately.

Our work is motivated by the prospect of realizing wide classes of spin Hamiltonians using a two-component gas of ultracold atoms in an optical lattice [14,15]. An important thermodynamic quantity to characterize two-component systems is the spin susceptibility, which provides a clear signature of phase transitions or crossovers involving the onset of pairing or magnetic order [16–19]. At a ferromagnetic phase transition the susceptibility diverges, whereas in a transition to a paired or antiferromagnetic phase the susceptibility becomes exponentially small in the ratio of the pair binding energy (or antiferromagnetic gap) to the temperature. The fluctuation-dissipation theorem relates response functions to fluctuations, consequently the spin susceptibility can be determined by measuring the fluctuations in the relative density of the two spin components.

In our experiment, we image the atom clouds using light detuned from resonance so that each atom's real polarizability, which contributes to the refractive index, is much larger than its imaginary polarizability, which contributes to absorption. Since the detunings for the two spin states are different, spin fluctuations lead to fluctuations in the local refractive index, resulting in phase shifts of the imaging light that vary randomly in space. We measure these phase shifts by imaging the resulting speckle patterns.

These speckle patterns are created by propagation, which converts the spatially varying phase shifts of the imaging light into an intensity pattern on our detector without the use of a phase plate. Spin and density fluctuations occur on all spatial scales down to the interatomic separation; the smallest observable fluctuations have a wavelength equal to the imaging system's maximum resolution. In our system that length has a Rayleigh range, and hence a depth of field, smaller than the cloud size, so the recorded image is necessarily modified by propagation effects. Propagation mixes up amplitude and phase signals [Fig. 1]. This can be easily seen in the case of a phase grating, which creates an interference pattern further downstream; after propagating for a distance equal to the Rayleigh range of the grating spacing, the imprinted phase is converted into an amplitude pattern. This feature of speckle makes our imaging technique both simple and robust. It is insensitive against defocusing, and allows us to image fluctuations of the real part of the refractive index (i.e., a phase signal) without a phase plate or other Fourier optics.

Similar physics is responsible for laser speckle when a rough surface scatters light with random phases [20], and occurs when a Bose-Einstein condensate with phase fluctuations develops density fluctuations during expansion [21], or when a phase-contrast signal is turned into an amplitude signal by deliberate defocusing [22].

The experiments were performed with typically 10^6 ^{6}Li atoms in each of the two lowest hyperfine states $|1\rangle$ and $|2\rangle$ confined in an optical dipole trap oriented at 45° to the imaging axis with radial and axial trap frequencies $\omega_r = 2\pi \times 108.9(6)\ \mathrm{s}^{-1}$ and $\omega_z = 2\pi \times 7.75(3)\ \mathrm{s}^{-1}$. For the

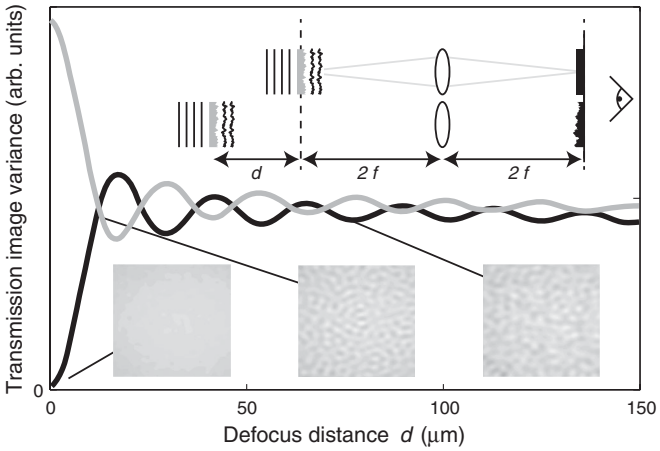

FIG. 1. Simulation of propagation effects after light has passed through a Poissonian phase noise object. Shown are the variance measured in the amplitude or in-phase quadrature (black line) and the out-of-phase quadrature (gray line) as a function of defocus distance, for an imaging system with a numerical aperture of 0.14. Within a distance less than 5% of our cloud size, noise becomes equally distributed between the two quadratures and the variances in transmission and phase-contrast images become the same. (Top inset) For small phase fluctuations, an in-focus phase noise object gives no amplitude contrast, but when it is out of focus it does. (Bottom inset) Sample intensity patterns for a defocused phase object.

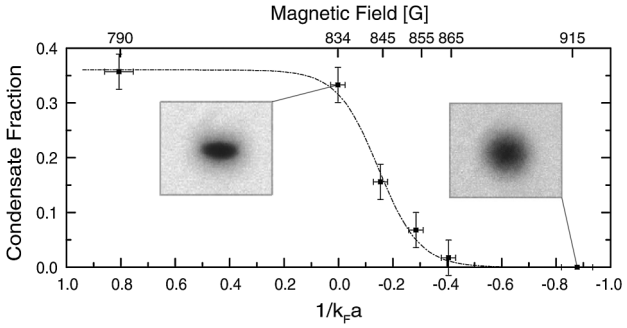

FIG. 2. Measured condensate fraction as a function of dimensionless interaction strength $1/(k_F a)$. Insets show typical images from which the condensate fraction was extracted by fitting a bimodal distribution. The dashed line is a sigmoidal fit to guide the eye.

samples imaged at 527 G, the sample preparation was similar to that described in [13], with a temperature of $0.14(1)T_F$. The samples imaged at other magnetic fields were prepared in a similar fashion, except that evaporation was performed at 1000 G to a final temperature of $T = 0.13(1)T_F$ before ramping the magnetic field over 1.5 s to its final value. The temperature at 1000 G was determined by fitting a noninteracting Thomas-Fermi distribution in time of flight. The temperatures at other points in the crossover were related to that value assuming an isentropic ramp, using calculations presented in [23]. Using this method we obtain temperatures of $0.13(1)T_F$ at 915 G, $0.19(1)T_F$ at 830 G, and $0.19(3)T_F$ at 790 G where additional evaporation was performed to achieve a central optical density similar to that at the other magnetic fields. The extent of the cloud along the imaging direction was 135 μm, much larger than the Rayleigh range of 8 μm for our imaging system with a NA of 0.14.

The superfluid to normal phase boundary was determined by measuring condensate fraction [Fig. 2] using the standard magnetic field sweep technique [24,25]. For this, the magnetic field was rapidly switched to 570 G to transfer atom pairs to more deeply bound pairs (molecules) which survive ballistic expansion. For resonant imaging of the molecules, the field was ramped back to 790 G over 10 ms. The condensate fraction was determined by fitting the one-dimensional density profiles with a bimodal distribution.

As previously described, propagation converts spatial fluctuations in the refractive index into amplitude fluctuations on the detector. For different choices of the probe light frequency, the two atomic spin states will have different real polarizabilities and the local refractive index will be a different linear combination of the (line-of-sight integrated) column densities n_1 and n_2. To measure the susceptibility we choose a probe light frequency exactly between the resonances for states $|1\rangle$ and $|2\rangle$, so that the real polarizabilities are opposite and the refractive index is proportional to the magnetization $(n_1 - n_2)$. The intensity fluctuations on the detector after propagation are consequently proportional to the fluctuations in magnetization. Since a refractive index proportional to $(n_1 + n_2)$ occurs only in the limit of infinite detuning, we measure the fluctuations in the total density by exploiting the fact that the fluctuations in total density can be inferred from the fluctuations in two different linear combinations of n_1 and n_2. For convenience, we obtain the second linear combination using a detuning that has the same value, but opposite sign for state $|2\rangle$, and therefore three times the value for state $|1\rangle$. With this detuning, we record images of the fluctuations in $(n_1/3 + n_2)$.

In principle, this information can be obtained by taking separate absorption images on resonance for states $|1\rangle$ and $|2\rangle$. However, the images would have to be taken on a time scale much faster than that of atomic motion and there would be increased technical noise from the subtraction of large numbers. The use of dispersive imaging has the additional advantage over absorption in that the number of scattered photons in the forward direction is enhanced by superradiance. As a result, for the same amount of heating, a larger number of signal photons can be collected [26]. This is crucial for measuring atomic noise, which requires the collection of several signal photons per atom. The choice of detuning between the transitions of the two states has the important feature that the index of refraction for an equal mixture fluctuates around zero, avoiding any lensing and other distortions of the probe beam. This is not

the case for other choices of detuning, and indeed, we observe some excess noise in those images (see below). At the detunings chosen, 10% residual attenuation is observed, some due to off-resonant absorption, some due to dispersive scattering of light out of the imaging system by small scale density fluctuations. The contribution to the variance of the absorption signal relative to the dispersive signal scales as $(2\Gamma)^2/\delta^2 \approx 0.006$ and can be neglected in the interpretation of the data.

The noise analysis procedure was nearly identical to that performed in [13]. A high-pass filter with a cutoff wavelength of 13 μm was applied to each image of the cloud to minimize the effect of fluctuations in total atom number. Then, for each pixel position, the variance of the optical densities at that position in the different images was computed. After the subtraction of the contribution of photon shot noise, the resulting variance image reflects the noise contribution from the atoms.

The goal of our noise measurements is to determine at various interaction strengths the normalized susceptibility $\tilde{\chi} = \chi/\chi_0$ and compressibility $\tilde{\kappa} = \kappa/\kappa_0$, where $\chi_0 = 3n/2E_F$ and $\kappa_0 = 3/2nE_F$ are the susceptibility and compressibility of a zero-temperature noninteracting Fermi gas with the same total density n and Fermi energy E_F. Before studying spin fluctuations through the BEC-BCS crossover, we therefore calibrate our measurement by measuring the spin fluctuations in a noninteracting mixture, realized at 527 G where the scattering length between the two states vanishes. Figure 3 shows raw profiles of the variances Δ_-^2 and Δ_+^2 measured at the two detunings. These fluctuations in the speckle pattern are proportional to number fluctuations in the specified probe volume V: $\Delta_-^2 = [c\Delta(N_1 - N_2)]^2$ and $\Delta_+^2 = [c'\Delta(N_1/3 + N_2)]^2$. In these relations c and c' are factors which have to be calibrated. Without interactions, N_1 and N_2 are uncorrelated, and one predicts $[\Delta(N_1 - N_2)]^2/[\Delta(N_1/3 + N_2)]^2 = 2/[1 + (1/3)^2] = 1.8$.

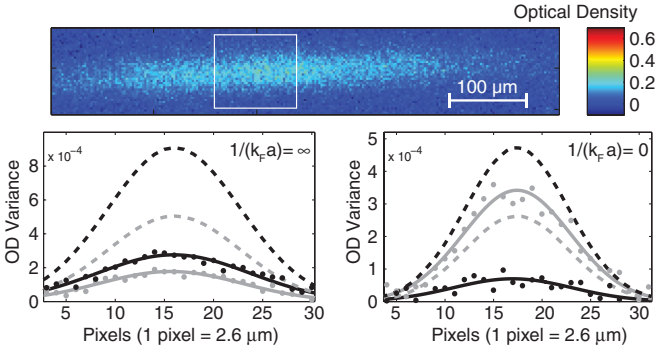

FIG. 3 (color online). (Top panel) Example speckle noise image, with white box indicating analysis region. (Bottom panels) Noise data for noninteracting (left panel) and resonantly interacting (right panel) cold clouds, showing Δ_-^2 (black dots) and Δ_+^2 (gray dots). Solid lines are Gaussian fits to the data, and dotted lines illustrate the expected full Poissonian noise for the corresponding quantities based on density determined from off-resonant absorption.

The observed ratio of $\Delta_-^2/\Delta_+^2 = 1.56(14)$ reflects excess noise contributing to Δ_+^2 due to residual systematic dispersive effects and is accounted for by setting $c'/c = \sqrt{1.8/1.56}$. For high temperatures, the atomic noise of the noninteracting gas approaches shot noise; for lower temperatures we observe a reduction in noise due to Pauli blocking as in our previous work [13]. With our new method, we easily discern spin fluctuations with a variance of less than 10% of atom shot noise.

The fluctuation-dissipation theorem connects the variances $[\Delta(N_1 - N_2)]^2$ and $[\Delta(N_1 + N_2)]^2$ to the susceptibility $\tilde{\chi}$ and the compressibility $\tilde{\kappa}$ via $[\Delta(N_1 - N_2)]^2 = 3N/2(T/T_F)\tilde{\chi}$ and $[\Delta(N_1 + N_2)]^2 = 3N/2(T/T_F)\tilde{\kappa}$ with $N = N_1 + N_2$ and T/T_F being the temperature measured in units of the Fermi temperature T_F. Recomposing the variances from the two experimentally accessible linear combinations these relations become $\Delta_-^2/Nc^2 = 3/2(T/T_F)\tilde{\chi}$ and $9/4\Delta_+^2/Nc'^2 - 1/4\Delta_-^2/Nc^2 = 3/2(T/T_F)\tilde{\kappa}$. The constants c and c' are determined using the noise measurements at 527 G for a noninteracting Fermi gas for which $\tilde{\chi} = \tilde{\kappa} = 1 + O((T/T_F)^2)$. This analysis ignores line-of-sight integration corrections.

Figure 4 shows the spin susceptibility, the compressibility, and the ratio between the two quantities for the interacting mixtures as the interaction strength is varied through the BEC-BCS crossover. The susceptibility and compressibility reproduce the expected qualitative behavior: for the sample at unitarity, where the transition temperature is sufficiently high that a sizable portion of the sample is superfluid, and for the sample on the BEC side, the spin susceptibility is strongly suppressed relative to the compressibility. This reflects the fact that the atoms form bound

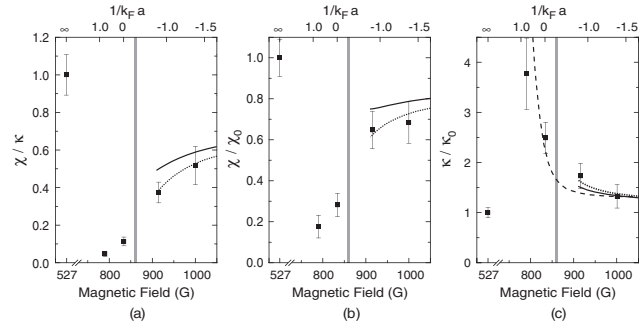

FIG. 4. (a) The ratio χ/κ, (b) the normalized susceptibility χ/χ_0, and (c) the normalized compressibility κ/κ_0 in the BEC-BCS crossover. The variances derived from sequences of images are converted into thermodynamic variables using the measured temperatures and a calibration factor determined from the noninteracting gas. The vertical line indicates the onset region of superfluidity, as determined via condensate fraction measurements. The curves show theoretical zero temperature estimates based on 1st (dotted) and 2nd order (solid) perturbative formulas obtained from Landau's Fermi-liquid theory integrated along the line of sight, and results from a Monte Carlo calculation (dashed) for the compressibility in a homogeneous system [32].

molecules or generalized Cooper pairs; the spin susceptibility should be exponentially small in the binding energy, while the enhanced compressibility reflects the bosonic character of the molecular condensate. At 915 G and 1000 G, where the sample is above the superfluid critical temperature, the susceptibility is larger but still below its value for the noninteracting gas, reflecting the persistence of pair correlations even in the normal phase of the gas.

Above the Feshbach resonance, for attractive interactions, we compare our results to first and second order perturbation theory in the small parameter $k_F a$. This ignores the instability to the superfluid BCS state at exponentially small temperatures. The perturbation theory is formulated for the Landau parameters for a Fermi liquid [16,27]. The susceptibility and compressibility are given by $\chi_0/\chi = (1 + F_0^a)m/m^*$, $\kappa_0/\kappa = (1 + F_0^s)m/m^*$, where $m^* = m(1 + F_1^s/3)$ is the effective mass, and F_l^s, F_l^a are the lth angular momentum symmetric and antisymmetric Landau parameters, respectively. Although the experimental data are taken for relatively strong interactions outside the range of validity for a perturbative description, the predictions still capture the trends observed in the normal phase above the Feshbach resonance. This shows that more accurate measurements of the susceptibility, and a careful study of its temperature dependence, are required to reveal the presence of a possible pseudogap phase.

In our analysis we have neglected quantum fluctuations which are present even at zero temperature [16,28]. They are related to the large-q static structure factor $S(q)$ measured in [29] and proportional to the surface of the probe volume, scaling with $N^{2/3}\log(N)$. For fluctuations of the total density, their relative contribution is roughly $N^{-1/3}/(T/T_F)$, and at most 40% for our experimental parameters. Attractive interactions and pairing suppress both the thermal and quantum spin fluctuations, but it is not known at what temperature quantum fluctuations become essential.

Spin susceptibilities can also be obtained from the equation of state which can be determined by analyzing the average density profiles of imbalanced mixtures [30]. Our method has the advantage of being applicable without imbalance, and requires only local thermal equilibrium. Moreover fluctuations can be compared with susceptibilities determined from the equation of state to perform absolute, model-independent thermometry for strongly interacting systems [31].

In conclusion, we have demonstrated a new technique to determine spin susceptibilities of ultracold atomic gases using speckle imaging. We have validated and calibrated this technique using an ideal Fermi gas and applied it to a strongly interacting Fermi gas in the BEC-BCS crossover. This technique is directly applicable to studying pairing and magnetic ordering of two-component gases in optical lattices.

We acknowledge Qijin Chen and Kathy Levin for providing calculations of condensate fraction, Gregory Astrakharchik and Stefano Giorgini for providing Monte Carlo results for the compressibility, Sandro Stringari and Alessio Recati for discussions, and Yong-il Shin for experimental assistance. This work was supported by NSF and the Office of Naval Research, AFOSR (through the MURI program), and under Army Research Office Grant No. W911NF-07-1-0493 with funds from the DARPA Optical Lattice Emulator program.

[1] S. Gupta *et al.*, Science **300**, 1723 (2003).
[2] C. A. Regal and D. S. Jin, Phys. Rev. Lett. **90**, 230404 (2003).
[3] J. Stenger *et al.*, Phys. Rev. Lett. **82**, 4569 (1999).
[4] T. Kitagawa *et al.*, arXiv:1001.4358.
[5] Z. Hadzibabic, S. Stock, B. Battelier, V. Bretin, and J. Dalibard, Phys. Rev. Lett. **93**, 180403 (2004).
[6] T. Jeltes *et al.*, Nature (London) **445**, 402 (2007).
[7] T. Rom *et al.*, Nature (London) **444**, 733 (2006).
[8] M. Greiner *et al.*, Phys. Rev. Lett. **94**, 110401 (2005).
[9] N. Gemelke *et al.*, Nature (London) **460**, 995 (2009).
[10] W. S. Bakr *et al.*, Science **329**, 547 (2010).
[11] J. F. Sherson *et al.*, Nature (London) **467**, 68 (2010).
[12] T. Müller *et al.*, Phys. Rev. Lett. **105**, 040401 (2010).
[13] C. Sanner *et al.*, Phys. Rev. Lett. **105**, 040402 (2010).
[14] L.-M. Duan, E. Demler, and M. D. Lukin, Phys. Rev. Lett. **91**, 090402 (2003).
[15] A. B. Kuklov and B. V. Svistunov, Phys. Rev. Lett. **90**, 100401 (2003).
[16] A. Recati and S. Stringari, arXiv:1007.4504.
[17] G. M. Bruun *et al.*, Phys. Rev. Lett. **102**, 030401 (2009).
[18] N. Trivedi and M. Randeria, Phys. Rev. Lett. **75**, 312 (1995).
[19] C.-C. Chien and K. Levin, Phys. Rev. A **82**, 013603 (2010).
[20] J. W. Goodman, *Speckle Phenomena in Optics* (Ben Roberts and Company, Greenwood Village, CO, 2007).
[21] D. Hellweg *et al.*, Phys. Rev. Lett. **91**, 010406 (2003).
[22] L. D. Turner *et al.*, Opt. Lett. **29**, 232 (2004).
[23] Q. Chen, J. Stajic, and K. Levin, Phys. Rev. Lett. **95**, 260405 (2005).
[24] M. Greiner *et al.*, Nature (London) **426**, 537 (2003).
[25] M. W. Zwierlein *et al.*, Phys. Rev. Lett. **91**, 250401 (2003).
[26] W. Ketterle, D. S. Durfee, and D. M. Stamper-Kurn, in *Proceedings of the International School of Physics Enrico Fermi, Varenna, 1998* (IOS, Amsterdam, 1999).
[27] E. M. Lifshitz and L. P. Pitaevskii, *Statistical Physics Part 2, 3rd ed.*, Course of Theoretical Physics Vol. 9 (Pergamon Press Inc., Oxford, 1980);
[28] G. E. Astrakharchik, R. Combescot, and L. P. Pitaevskii, Phys. Rev. A **76**, 063616 (2007).
[29] E. D. Kuhnle *et al.*, Phys. Rev. Lett. **105**, 070402 (2010).
[30] C. Salomon (private communication).
[31] D. McKay and B. DeMarco, arXiv:1010.0198.
[32] G. E. Astrakharchik, J. Boronat, J. Casulleras, and S. Giorgini, Phys. Rev. Lett. **93**, 200404 (2004).

Appendix G

Correlations and Pair Formation in a Repulsively Interacting Fermi Gas

Correlations and Pair Formation in a Repulsively Interacting Fermi Gas

Christian Sanner, Edward J. Su, Wujie Huang, Aviv Keshet, Jonathon Gillen, and Wolfgang Ketterle

MIT-Harvard Center for Ultracold Atoms, Research Laboratory of Electronics, and Department of Physics, Massachusetts Institute of Technology, Cambridge, Massachusetts 02139, USA

(Received 9 August 2011; published 13 June 2012)

A degenerate Fermi gas is rapidly quenched into the regime of strong effective repulsion near a Feshbach resonance. The spin fluctuations are monitored using speckle imaging and, contrary to several theoretical predictions, the samples remain in the paramagnetic phase for an arbitrarily large scattering length. Over a wide range of interaction strengths a rapid decay into bound pairs is observed over times on the order of $10\hbar/E_F$, preventing the study of equilibrium phases of strongly repulsive fermions. Our work suggests that a Fermi gas with strong short-range repulsive interactions does not undergo a ferromagnetic phase transition.

DOI: 10.1103/PhysRevLett.108.240404 PACS numbers: 03.75.Ss, 67.85.Lm, 75.10.Lp

Many-body systems can often be modeled using contact interactions, greatly simplifying the analysis while maintaining the essence of the phenomenon to be studied. Such models are almost exactly realized with ultracold gases due to the large ratio of the de Broglie wavelength to the range of the interatomic forces [1]. For itinerant fermions with strong short-range repulsion, textbook calculations predict a ferromagnetic phase transition—the so-called Stoner instability [2].

Here we investigate this system using an ultracold gas of fermionic lithium atoms, and observe that the ferromagnetic phase transition does not occur. A previous experimental study [3] employing a different apparatus found indirect evidence for a ferromagnetic phase, but did not observe the expected domain structure, possibly due to the lack of imaging resolution. Here we address this shortcoming by analyzing density and spin density fluctuations via speckle imaging [4]. When spin domains of m atoms form, the spin density variance will increase by a factor of m [5], even if individual domains are not resolved. One main result of this paper is the absence of such a significant increase which seems to exclude the possibility of a ferromagnetic state in the studied system.

The Stoner model assumes a two-component Fermi gas with a repulsive short-range interaction described by a single parameter, the scattering length. The predicted phase transition to a ferromagnetic state requires large repulsive scattering lengths on the order of the interatomic spacing. They can be realized only by short-range *attractive* potentials with a loosely bound state with binding energy $\hbar^2/(ma^2)$, with m being the atomic mass and a being the scattering length [6]. However, as shown schematically in Fig. 1, the repulsive gas is then by necessity only metastable with respect to decay into the bound state. Many theoretical studies of a Fermi gas with strong short-range repulsive interactions assume that the metastable state is sufficiently long-lived [7–18]. In recent Monte Carlo simulations, the paired state is projected out in the time evolution of the system [19,20]. Theoretical studies concluded that the pairing instability is somewhat faster than the ferromagnetic instability [21]. The second major result of this paper is to show that pair formation occurs indeed on a very short time scale. The measured time constant of $10\hbar/E_F$ (where E_F is the Fermi energy) indicates that the metastable repulsive state will never reach equilibrium and that, even in a metastable sense, a Fermi gas with strong short-range repulsive interactions does not exist. The fast pair formation could not be observed previously due to limited time resolution [3]. Instead, a much slower second phase in the conversion of atoms to pairs was observed leading to the wrong conclusion that the unpaired atoms have a much longer lifetime.

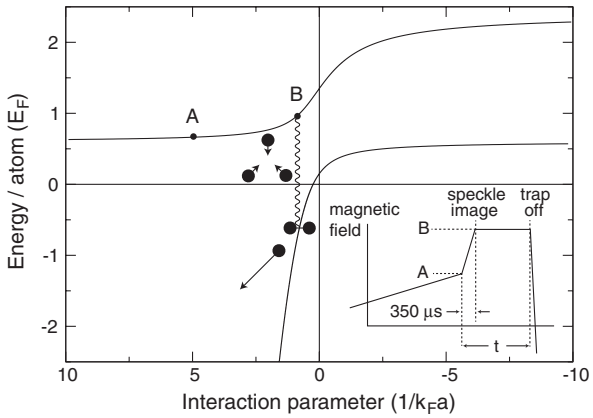

FIG. 1. Diagram showing energy levels and timing of the experiment. The upper (repulsive) and lower (attractive) branch energies, near a Feshbach resonance, are connected by three-body collisions. In our experiment, we quickly jump from a weakly interacting Fermi gas (A) to a strongly interacting one (B) with a rapid magnetic field change. The evolution of correlations and domains and the molecule formation (population of the lower branch) are studied as a function of hold time t. Adapted from [42].

The experiments were carried out with typically 4.2×10^5 ^{6}Li atoms in each of the two lower spin states $|1\rangle$ and $|2\rangle$ confined in an optical dipole trap with radial and axial trap frequencies $\omega_r = 2\pi \times 100(1)$ s^{-1} and $\omega_z = 2\pi \times 9.06(25)$ s^{-1}. The sample was evaporatively cooled at a magnetic bias field $B = 320$ G, identical to the procedure described in [22]. Then the magnetic field was slowly ramped to 730 G ($k_F a = 0.35$) in 500 ms. The fraction of atoms being converted to molecules during the ramp was measured (see below for method) to be below 5%. The temperature of the cloud was typically $0.23(3)T_F$ at 527 G with a Fermi energy of $E_F = k_B T_F = h \times 6.1$ kHz. After rapidly switching the magnetic field from 730 G to the final value in less than 350 μs, spin fluctuations were measured by speckle imaging. Optionally an appropriate rf pulse was applied directly before imaging to rotate the spin orientation along the measurement axis. Due to the use of 20 cm diameter coils outside the vacuum chamber, the inductance of the magnet coils was 330 μH and the fast switching was accomplished by rapidly discharging capacitors charged to 500 V.

Experimentally, spin fluctuations are measured using the technique of speckle imaging described in Ref. [4]. For an appropriate choice of detuning, an incident laser beam experiences a shift of the refractive index proportional to the difference between the local populations of the two spin states N_1 and N_2. Spin fluctuations create spatial fluctuations in the local refractive index and imprint a phase pattern into the incoming light, which is then converted into an amplitude pattern during propagation. The resulting spatial fluctuations in the probe laser intensity are used to determine the spin fluctuations in the sample.

In Ref. [4] we prepared samples on the lower branch of the Feshbach resonance, where positive values of $k_F a$ correspond to a gas of weakly bound molecules. At $k_F a = 1.2$, we observed a sixfold suppression of spin fluctuations and a fourfold enhancement of density fluctuations. Typical fluctuations in the speckle images of a noninteracting Fermi gas at $T = 0.23T_F$ amount to 5% of the average optical signal per pixel, corresponding to about 50% of Poissonian fluctuations. Those fluctuations are modified by factors between 0.2 and 1.6 due to pairing and interactions.

In this study, on the upper branch of the Feshbach resonance, the situation is reversed. For unbound atoms, as the interaction strength increases, the two spin components should develop stronger and stronger anticorrelations and enhanced spin fluctuations. Previous experimental work [3] and several theoretical studies [10,11,13–15,18,23] predicted a phase transition to a ferromagnetic state where the magnetic susceptibility and therefore the spin fluctuations diverge. Recent Monte Carlo simulations [19] predict such a divergence around $k_F a = 0.83$. We therefore expected an increase of spin fluctuations by one or several orders of magnitude, related to the size of magnetic domains.

Figure 2 shows the observed spin fluctuations enhancement compared to the non-interacting cloud at 527 G. The variance enhancement factor reaches its maximum value of 1.6 immediately after the quench, decreasing during the 2 ms afterward. The absence of a dramatic increase shows that no domains form and that the sample remains in the paramagnetic phase throughout. Similar observations were made for a wide range of interaction strengths and wait times. Note that first-order perturbation theory [24] predicts an increase of the susceptibility by a factor of 1.5 at $k_F a = 0.5$ and by a factor of 2 at $kFa = 0.8$ (i.e., no dramatic increase for $k_F a < 1$). Therefore, our data show no evidence for the Fermi gas approaching the Stoner instability.

Before we can fully interpret these findings, we have to take into account the decay of the atomic sample on the upper branch of the Feshbach resonance into bound pairs. We characterize the pair formation by comparing the total number of atoms and molecules $N_a + 2N_{\mathrm{mol}}$ (determined by taking an absorption image after ballistic expansion at high magnetic field where molecules and atoms have the same absorption resonance) to the number of free atoms (determined by rapidly sweeping the magnetic field to 5 G before releasing the atoms and imaging the cloud, converting pairs into deeply bound molecules that are completely shifted out of resonance) [25].

The time evolution of the molecule production (Fig. 3) shows two regimes of distinct behavior. For times less than 1 ms, we observe a considerable number of atoms converted into molecules, while the total number $N_a + 2N_{\mathrm{mol}}$ remains constant. The initial drop in atom number becomes larger as we increase the final magnetic field, and saturates at around 50% near the Feshbach resonance.

We attribute this fast initial decay in atom number to recombination [26,27] into the weakly bound molecular

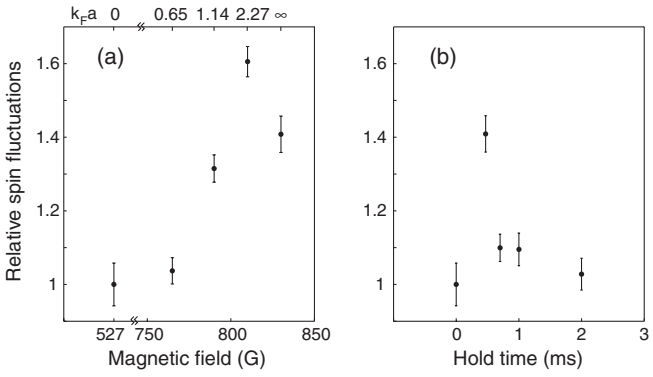

FIG. 2. Spin fluctuations (a) after 350 μs as a function of magnetic field and (b) on resonance as a function of hold time scaled to the value measured at 527 G. Even at strong repulsive interactions, the measured spin fluctuations are barely enhanced, indicating only short-range correlations and no domain formation. The spin fluctuations were determined for square bins of 2.6 μm, each containing on average 1000 atoms per spin state.

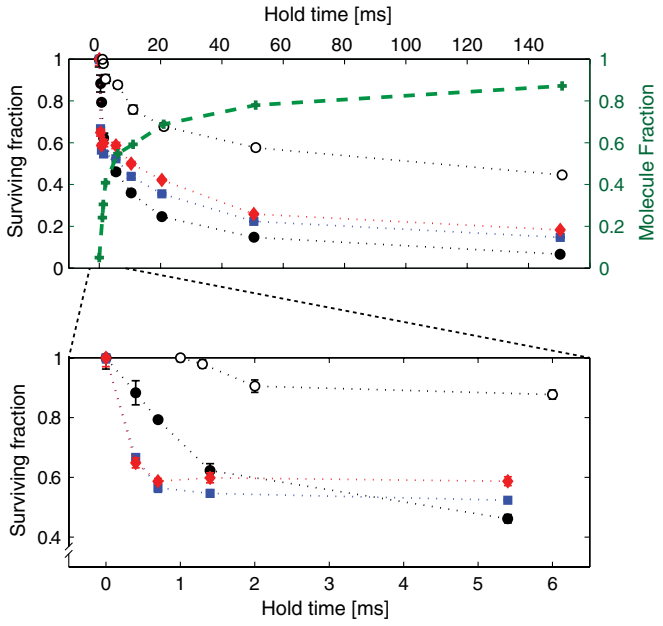

FIG. 3 (color online). Characterization of molecule formation at short and long hold times, and at different values of the interaction strength. The closed symbols, circles (black) at 790 G with $k_F a = 1.14$, squares (blue) at 810 G with $k_F a = 2.27$ and diamonds (red) at 818 G with $k_F a = 3.5$ represent the normalized number of free atoms, the open symbols the total number of atoms including those bound in Feshbach molecules (open circles at 790 G with $k_F a = 1.14$). The crosses (green) show the molecule fraction. The characteristic time scale is set by the Fermi time $\hbar/E_F = 43\ \mu$s, calculated with a cloud averaged Fermi energy.

state. We obtain an atom loss rate $\dot{N}_a/N_a = 250\ \mathrm{s}^{-1}$ at 790 G in the first 1 ms after the magnetic field switch. Assuming a three-body process we estimate the rate coefficient L_3 at this field to be $3.9 \times 10^{-22}\ \mathrm{cm}^6\,\mathrm{s}^{-1}$, though the interaction is already sufficiently strong for many-body effects to be significant. For stronger interactions, about 30% of atom loss occurs already during the relevant 100 μs of ramping through the strongly interacting region, indicating a lower bound of around $3 \times 10^3\ \mathrm{s}^{-1}$ for the loss rate which is 13% of the inverse Fermi time $E_F/\hbar$, calculated with a cloud averaged Fermi energy.

After the first millisecond, the molecule formation rate slows down, by an order of magnitude at a magnetic field of 790 G (and even more dramatically at higher fields) when it reaches about 50%. It seems likely that the molecule fraction has reached a quasi-equilibrium value at the local temperature, which is larger than the initial temperature due to local heating accompanying the molecule formation. Reference [28] presents a simple model for the equilibrium between atoms and molecules (ignoring strong interactions). For phase space densities around unity and close to resonance, the predicted molecule fraction is 0.5, in good agreement with our observations [29].

For longer time scales (hundred milliseconds) we observe a steady increase of the molecule fraction to 90% for the longest hold time. This occurs due to continuous evaporation which cools down the system and shifts the atom-molecule equilibrium towards high molecule fractions. During the same time scale, a slow loss in both atom number and total number is observed caused by inelastic collisions (vibrational relaxation of molecules) and evaporation loss.

Is the rapid conversion into molecules necessarily faster than the evolution of ferromagnetic domains? Our answer is tentatively yes. First, for strong interactions with $k_F a$ around 1, one expects both instabilities (pair formation and Stoner instability) to have rates which scale with the Fermi energy E_F and therefore with $n^{2/3}$. Therefore, one cannot change the competition between the instabilities by working at higher or lower densities. According to Ref. [21] the fastest unstable modes for domain formation have a wave vector $q \approx k_F/2$ and grow at a rate of up to $E_F/4\hbar$ when the cloud is quenched sufficiently far beyond the critical interaction strength. Unstable modes with such wave vectors will develop "domains" of half a wavelength or size $\xi = \pi/q = 2\pi/k_F$ containing 5 atoms per spin state in a volume ξ^3. This rate is comparable to the observed conversion rates into pairs of $0.13E_F$. Therefore, at best, "domains" of a few particles could form, but before they can grow further and prevent the formation of pairs (in a fully polarized state), rapid pair formation takes over and populates the lower branch of the Feshbach resonance. Based on our observations and these arguments, it seems that it is not possible to realize ferromagnetism with strong short range interaction, and therefore the basic Stoner model cannot be realized in nature.

One possibility to suppress pair formation is provided by narrow Feshbach resonances. Here the pairs have dominantly closed channel character and therefore a much smaller overlap matrix element with the free atoms. However, narrow Feshbach resonances are characterized by a long effective range and do not realize the Stoner model which assumes short-range interactions. Other interesting topics for future research on ferromagnetism and pair formation include the effects of dimensionality [30,31], spin imbalance [32,33], mass imbalance [34], lattice and band structure [35,36].

We now discuss whether ferromagnetism is possible *after* atoms and molecules have rapidly established local equilibrium. In other words, starting at $T = 0$, one could heat up the fully paired and superfluid system and create a gas of atomic quasiparticles which are similar to free atoms with repulsive interactions. Density and temperature of the atoms are now coupled. It is likely that such a state is realized in our experiments after a few ms following the quench, until evaporative cooling converts the system into a molecular condensate over ≈ 100 ms. The possibility that such a quasiparticle gas could become ferromagnetic

has not been discussed in the literature. Our experiments do not reveal any major increase in spin fluctuations which seems to exclude a ferromagnetic state. In the simplest picture, we could regard the atomic quasiparticles as free atoms, and then apply the Stoner model to them. Ferromagnetic domain formation is analogous to phase separation between the two spin components [3]. Since dimers interact equally with the two spin components, one might expect that even a noticeable dimer fraction should not suppress the tendency of the atomic gas to form domains. Therefore, in a simple model, one may neglect dimer-atom interactions.

If the Stoner model applies to this quasiparticle gas, the next question is whether the temperature is low enough for the ferromagnetic phase transition. Available theoretical treatments do not predict an exact maximum transition temperature to the ferromagnetic state and obtain an unphysical divergence for large scattering lengths. Since the only energy scale is the Fermi temperature, one would expect a transition temperature which is a fraction of the Fermi temperature [37], higher or around the temperature scale probed in our experiments. However, even above the transition temperature, the susceptibility is enhanced. A simple Weiss mean field or Stoner model leads to the generic form of the susceptibility $\chi(T) = \chi_0(T)/(1 - w\chi_0(T))$, where $\chi_0(T)$ is the Pauli susceptibility of the non-interacting gas and w the interaction parameter. This formula predicts a twofold increase in the susceptibility even 50% above the transition temperature, which is well within the sensitivity of our measurements.

Therefore, our experiment can rule out ferromagnetism for temperatures even slightly lower than the experimental temperatures. Temperatures are very difficult to measure in a transient way for a dynamic system which may not be in full equilibrium. For example, cloud thermometry requires full equilibration and lifetimes much longer than the longest trap period. We attempted to measure the temperature after the hold time near the Feshbach resonance by quickly switching the magnetic field to weak interactions at 527 G and then performing noise thermometry using speckle imaging [4]. We measure column-integrated fluctuations that are 0.61(8) of the Poisson value which implies an effective temperature well below T_F, around 0.33(7) T_F, not much higher than our initial temperature of 0.23 T_F. Although the cloud is not in full equilibrium, an effective local temperature can still be obtained from noise thermometry.

Alternatively, we can estimate the temperature increase from the heat released by pair formation. A simple model [38] accounting for the relevant energy contributions predicts for $k_F a = 1$ that molecule fractions of higher than 20% result in a final temperature above $0.4T_F$, an estimate which is higher than the measurement reported above. One may hope that closer to resonance many-body effects lower the released energy; however, as we show in the Supplemental Material (Fig. 1 of [38]) this is not necessarily the case due to the repulsive interaction energy.

Our experiment has not shown any evidence for a possible ferromagnetic phase in an atomic gas in ''chemical'' equilibrium with dimers. This implies one of the following possibilities. (i) This gas can be described by a simple Hamiltoninan with strong short range repulsion. However, this Hamiltonian does not lead to ferromagnetism. This would be in conflict with the results of recent quantum Monte Carlo simulations [19,20] and second order perturbation theory [11], and in agreement with conclusions based on Tan relations [39]. (ii) The temperature of the gas was too high to observe ferromagnetism. This would then imply a critical temperature around or below $0.2T/T_F$, lower than generally assumed. (iii) The quasiparticles cannot be described by the simple model of an atomic gas with short-range repulsive interactions due to their interactions with the paired fraction.

A previous experiment [3] reported evidence for ferromagnetism by presenting non-monotonic behavior of atom loss rate, kinetic energy and cloud size when approaching the Feshbach resonance, in agreement with predictions based on the Stoner model. Our measurements confirm that the properties of the gas strongly change near $k_F a = 1$. Similar to [3], we observe features in kinetic and release energy measurements near the resonance (see Supplemental Material [38]). However, the behavior is more complex than that captured by simple models. The atomic fraction decays non-exponentially (see Fig. 3), and therefore an extracted decay time will depend on the details of the measurement such as time resolution. Reference [3] found a maximum of the loss rate of 200 s^{-1} for a Fermi energy of 28 kHz. Our lower bound of the decay rate of 3×10^3 s^{-1} is 15 times faster at a five times smaller Fermi energy. Our more detailed study rules out that Ref. [3] has observed ferromagnetic behavior.

Our conclusion is that an ultracold gas with strong short range repulsive interactions near a Feshbach resonance remains in the paramagnetic phase. The fast formation of molecules and the accompanying heating makes it impossible to study such a gas in equilibrium, confirming predictions of a rapid conversion of the atomic gas to pairs [21,40]. The Stoner criterion for ferromagnetism obtains when the effective interaction strength times the density of states is larger than one. This is a at least an approximately valid criterion for multi-band lattice models [41]. We have shown here that this criterion cannot be applied to Fermi gases with short-range repulsive interactions (the basic Stoner model) since the neglected competition with pairing is crucial.

This work was supported by NSF and ONR, AFOSR MURI, and under ARO Grant No. W911NF-07-1-0493 with funds from the DARPA Optical Lattice Emulator

program. We are thankful to Eugene Demler, David Pekker, Boris Svistunov, Nikolay Prokof'ev, and Wilhelm Zwerger for valuable discussions and to David Weld for critical reading of the manuscript.

[1] W. Ketterle and M. W. Zwierlein, in *Proceedings of the International School of Physics "Enrico Fermi,"* Course CLXIV (IOS, Amsterdam, 2007).
[2] D. W. Snoke, *Solid State Physics: Essential Concepts* (Addison-Wesley, San Francisco, 2008).
[3] G.-B. Jo, Y.-R. Lee, J.-H. Choi, C. A. Christensen, T. H. Kim, J. H. Thywissen, D. E. Pritchard, and W. Ketterle, Science **325**, 1521 (2009).
[4] C. Sanner, E. J. Su, A. Keshet, W. Huang, J. Gillen, R. Gommers, and W. Ketterle, Phys. Rev. Lett. **106**, 010402 (2011).
[5] This is illustrated by a simplified model assuming Poissonian fluctuations in a given probe volume within the atom sample. With on average N atoms in this volume, one would measure a standard deviation in the atom number of $\sqrt{N}$. However, if the atoms formed clusters each made of m atoms, the standard deviation of the number of clusters would be $\sqrt{N/m}$, leading to a variance in atom number of $(m\sqrt{N/m})^2 = mN$.
[6] Potentials with a positive scattering length a have no bound state only if the effective range r_e is larger than $a/2$. Otherwise, the s-wave scattering amplitude $f(k) = 1/(-1/a + r_e k^2/2 - ik)$ has a pole on the imaginary axis corresponding to a bound state.
[7] M. Houbiers, R. Ferwerda, H. T. C. Stoof, W. I. McAlexander, C. A. Sackett, and R. G. Hulet, Phys. Rev. A **56**, 4864 (1997).
[8] M. Amoruso, I. Meccoli, A. Minguzzi, and M. P. Tosi, Eur. Phys. J. D **7**, 441 (1999).
[9] L. Salasnich, B. Pozzi, A. Parola, and L. Reatto, J. Phys. B **33**, 3943 (2000).
[10] T. Sogo and H. Yabu, Phys. Rev. A **66**, 043611 (2002).
[11] R. A. Duine and A. H. MacDonald, Phys. Rev. Lett. **95**, 230403 (2005).
[12] H. Zhai, Phys. Rev. A **80**, 051605 (2009).
[13] G. J. Conduit and B. D. Simons, Phys. Rev. Lett. **103**, 200403 (2009).
[14] L. J. LeBlanc, J. H. Thywissen, A. A. Burkov, and A. Paramekanti, Phys. Rev. A **80**, 013607 (2009).
[15] I. Berdnikov, P. Coleman, and S. H. Simon, Phys. Rev. B **79**, 224403 (2009).
[16] X. Cui and H. Zhai, Phys. Rev. A **81**, 041602 (2010).
[17] S. Zhang, H. Hung, and C. Wu, Phys. Rev. A **82**, 053618 (2010).
[18] H. Heiselberg, Phys. Rev. A **83**, 053635 (2011).
[19] S. Pilati, G. Bertaina, S. Giorgini, and M. Troyer, Phys. Rev. Lett. **105**, 030405 (2010).
[20] S.-Y. Chang, M. Randeria, and N. Trivedi, Proc. Natl. Acad. Sci. U.S.A. **108**, 51 (2010).
[21] D. Pekker, M. Babadi, R. Sensarma, N. Zinner, L. Pollet, M. W. Zwierlein, and E. Demler, Phys. Rev. Lett. **106**, 050402 (2011).
[22] C. Sanner, E. J. Su, A. Keshet, R. Gommers, Y. Shin, W. Huang, and W. Ketterle, Phys. Rev. Lett. **105**, 040402 (2010).
[23] M. Sandri, A. Minguzzi, and F. Toigo, Europhys. Lett. **96**, 66 004 (2011).
[24] A. Recati and S. Stringari, Phys. Rev. Lett. **106**, 080402 (2011).
[25] S. Jochim, M. Bartenstein, A. Altmeyer, G. Hendl, C. Chin, J. Hecker Denschlag, and R. Grimm, Phys. Rev. Lett. **91**, 240402 (2003).
[26] C. Chin, R. Grimm, P. Julienne, and E. Tiesinga, Rev. Mod. Phys. **82**, 1225 (2010).
[27] G. J. Conduit and E. Altman, Phys. Rev. A **83**, 043618 (2011).
[28] C. Chin and R. Grimm, Phys. Rev. A **69**, 033612 (2004).
[29] Note that the drop in molecule formation after 1 ms cannot be explained by the drop in atomic density by a factor of 2 due to conversion into molecules and to an increase in the size of the sample due to the increased repulsive interactions.
[30] N. D. Drummond, N. R. Cooper, R. J. Needs, and G. V. Shlyapnikov, Phys. Rev. B **83**, 195429 (2011).
[31] V. Pietilä, D. Pekker, Y. Nishida, and E. Demler, Phys. Rev. A **85**, 023621 (2012).
[32] X.-J. Liu and H. Hu, Phys. Rev. A **82**, 043626 (2010).
[33] H. Dong, H. Hu, X.-J. Liu, and P. D. Drummond, Phys. Rev. A **82**, 013627 (2010).
[34] C. W. von Keyserlingk and G. J. Conduit, Phys. Rev. A **83**, 053625 (2011).
[35] C.-C. Chang, S. Zhang, and D. M. Ceperley, Phys. Rev. A **82**, 061603 (2010).
[36] G. Carleo, S. Moroni, F. Becca, and S. Baroni, Phys. Rev. B **83**, 060411 (2011).
[37] X.-J. Liu, H. Hu, and P. D. Drummond, Phys. Rev. A **82**, 023619 (2010).
[38] See Supplemental Material at http://link.aps.org/supplemental/10.1103/PhysRevLett.108.240404 for a discussion of cloud release energy and heating due to molecule formation.
[39] M. Barth and W. Zwerger, Ann. Phys. (N.Y.) **326**, 2544 (2011).
[40] S. Zhang and T.-L. Ho, New J. Phys. **13**, 055003 (2011).
[41] J. Bünemann, W. Weber, and F. Gebhard, Phys. Rev. B **57**, 6896 (1998).
[42] L. Pricoupenko and Y. Castin, Phys. Rev. A **69**, 051601 (2004).

Appendix H

Speckle Simulation

```
%%% Speckle simulation class, and static simulation functions.
%%% Figure generation made use of VarianceVsDefocus and
%%% VarianceVsDefocusPhasecontrast routines.

classdef ImageMatrix < handle
    properties
        dataMatrix
        fourierDataMatrix
        nPixels
        delta
        deltav
        transmissionMatrix
        illuminationMatrix
        atPerPixel
    end

    methods(Static)

        function [variance densityfactor]= VarianceVsDensity
            for i=0:100
                a=ImageMatrix.OutOfFocusNoiseSimulation(2048, 50, i);
                a.MakeTransmissionMatrix();
                temp = a.transmissionMatrix(800:1200, 800:1200);
                variance(i+1) = var(temp(:));
                densityfactor(i+1)=i/5;
                i
            end
        end

        function [variance defocus] = VarianceVsDefocus
            for i=0:1500
                a=ImageMatrix.OutOfFocusNoiseSimulation(2048, i*.1, 1);
                a.MakeTransmissionMatrix();
                temp = a.transmissionMatrix(800:1200, 800:1200);
                variance(i+1) = var(temp(:));
                defocus(i+1)=i*.1;
                i
            end
        end

        function [variance defocus] = VarianceVsDefocusPhasecontrast
            for i=0:1500
                a=ImageMatrix.OutOfFocusNoiseSimulation(2048, i*.1, []);
                a.AddPhaseSpot();
                a.InverseFourierTransform();
                a.MakeTransmissionMatrix();
                temp = a.transmissionMatrix(800:1200, 800:1200);
                variance(i+1) = var(temp(:));
                defocus(i+1)=i*.1;
                i
            end
        end

        function [variance nplanes] = VarianceVsNplanes

            for (i=1:15)
                for (j=1:10)
                    a=ImageMatrix.MultiPlaneNoiseSimulation(2048, i, []);
                    a.MakeTransmissionMatrix();
                    temp = a.transmissionMatrix(800:1200, 800:1200);
                    variance(i) = variance(i) + var(temp(:))/10;
                    nplanes(i)=i;
                    i
                    j
                end
            end
        end
```

```
function output = MultiPlaneNoiseSimulation (nnn,nPlanes, dPerPlane)
    if (isempty(nPlanes))
        nPlanes = 10;
    end

    if (isempty(dPerPlane))
        dPerPlane=10;
    end

    a=ImageMatrix;
    a.InitGaussianMatrix(0, nnn, []);
    atomsPerSquareMicron = 44.4444;
    atomsPerPixel = atomsPerSquareMicron * (a.delta^2);
    areaPhasePerAtom = 0.27;
    phaseDegPerAtom = areaPhasePerAtom / (a.delta^2);

    for i=1:nPlanes

        a.AddNoiseToMatrix(atomsPerPixel/nPlanes, phaseDegPerAtom, a.nPixels/8);
        a.FourierTransform;
        a.Propagate(dPerPlane);
        a.InverseFourierTransform;

    end

    a.LowPassFilter(.25);
    a.InverseFourierTransform;

    output=a;
end

function output=OutOfFocusNoiseSimulation(nnn, defocus, densityFactor)
    if (isempty(defocus))
        defocus=10
    end

    if (isempty(densityFactor))
        densityFactor=1;
    end

    a=ImageMatrix;
    a.InitGaussianMatrix(0, nnn, []);
    atomsPerSquareMicron = 44.4444 * densityFactor;
    atomsPerPixel = atomsPerSquareMicron * (a.delta^2);
    a.atPerPixel = atomsPerPixel;
    areaPhasePerAtom = 0.27;
    phaseDegPerAtom = areaPhasePerAtom / (a.delta^2);
    a.AddNoiseToMatrix(atomsPerPixel, phaseDegPerAtom, a.nPixels/8);
    a.FourierTransform;
    a.Propagate(defocus);
    a.LowPassFilter(.25);
    a.InverseFourierTransform;
    %    a.PlotImage;
    %    a.delta

    output=a;
end

function [varData meanData]=VerticalStack(nnn, nShots)
    allData(1:nShots, 1:nnn, 1:nnn)=0;

    for i=1:nShots
        allData(i,:,:)=abs(ImageMatrix.OutOfFocusNoiseSimulation(nnn)).^2;
        i
    end

    varData=squeeze(var(allData));
    meanData=squeeze(mean(allData));
```

```
        end
    end



    methods

        function MakeTransmissionMatrix(obj)
            obj.transmissionMatrix=(abs(obj.dataMatrix).^2)./obj.illuminationMatrix;
        end

        function InitGaussianMatrix(obj, zref, nnn, field)

            if (isempty(nnn))
                nnn=4096;
            end

            if (isempty(field))
                field=614.4;
            end

            if (isempty(zref))
                zref=0;
            end

            obj.delta = field/nnn;
            obj.nPixels = nnn;

            s1=num2str(zref);
            s2=num2str(nnn);
            s3=num2str(field);
            cache_filename = strcat('gausscache', s1,s2,s3,'.mat');

            if (exist(cache_filename, 'file'))
                disp('loading initial gaussian matrix from cached file');
                load(cache_filename);
                obj.dataMatrix = gcache;
                obj.illuminationMatrix=abs(obj.dataMatrix.^2);
                return
            end

            disp('synthesizing initial gaussian matrix (will be saved to cache file)');

            obj.delta = field / obj.nPixels;

            [pp,qq]=meshgrid(-nnn/2:nnn/2-1);

            xx=obj.delta*pp;
            yy=obj.delta*qq;
            zz=zref*ones(nnn);

            obj.dataMatrix=gaussian(xx,yy,zz,[],[],[]);
            obj.illuminationMatrix=abs(obj.dataMatrix.^2);
            gcache = obj.dataMatrix;
            save(cache_filename, 'gcache');
        end

        function AddNoiseToMatrix(obj, atomsPerPixel, phaseDegreesPerAtom, halfBoxSize)
            boxSize = 2 * halfBoxSize + 1;
            randn('state', sum(100*clock));

            randPhases      = exp(((2*pi*1i*phaseDegreesPerAtom/360)*(poissrnd↵
(atomsPerPixel,boxSize,boxSize)-poissrnd(atomsPerPixel,boxSize,boxSize))));

            indexRange = (obj.nPixels/2+1-halfBoxSize):(obj.nPixels/2+1+halfBoxSize);
            obj.dataMatrix(indexRange, indexRange) = obj.dataMatrix(indexRange,↵
indexRange) .* randPhases;
```

```
        end

        function PlotImage(obj)
            colormap(gray);
            imagesc(abs(obj.dataMatrix).^2);
        end

        function PlotSpectrum(obj)
            imagesc(abs(obj.fourierDataMatrix));
        end

        function FourierTransform(obj)
            [mm1,nn2]=ndgrid(1:obj.nPixels,1:obj.nPixels);
            signmatrix=(-1).^(mm1+nn2);
            fouriermatrix1=obj.delta^2*obj.nPixels^2*ifft2(obj.dataMatrix').*signmatrix;
            %fourierpixelmatrix=fouriermatrix1';

            clear trandposedDataMatrix mm1 nn2 signmatrix;

            %output1=[fourierpixelmatrix,fourierpixelmatrix;fourierpixelmatrix,
fourierpixelmatrix];

            nnn=obj.nPixels;
            %obj.fourierDataMatrix=output1(nnn/2+1:nnn/2+nnn,nnn/2+1:nnn/2+nnn);
            obj.fourierDataMatrix = circshift(fouriermatrix1', [nnn/2, nnn/2]);
        end

        function Propagate(obj,propdist)

            nnn=obj.nPixels;

            [xxmatrix,yymatrix]=meshgrid(-nnn/2:nnn/2-1);
            deltav=1/(nnn*obj.delta);
            vxx=deltav*xxmatrix;
            vyy=deltav*yymatrix;
            clear xxmatrix yymatrix;

            lambda=671/1000;


            radicand=ones(nnn)*1/(lambda^2)-vxx.^2-vyy.^2;
            clear vxx vyy;

            c1matrix=(radicand<0);
            c2matrix=(c1matrix<0.5);
            c3matrix=-c1matrix+c2matrix;
            c3matrix=double(c3matrix);
            hmatrix=exp(-1i*2*pi*propdist*sqrt(radicand).*c3matrix);
            clear c1matrix c2matrix c3matrix radicand;

            obj.fourierDataMatrix=hmatrix.*obj.fourierDataMatrix;
        end

        function InverseFourierTransform(obj)
            nnn=obj.nPixels;
            deltav=1/(nnn*obj.delta);

            [mm1,nn2]=ndgrid(1:nnn,1:nnn);
            signmatrix=(-1).^(mm1+nn2);
            clear mm1 nn2;

            fourierout=deltav^2*signmatrix.*fft2(obj.fourierDataMatrix');
            clear signmatrix;



            %output1=[outputpixelmatrix,outputpixelmatrix;outputpixelmatrix,
outputpixelmatrix];
```

```
            %obj.dataMatrix=output1(nnn/2+1:nnn/2+nnn,nnn/2+1:nnn/2+nnn);

            obj.dataMatrix = circshift(fourierout', [nnn/2, nnn/2]);

        end

        function LowPassFilter(obj, vmax)
            if (isempty(vmax))
                vmax=0.25;
            end

            nnn=obj.nPixels;
            delta=obj.delta;

            [xxmatrix,yymatrix]=meshgrid(-nnn/2:nnn/2-1);
            deltav=1/(nnn*delta); %pixelsize deltavx and deltavy
            obj.deltav=deltav
            vxx=deltav*xxmatrix;
            vyy=deltav*yymatrix;

            passmatrix=(vxx.^2+vyy.^2)<=vmax^2;

            obj.fourierDataMatrix=passmatrix.*obj.fourierDataMatrix;
        end

        function AddPhaseSpot(obj)
            nnn=obj.nPixels;
            [xxmatrix,yymatrix]=meshgrid(-nnn/2:nnn/2-1);
            deltav=1/(nnn*obj.delta); %pixelsize deltavx and deltavy
            vxx=deltav*xxmatrix;
            vyy=deltav*yymatrix;
            prehh1=vxx.^2+vyy.^2;
            prehh3=(prehh1<=0.003^2);

            obj.fourierDataMatrix(prehh3) = obj.fourierDataMatrix(prehh3).*1i;


        end

        function HighPassFilter(obj, vmin)
            if (isempty(vmin))
                vmin=.0025;
            end

            nnn=obj.nPixels;
            delta=obj.delta;

            [xxmatrix,yymatrix]=meshgrid(-nnn/2:nnn/2-1);
            deltav=1/(nnn*delta); %pixelsize deltavx and deltavy
            vxx=deltav*xxmatrix;
            vyy=deltav*yymatrix;

            passmatrix=(vxx.^2+vyy.^2)>=vmin^2;

            obj.fourierDataMatrix=passmatrix.*obj.fourierDataMatrix;
        end


    end
end


%%% Gaussian Generation Helper Functions

function output=gaussian(x,y,z, waist, lamb, a0)
    global w0 z0

    if (isempty(waist))
```

```
        waist = 200;
    end

    if (isempty(lamb))
        lamb = 671/1000;
    end

    if (isempty(a0))
        a0 = 1;
    end

    w0 = waist;
    z0 = w0^2*pi/lamb;
    k = 2*pi/lamb;

    if z(1,1)==0
        output = a0*w0./w(z).*exp(-(x.^2 + y.^2)./w(z).^2).*exp(-1i*k*z + 1i*zet(z));
    else
        output = a0*w0./w(z).*exp(-(x.^2 + y.^2)./w(z).^2).*exp(-1i*k*z - 1i*k*(x.^2 +
y.^2)./(2*r(z)) + 1i*zet(z));
    end
end


function outw=w(zzz)
    global w0 z0
    outw = w0*sqrt(1 + (zzz/z0).^2);
end

function outr=r(zzz)
    global z0
    outr = zzz.*(1 + (z0./zzz).^2);
end

function outzet=zet(zzz)
    global z0
    outzet = atan(zzz/z0);
end
```

Appendix I

Band Insulator Optimization

In[49]:=
```
Needs["PlotLegends`"]
```

Constants

In[50]:=
```
λ = 1064.0*^-9;
λ0 = 671.0*^-9;
c = 3.0*^8;
h = 6.626*^-34;
ħ = h / (2 π);
m = 9.96*^-27;
ωL = (2 π) c / λ;
ω0 = (2 π) c / λ0;
Γ = (2 π) * 5.87*^6;
kL = (2 π) / λ;
Er = ħ^2 kL^2 / (2 m);
```

In[61]:=
```
(*Recoil energy sanity check, lithium recoil for 1064 nm is ~29 kHz*)
Er / h
```

Out[61]= 29 381.8

Formulas

In[62]:=
```
Udip[II_] := -3 π c^2 / (2 ω0^3) Γ (1 / (ω0 - ωL) + 1 / (ω0 + ωL)) II; (* From Grimm et all '99*)
```

In[63]:=
```
ωa[U0_] := 2 Sqrt[Er Abs[U0]] / ħ; (*From Bloch/Dalibard/Zwerger Rev Mod Phys*)
J[U0_] := 4 / Sqrt[π] Er (Abs[U0] / Er)^(3/4) Exp[-2 (Abs[U0] / Er)^(1/2)];
(*From Bloch/Dalibard/Zwerger Rev Mod Phys, approximate for deep lattices*)
(*In both expressions U0 is the full absolute height*)
```

In[65]:=

In[66]:=
```
W[U0_] = 4 J[U0]; (*Width of band, from Bloch/Dalibard/Zwerger*)
```

Plots -- Basic Lattice Properties

In[67]:=
```
p1 = Plot[ωa[u * Er], {u, 0, 20}, PlotLabel → "Lattice site trap frequency",
  AxesLabel → {"Lattice Depth / Er", "Trap frequency (rad/s)"}]
```

Out[67]=

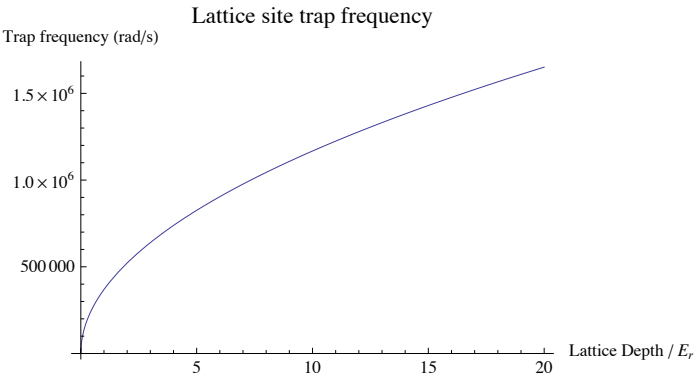

In[68]:=
```
p2 = Plot[W[u * Er] / ħ, {u, 0, 20}, PlotLabel → "Width of First Band",
  AxesLabel → {"Lattice Depth / Er", "First band width (rad/s)"}]
```

Out[68]=

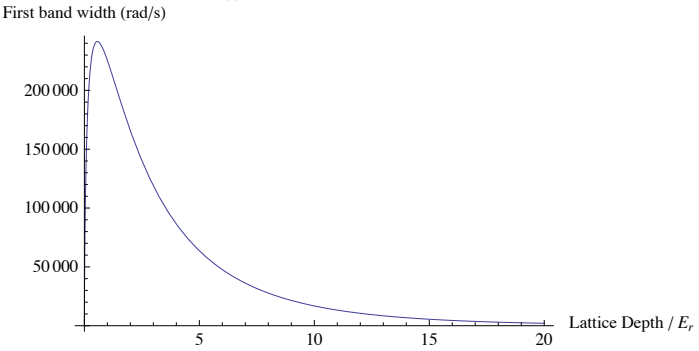

In[69]:=
```
p3 = Plot[(W[u * Er] / ħ) / ωa[u * Er], {u, 0, 20},
  PlotRange → All, PlotLabel → "Bandwidth / Band Spacing",
  AxesLabel → {"Lattice Depth / Er", "Dimensionless"}]
```

Out[69]=

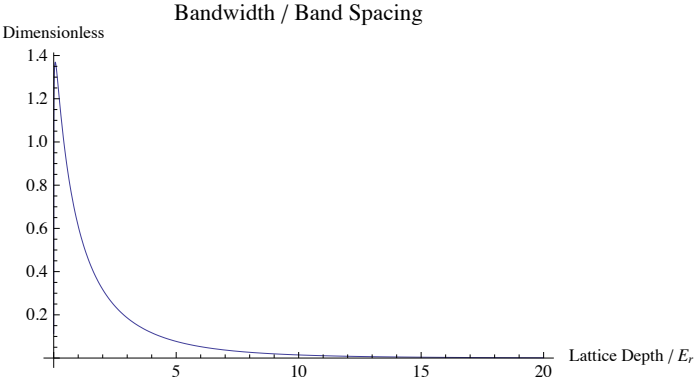

Trapping potential from beam power

In[70]:=
```
I0FromPower[P_, w_] := 2 * P / (π w^2);

RadialOnlyGaussianBeamIntensity[r_, P_, w_] := I0FromPower[P, w] Exp[-2 r^2 / w^2];

(* From http://en.wikipedia.org/wiki/Gaussian_beam *)

TrapFrequency[U0_, w_] := (4 Abs[U0] / (m w^2))^(1/2)

(*From Grimm et all '99*)
```

In[73]:=
```
Plot[U_dip[RadialOnlyGaussianBeamIntensity[rad * 10^-6, 5, 50*^-6]] / ħ, {rad, -200, 200},
 PlotLabel → "Radial profile of gaussian potential for 5 Watt 50 micron single beam",
 AxesLabel → {"Radial position (μm)", "Potential depth (rad/s)"}]
```

Out[73]=

Radial profile of gaussian potential for 5 Watt 50 micron single beam

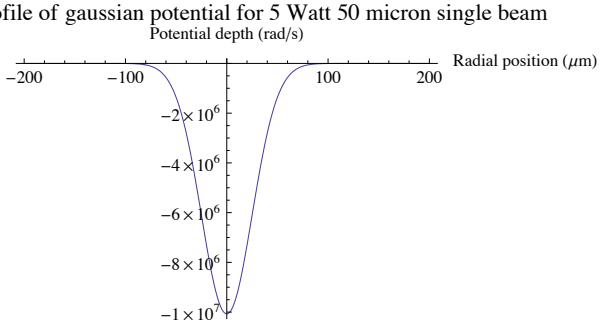

In[74]:=
```
(*Sanity check, ~2kHz for a 5W beam focused to a 50 micron waist seems about right*)
TrapFrequency[U_dip[I0FromPower[5, 50*^-6]], 50*^-6] / (2 π)
```

Out[74]= 2078.79

In[75]:=
```
4 * U_dip[I0FromPower[5, 100*^-6]] / E_r
```

Out[75]= -54.5492

Band Insulator Region Size -- Sandbox

In[76]:=
```
(*Consider a lattice in 1D, inside of an overall trap provided by the confining
 potential of the other two directions of lattice beam. In this situation,
it so happens that the effective "confining potential" provided
 by the other two beams is the same as the lattice depth.*)
```

In[77]:=
```
TestLatticeParameters = {P → 1, w → 200*^-6};
LatticeDepth[r_, P_, w_] := 4 * U_dip[RadialOnlyGaussianBeamIntensity[r, P, w]];
```

In[79]:=

In[80]:=
```
Plot[LatticeDepth[rad * 10^-6, P, w] / Eᵣ /. TestLatticeParameters, {rad, 0, 200}]
```

Out[80]=

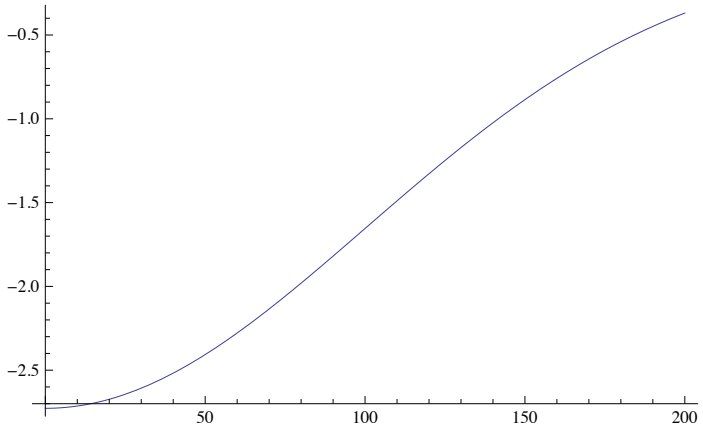

In[81]:=
```
Plot[{ħ ωₐ[LatticeDepth[rad * 10^-6, P, w]],
    LatticeDepth[rad * 10^-6, P, w] - LatticeDepth[0, P, w],
    W[LatticeDepth[rad * 10^-6, P, w]]} / h /. TestLatticeParameters, {rad, 0, 1000}]
```

Out[81]=

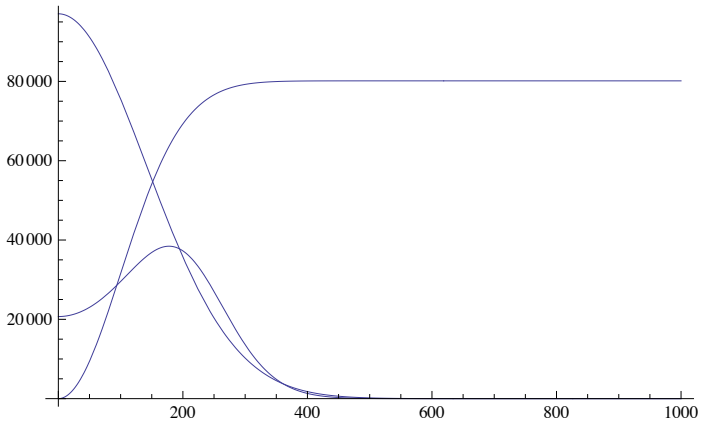

Band Insulator Region -- Plots

In[84]:=
```
BIRadiusSolution = Solve[{LatticeDepth[rad, P, w * 10^-6] - LatticeDepth[0, P, w * 10^-6] ==
      ħ ωₐ[LatticeDepth[0, P, w * 10^-6]], rad > 0}, {rad}, Reals][[1]];
```

In[85]:=
```
ContourPlot[(rad * 10^6) /. BIRadiusSolution,
  {P, 0, 5}, {w, 1, 200}, ContourLabels → True,
  RegionFunction → Function[{P, w}, -LatticeDepth[0, P, w * 10^-6] > 8 Eᵣ],
  BoundaryStyle → Automatic, Contours → Range[10] * 20, PlotLabel ->
   "Radius of maximally filled band insulator (in μm) in an isotropic 3D Lattice",
  FrameLabel → {"Power per lattice beam (W)", "Waist size per lattice beam (μm)"},
  ImageSize → Large];
```

In[86]:=
```
ContourPlot[(4/3 π rad^3) * 10^12 /. BIRadiusSolution,
  {P, 0, 5}, {w, 1, 200}, ContourLabels → True,
  RegionFunction → Function[{P, w}, -LatticeDepth[0, P, w * 10^-6] > 8 Eᵣ],
  BoundaryStyle → Automatic, PlotRange → {0, 10 000 000}, Contours → Range[20], PlotLabel →
   "Number of band insulator region atoms (in millions) in an isotropic 3D Lattice",
  FrameLabel → {"Power per lattice beam (W)", "Waist size per lattice beam (μm)"},
  ImageSize → Large];
```

Bibliography

[1] E Altman, E Demler, and M Lukin. Probing many-body states of ultracold atoms via noise correlations. *Physical Review A*, 70(013603), 2004.

[2] M H Anderson, J R Ensher, M R Matthews, C E Wieman, and E A Cornell. Observation of Bose-Einstein Condensation in a Dilute Atomic Vapor. *Science*, 269(5221):198–201, January 1995.

[3] M. R. Andrews, M.-O. Mewes, N. J. van Druten, D S Durfee, D. M. Kurn, and W Ketterle. Direct, Nondestructive Observation of a Bose Condensate. *Science*, 273(5271):84–87, January 1996.

[4] G E Astrakharchik, J Boronat, J Casulleras, and S Giorgini. Equation of State of a Fermi Gas in the BEC-BCS Crossover: A Quantum Monte Carlo Study. *Physical review letters*, 93(20):200404 EP –, January 2004.

[5] W Bakr, J Gillen, A Peng, S Fölling, and M Greiner. A quantum gas microscope for detecting single atoms in a Hubbard-regime optical lattice. *Nature*, 462:74–77, 2009.

[6] J G Bednorz and K A Müller. Possible high T_c superconductivity in the BaLaCuO system. *Zeitschrift für Physik B Condensed Matter*, 64(2):189–193, January 1986.

[7] C Benvenuti, P Chiggiato, P Costa Pinto, and A Escudeiro. Vacuum properties of TiZrV non-evaporable getter films. *Vacuum*, 60:57–65, 2001.

[8] R Hanbury Brown and R Q Twiss. Correlation between Photons in two Coherent Beams of Light. *Nature*, 177(4497):27–29, January 1956.

[9] G Campbell, J Mun, M Boyd, P Medley, and A Leanhardt. Imaging the Mott insulator shells by using atomic clock shifts. *Science*, 313(649), 2006.

[10] Robert Campbell, Robert Smith, Naaman Tammuz, Scott Beattie, Stuart Moulder, and Zoran Hadzibabic. Efficient production of large ^{39}K Bose-Einstein condensates. *Physical Review A*, 82(6), December 2010.

[11] Yu-Ao Chen. Controlling Correlated Tunneling and Superexchange Interactions with ac-Driven Optical Lattices. *Physical review letters*, 107(21):210405 EP –, January 2011.

[12] P Chiggiato and C Pinto. Ti-Zr-V non-evaporable getter films: from development to large scale production for the Large Hadron Collider. *Thin Solid Films*, 515:382–388, 2006.

[13] Ananth P. Chikkatur. *Colliding and Moving Bose-Einstein Condensates: Studies of superfluidity and optical tweezers for condensate transport*. PhD thesis, MIT, October 2002.

[14] J. K. Chin, D. E. Miller, Y Liu, C Stan, W Setiawan, C Sanner, K Xu, and W Ketterle. Evidence for superfluidity of ultracold fermions in an optical lattice. *Nature*, 443(7114):961–964.

[15] Jit Kee Chin. *Strongly-interacting Fermions in an Optical Lattice*. PhD thesis, MIT, August 2007.

[16] K B Davis, M O Mewes, M R Andrews, N J van Druten, D S Durfee, D M Kurn, and W Ketterle. Bose-Einstein Condensation in a Gas of Sodium Atoms. *Phys. Rev. Lett*, 75:3969–3973, November 1995.

[17] B DeMarco and D S Jin. Onset of Fermi Degeneracy in a Trapped Atomic Gas. *Science*, 285(5434):1703–1706, January 1999.

[18] K Dieckmann, C A Stan, S Gupta, Z Hadzibabic, C H Schunck, and W Ketterle. Decay of an Ultracold Fermionic Lithium Gas near a Feshbach Resonance. *Physical review letters*, 89(20):203201, October 2002.

[19] Dallin S. Durfee. *Dynamic Properties of Dilute Bose-Einstein Condensates*. PhD thesis, MIT, October 1999.

[20] J Esteve, JB Trebbia, T Schumm, A Aspect, CI Westbrook, and I Bouchoule. Observations of density fluctuations in an elongated bose gas: Ideal gas and quasicondensate regimes. *Physical review letters*, 96(13):130403, 2006.

[21] Richard Feynman. Simulating physics with computers. *International Journal of Theoretical Physics*, 21(6):467–488, January 1982.

[22] Robert J. Finkelstein. *Thermodynamics and Statistical Physics: A Short Introduction*. W. H. Freeman and Company, 1969.

[23] Peter E Gaskell, Jeremy J Thorn, Sequoia Alba, and Daniel A Steck. An open-source, extensible system for laboratory timing and control. *Review of Scientific Instruments*, 80(11):115103, 2009.

[24] Nathan Gemelke, Xibo Zhang, Chen-Lung Hung, and Cheng Chin. In situ observation of incompressible Mott-insulating domains in ultracold atomic gases. *Nature*, 460(7258):995–998, August 2009.

[25] F Gerbier, A Widera, O Mandel, T Gericke, and I Bloch. Spatial quantum noise interferometry in expanding ultracold atom clouds. *Nature*, 434:481–484, 2005.

[26] Tatjana Gericke, Peter Würtz, Daniel Reitz, Tim Langen, and Herwig Ott. High-resolution scanning electron microscopy of an ultracold quantum gas. *Nature Publishing Group*, 4(12):949–953, October 2008.

[27] Joseph W. Goodman. *Speckle Phenomena in Optics: Theory and Applications*. Roberts and Company Publishers, 2007.

[28] A Görlitz and W Ketterle. Enhancement and suppression of spontaneous emission and light scattering by quantum degeneracy. *Physical Review A*, 63(4):041601 EP –, January 2001.

[29] M Greiner, C Regal, and D Jin. Emergence of a molecular Bose–Einstein condensate from a Fermi gas. *Nature*, 426:537–540, 2003.

[30] M Greiner, C Regal, J Stewart, and D Jin. Probing pair-correlated fermionic atoms through correlations in atom shot noise. *Physical review letters*, 94(110401), 2005.

[31] Markus Greiner, Olaf Mandel, Tilman Esslinger, Theodor W Hänsch, and Immanuel Bloch. Quantum phase transition from a superfluid to a Mott insulator in a gas of ultracold atoms. *Nature*, 415(6867):39–44, January 2002.

[32] Subhadeep Gupta, Zoran Hadzibabic, James Anglin, and Wolfgang Ketterle. Collisions in Zero Temperature Fermi Gases. *Physical review letters*, 92(10), March 2004.

[33] Z Hadzibabic, S Gupta, C Stan, C Schunck, M Zwierlein, K Dieckmann, and W Ketterle. Fiftyfold Improvement in the Number of Quantum Degenerate Fermionic Atoms. *Physical review letters*, 91(16):160401, October 2003.

[34] Zoran Hadzibabic. *Studies of a Quantum Degenerate Fermionic Lithium Gas*. PhD thesis, MIT, 2003.

[35] David S Hall. Triggerable general-purpose interface bus controller. *Review of Scientific Instruments*, 75(2):562, 2004.

[36] Myoung-Sun Heo, Jae-yoon Choi, and Yong-il Shin. Fast production of large ^{23}Na Bose-Einstein condensates in an optically plugged magnetic quadrupole trap. *Physical Review A*, 83(1), January 2011.

[37] Tin-Lun Ho and Qi Zhou. Squeezing out the entropy of fermions in optical lattices. *Proceedings of the National Academy of Sciences*, 106(17):6916–6920, January 2009.

[38] S Inouye, M. R. Andrews, J Stenger, H J Miesner, D M Stamper-Kurn, and W Ketterle. Observation of Feshbach resonances in a Bose–Einstein condensate. *Nature*, 392(6672):151–154, March 1998.

[39] T Jeltes, J M McNamara, W Hogervorst, W Vassen, V Krachmalnicoff, M Schellekens, A Perrin, H Chang, D Boiron, A Aspect, and C I Westbrook. Comparison of the Hanbury Brown–Twiss effect for bosons and fermions. *Nature*, 445(7126):402–405, January 2007.

[40] G B Jo, Y R Lee, J H Choi, C A Christensen, T H Kim, J H Thywissen, D E Pritchard, and W Ketterle. Itinerant Ferromagnetism in a Fermi Gas of Ultracold Atoms. *Science*, 325(5947):1521–1524, September 2009.

[41] R Jördens, N Strohmaier, K Günter, and H Moritz. A Mott insulator of fermionic atoms in an optical lattice. *Nature*, 455:204–208, 2008.

[42] Aviv Keshet. The Cicero Word Generator. `https://github.com/akeshet/Cicero-Word-Generator`, 2012. [Online; accessed 13-July-2012].

[43] Aviv Keshet. USRP based PID controller. `https://github.com/akeshet/USRP-PID-Controller`, 2012. [Online; accessed 13-July-2012].

[44] Aviv Keshet and Wolfgang Ketterle. A Distributed GUI-based Computer Control System for Atomic Physics Experiments. `http://arxiv.org/abs/1208.2607`, August 2012.

[45] W. Ketterle and M. W. Zwierlein. *Proceedings of the International School of Physics Enrico Fermi, Course CLXIV*. IOS, Amsterdam, 2008.

[46] Wolfgang Ketterle and Martin W Zwierlein. Making, probing and understanding ultracold Fermi gases. http://arxiv.org/abs/0801.2500, February 2008.

[47] Arnaud Koetsier, R Duine, Immanuel Bloch, and H Stoof. Achieving the Néel state in an optical lattice. *Physical Review A*, 77(2):023623, February 2008.

[48] M J H Ku, A T Sommer, L W Cheuk, and M W Zwierlein. Revealing the Superfluid Lambda Transition in the Universal Thermodynamics of a Unitary Fermi Gas. *Science*, 335(6068):563–567, February 2012.

[49] H. J. Lewandowski, D. M. Harber, D. L. Whitaker, and E. A. Cornell. Simplified system for creating a bose-einstein condensate. `http://jila.colorado.edu/bec/CornellGroup/JLTP_Lewandowski2003.pdf`, 2003.

[50] Y J Lin, R L Compton, K Jiménez-García, J V Porto, and I B Spielman. Synthetic magnetic fields for ultracold neutral atoms. *Nature*, 462(7273):628–632, December 2009.

[51] Michael Lubasch, Valentin Murg, Ulrich Schneider, J Ignacio Cirac, and Mari-Carmen Banuls. Adiabatic Preparation of a Heisenberg Antiferromagnet Using an Optical Superlattice. *Physical review letters*, 107(16):165301 EP –, January 2011.

[52] Patrick Medley, David M Weld, Hirokazu Miyake, David E Pritchard, and Wolfgang Ketterle. Spin Gradient Demagnetization Cooling of Ultracold Atoms. *Physical review letters*, 106(19):195301 EP –, January 2011.

[53] Todd Meyrath and Florian Schreck. A Laboratory Control System for Cold Atom Experiments. `http://iqoqi.at/control`, 2006.

[54] D Miller, J Chin, C Stan, Y Liu, and W Setiawan. Critical velocity for superfluid flow across the BEC-BCS crossover. *Physical review letters*, 99(070402), 2007.

[55] Daniel E. Miller. *Studying Coherence in Ultra-Cold Atomic Gases*. PhD thesis, MIT, August 2007.

[56] E Mimoun, L Sarlo, J-J Zondy, J Dalibard, and F Gerbier. Solid-state laser system for laser cooling of sodium. *Applied Physics B*, 99(1-2):31–40, April 2010.

[57] Torben Müller, Bruno Zimmermann, Jakob Meineke, Jean-Philippe Brantut, Tilman Esslinger, and Henning Moritz. Local Observation of Antibunching in a Trapped Fermi Gas. *Physical review letters*, 105(4), July 2010.

[58] Michael A. Nielsen and Isaac L. Chuang. *Quantum Computation and Quantum Information*. Cambridge University Press, 2000.

[59] Van Oosten, U Schneider, S Fölling, B Paredes, and I Bloch. Free fermion antibunching in a degenerate atomic Fermi gas released from an optical lattice. *Nature*, 444:733–736, 2006.

[60] Scott F. Owen and David S. Hall. Fast line-based experiment timing system for labview. *Review of Scientific Instruments*, 75(1):259–265, 2004.

[61] David Pekker, Mehrtash Babadi, Rajdeep Sensarma, Nikolaj Zimmer, Lode Pollet, Martin W Zwierlein, and Eugene Demler. Competition between Pairing and Ferromagnetic Instabilities in Ultracold Fermi Gases near Feshbach Resonances. *Physical review letters*, 106(5):050402 EP –, January 2011.

[62] David Pines and Philippe Nozières. *The Theory of Quantum Liquids*, volume 1. W. A. Benjamin, Inc., 1966.

[63] Ludovic Pricoupenko and Yvan Castin. One particle in a box: The simplest model for a Fermi gas in the unitary limit. *Physical Review A*, 69(5):051601 EP –, January 2004.

[64] M. P. Quine and E. T3 Seneta. Bortkiewicz's Data and the Law of Small Numbers. *International Statistical Review / Revue Internationale de Statistique*, 55(2):173–181, January 1987.

[65] Subir Sachdev. *Quantum Phase Transisitons*. Cambridge University Press, 2nd edition, 2011.

[66] Christian Sanner. *Fluctuations in Quantum Degenerate Fermi Gases*. PhD thesis, MIT / Heidelberg University, 2012.

[67] Christian Sanner, Edward Su, Wujie Huang, Aviv Keshet, Jonathon Gillen, and Wolfgang Ketterle. Correlations and Pair Formation in a Repulsively Interacting Fermi Gas. *Physical review letters*, 108(24), June 2012.

[68] Christian Sanner, Edward Su, Aviv Keshet, Ralf Gommers, Yong-il Shin, Wujie Huang, and Wolfgang Ketterle. Suppression of Density Fluctuations in a Quantum Degenerate Fermi Gas. *Physical review letters*, 105(4), July 2010.

[69] Christian Sanner, Edward Su, Aviv Keshet, Wujie Huang, Jonathon Gillen, Ralf Gommers, and Wolfgang Ketterle. Speckle Imaging of Spin Fluctuations in a Strongly Interacting Fermi Gas. *Physical review letters*, 106(1), January 2011.

[70] M Schellekens, R. Hoppeler, A Perrin, J. Viana Gomes, D Boiron, A Aspect, and C I Westbrook. Hanbury Brown Twiss Effect for Ultracold Quantum Gases. *Science*, 310(5748):648–651, January 2005.

[71] A Schirotzek, C Wu, A Sommer, and Martin W Zwierlein. Observation of Fermi polarons in a tunable Fermi liquid of ultracold atoms. *Physical review letters*, 102(230402), 2009.

[72] U Schneider, L Hackermuller, S Will, Th Best, I Bloch, T A Costi, R W Helmes, D Rasch, and A Rosch. Metallic and Insulating Phases of Repulsively Interacting Fermions in a 3D Optical Lattice. *Science*, 322(5907):1520–1525, December 2008.

[73] C Schunck, Y Shin, A Schirotzek, and W Ketterle. Determination of the fermion pair size in a resonantly interacting superfluid. *Nature*, 454:739–744, 2008.

[74] C Schunck, Y Shin, A Schirotzek, M Zwierlein, and W Ketterle. Pairing without superfluidity: The ground state of an imbalanced Fermi mixture. *Science*, 316(867), 2007.

[75] Jacob F Sherson, Christof Weitenberg, Manuel Endres, Marc Cheneau, Immanuel Bloch, and Stefan Kuhr. Single-atom-resolved fluorescence imaging of an atomic Mott insulator. *Nature*, 467(7311):68–72, August 2010.

[76] Y Shin, C Schunck, A Schirotzek, and W Ketterle. Phase diagram of a two-component Fermi gas with resonant interactions. *Nature*, 451:689–694, 2008.

[77] C Stan and Wolfgang Ketterle. Multiple species atom source for laser-cooling experiments. *Review of Scientific Instruments*, 76(063113), 2005.

[78] S. Trotzky, P. Cheinet, S Fölling, M. Feld, U Schnorrberger, A. M. Rey, A. Polkovnikov, E. A. Demler, M. D. Lukin, and I Bloch. Time-Resolved Observation and Control of Superexchange Interactions with Ultracold Atoms in Optical Lattices. *Science*, 319(5861):295–299, January 2008.

[79] Christof Weitenberg, Manuel Endres, Jacob F Sherson, Marc Cheneau, Peter Schauß, Takeshi Fukuhara, Immanuel Bloch, and Stefan Kuhr. Single-spin addressing in an atomic Mott insulator. *Nature*, 471(7338):319–324, March 2011.

[80] David M Weld, Patrick Medley, Hirokazu Miyake, David Hucul, David E Pritchard, and Wolfgang Ketterle. Spin Gradient Thermometry for Ultracold Atoms in Optical Lattices. *Physical review letters*, 103(24):245301 EP –, January 2009.

[81] Tarik Yefsah, Rémi Desbuquois, Lauriane Chomaz, Kenneth Günter, and Jean Dalibard. Exploring the Thermodynamics of a Two-Dimensional Bose Gas. *Physical review letters*, 107(13), September 2011.

[82] M Zwierlein, C Stan, C Schunck, S Raupach, S Gupta, Z Hadzibabic, and W Ketterle. Observation of Bose-Einstein Condensation of Molecules. *Physical review letters*, 91(25):250401, December 2003.